INFORMATION TO USERS

This manuscript has been reproduced from the microfilm master. UMI films the text directly from the original or copy submitted. Thus, some thesis and dissertation copies are in typewriter face, while others may be from any type of computer printer.

The quality of this reproduction is dependent upon the quality of the copy submitted. Broken or indistinct print, colored or poor quality illustrations and photographs, print bleedthrough, substandard margins, and improper alignment can adversely affect reproduction.

In the unlikely event that the author did not send UMI a complete manuscript and there are missing pages, these will be noted. Also, if unauthorized copyright material had to be removed, a note will indicate the deletion.

Oversize materials (e.g., maps, drawings, charts) are reproduced by sectioning the original, beginning at the upper left-hand corner and continuing from left to right in equal sections with small overlaps. Each original is also photographed in one exposure and is included in reduced form at the back of the book.

Photographs included in the original manuscript have been reproduced xerographically in this copy. Higher quality 6" x 9" black and white photographic prints are available for any photographs or illustrations appearing in this copy for an additional charge. Contact UMI directly to order.

UMI

A Bell & Howell Information Company
300 North Zeeb Road, Ann Arbor MI 48106-1346 USA
313/761-4700 800/521-0600

An Investigation of the Influence of a Transverse Magnetic Field on the Formation of Large Anode Fall Voltages in Low-Pressure Arcs

by

John Edison Foster

A dissertation submitted in partial fulfillment
of the requirements for the degree of
Doctor of Philosophy
(Applied Physics)
in The University of Michigan
1996

Doctoral Committee:

Assistant Professor Alec Gallimore, Chair
Professor Michael Bretz
Professor Ronald Gilgenbach
Professor Y.Y. Lau
Professor Fred Macintosh

UMI Number: 9711967

UMI
300 North Zeeb Road
Ann Arbor, MI 48103

To my Mother

ACKNOWLEDGMENTS

I would like to extend my warmest thanks to my advisor, Dr. Alec Gallimore, for his excellent support, guidance, and meaningful discussions that generously flowed throughout my graduate years. I would also like to thank Dr. Gilgenbach not only for his support but also for introducing me to an array of plasma diagnostics in his plasma diagnostics course. I would like to give thanks to Dr. Lau for his support and his insight imparted to me through discussions and his course on plasma physics. I am grateful to Dr. Bretz and Dr. Macintosh for reviewing my thesis. Indeed, I would like to thank all the members of my thesis committee. Each have played an important role cultivating in me important skills that have made me a scientist.

I am also indebted to Dr. Clarke, Director of Applied Physics, who served as an invaluable source of support and advice, particularly in my early graduate years. I would also like to thank Dr. Homer Neal, not only for playing a major part in convincing me to come to the University of Michigan, but also for his support.

I would like to thank the National Physical Sciences Consortium for fellowship support. I would like to thank NASA Lewis Research Center for sponsoring my fellowship. I would also like to give thanks to NASA engineers Mike Patterson, Roger Myers, Dave Byers, and Frank Curran for advice and equipment support.

I am also grateful for the members of my research group: Matt, Sang, Colleen, James, Brad, Frank, and George. For all the physical problems that we tackled over the years, we are all the more wiser. I would also like to thank Gary, Tom, and Terry for technical advice and fabrication of various experimental components. I also thank the graduate secretaries Rohn, Marge, Bonnie, and Caroline.

I also thank my mother and sisters who have been an immense source of motivation and inspiration throughout my graduate years and indeed my life. I thank my friend Valarie who has not only been a source of inspiration and support but also a source of very meaningful scientific discussions concerning my work. I would also like to acknowledge Jhules, a member of my entering class who has been a good friend throughout my graduate years.

Finally, to put all of this into proper perspective, I give thanks to God for without Him none of this would have been possible.

PREFACE

This research focuses on understanding the physical mechanisms underlying the formation of large anode sheath potentials [sheath potentials that are significant fractions (>0.5) of the total discharge voltage] in low pressure arc discharges that are immersed in a transverse magnetic field. An understanding of these processes can provide much insight into methods for reducing such sheath potentials. NASA and the private sector in general are interested in understanding these processes because the potential distribution at the electrodes of plasma accelerators used for space propulsion (i.e. orbit maintenance of communication satellites) determine erosion phenomena, which determines engine lifetime, and power losses at the electrodes, which determine engine overall efficiency. The low pressure discharge under transverse magnetic field conditions is a configuration utilized in a number of electric propulsion devices that rely on Lorentz forces for thrust production. In such systems the anode fall voltage term dominates anode power deposition. For example in magnetoplasmadynamic (MPD) thrusters, the power deposited into the anode driven by large anode fall voltages can be in excess of 50% of the total input discharge power. In order to study the anode fall problem, a D.C. plasma diode is used to generate a low pressure discharge. An electromagnet provides a uniform transverse field in the near-anode region. In addition, a coil coaxial with the anode is used in this study to impose varying axial magnetic fields at the anode surface and in the near-anode region. Langmuir probes and emission spectroscopy are used to measure plasma properties in the near-anode region as a function of the magnetic field. Water calorimetry is used to measure actual power flux deposited into the anode.

A number of significant results were obtained from this study. During the near-anode characterization phase of this study, it was found that the anode fall voltage is a strong function of the relative available transverse current and local electron number density.

This finding is significant in that it exposes the major variables that determine the anode fall voltage. Guided by the findings of the characterization study, an auxiliary discharge was used to modify plasma properties in the near-anode region at a fixed transverse magnetic field strength. It was found that the increases in the electron number density associated with the operation of the auxiliary discharge gave rise to significant reductions in anode power deposition and in the anode fall voltage. This finding is also significant in that it suggests a means of reducing the anode fall voltage under transverse magnetic field conditions. In another part of this research, an axial magnetic field was found to have little effect on the measured anode fall voltage at a fixed transverse magnetic field. The independence of the anode fall voltage on the axial magnetic field is significant in that it suggests that re-interpretation of findings of previous studies concerning the effect of magnetic field angle on anode fall voltage may be necessary. Finally, a numerical model was developed to predict the variations in anode fall voltage with transverse magnetic field strength. The model's predictions were in good agreement with measured anode fall voltage variations in response to the changing transverse magnetic field. This finding is significant in that it demonstrates that the postulated physical processes of the model represent important physical aspects of the problem, particularly in the limit of large transverse magnetic field. In this respect, the model can be used as a guide in predicting anode fall behavior as a function of the transverse magnetic field in plasma thrusters. Even though the potential for application of this research is largest in the electric propulsion community, the research findings may have some applicability in the plasma processing community (i.e. coaxial plasma sprayers) and in the lighting industry (minimizing electrode losses in plasma light sources).

TABLE OF CONTENTS

CHAPTERS

LIST OF FIGURES

Figures

LIST OF APPENDICES

Appendix

CHAPTER 1

INTRODUCTION

1.1 Motivation

Exploration of the solar system and beyond requires the development of new and improved rocket propulsion systems. Whether a given rocket system can be realistically used for such energetic missions largely depends on the whether the rocket engine can impart the necessary change in velocity, Δv, to the payload as quickly and economically as possible. Present chemical rockets fall far short in achieving these goals. In general, the fuel needed for a given mission rises exponentially with Δv. This assertion is based on the rocket equation:

$$\frac{M_i}{M_f} = \exp(\frac{\Delta v}{u_e}). \tag{1.1}$$

Here $\frac{M_i}{M_f}$ is the ratio of the initial mass of the rocket including fuel to the final mass of the rocket at the end of the fuel burn and u_e is the effective exhaust velocity of the rocket. According to the rocket equation, the fuel requirements for a given mission grows exponentially with Δv. Because a chemical rocket's exhaust velocity is limited to the chemical energy released in the combustion chamber, u_e for all practical purposes is fixed; therefore, such systems cannot offset the exponential rise in fuel requirements for highly energetic missions. In general, chemical rockets are not well suited for those missions where the mission Δv is much larger than 5000 m/s, which roughly corresponds to the maximum exhaust velocity attainable with conventional systems.

Electric propulsion systems on the other hand offer unique advantages over traditional chemical rockets. Electric propulsion itself is a facet of rocket science that deals with those engine systems which generate thrust by electrical means. These systems can minimize the mass ratio requirement, $\frac{M_i}{M_f}$, by increasing the exhaust velocity. In general. the input electrical energy goes into increasing the kinetic energy of the fuel, thus providing a wide range of exhaust velocities for which these systems can operate. These devices are typically low thrust and usually require longer thrusting times to achieve the required Δv than their higher thrust. low exhaust velocity chemical rocket counterparts.

The basic electric propulsion thrust production schemes are illustrated in Figure 1.1. In general. the various electric propulsion devices can be categorized into three groups. The first category is electrothermal acceleration. This category, which in general is the simplest. includes engines which generate thrust via the application of thermal energy to the propellant by way of an electrical heating element. The electrothermal system illustrated in Figure 1.1 is that of an arcjet which utilizes an electric arc struck between two electrodes to heat gas flowing through it. The expansion of this hot gas through the nozzle generates the thrust. The second category of electric propulsion is electrostatic acceleration. Here large electric fields are used to accelerate the charged particles of a plasma to generate thrust. The electrostatic system illustrated in Figure 1.1 is an ion engine. The ion engine utilizes a set of closely spaced grids to extract ions from the discharge plasma and accelerate them rearward to generate thrust. An additional device called a neutralizer is used to inject electrons into the ion beam to neutralize it and to prevent the engine and spacecraft from charging negatively. The final category of electric propulsion is that of electromagnetic acceleration. Here, it is the interaction between the electric and magnetic fields and the plasma that generates thrust. Typically, such systems utilize orthogonal electric and magnetic field geometries so that Lorentz forces acting on the plasma accelerates it out of the device. The electromagnetic system illustrated in Figure 1.1 is that of a magnetoplasmadynamic (MPD) thruster. In this device, a large kiloamp discharge arc generates a strong self-magnetic field. It is the interaction between this self-magnetic field and the plasma current that "blows" the plasma out of the device thereby generating thrust.

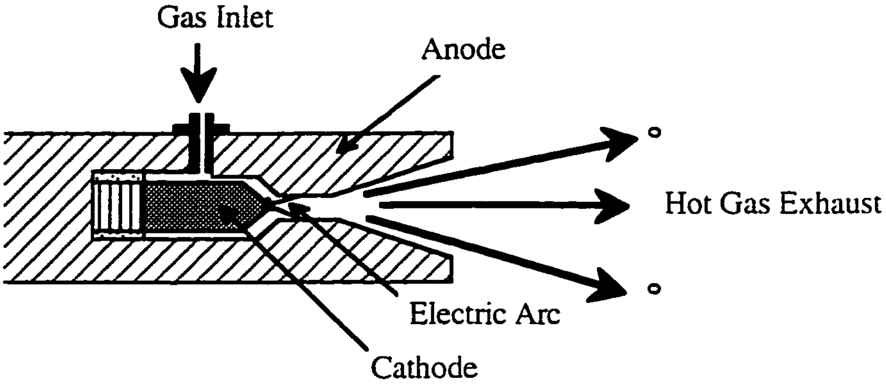

Arc Jet (Electrothermal)

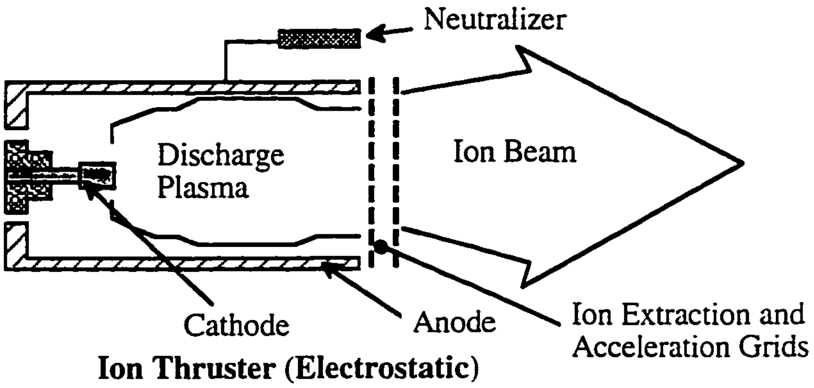

Ion Thruster (Electrostatic)

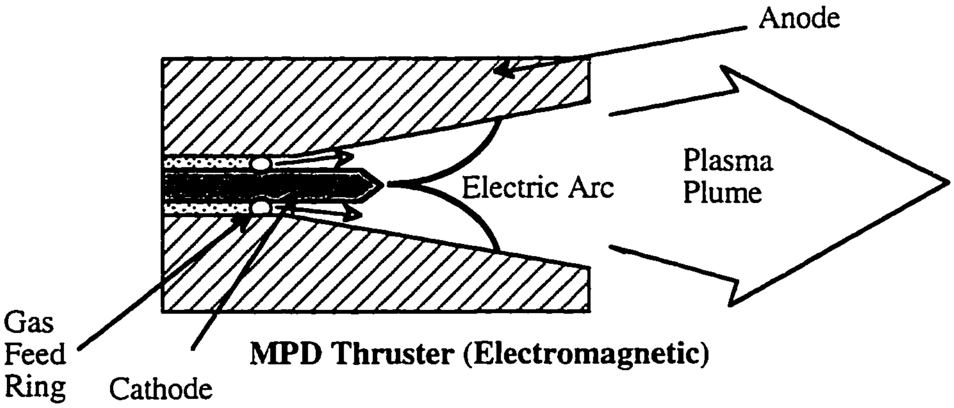

MPD Thruster (Electromagnetic)

Fig. 1.1. Electric Propulsion Devices.

In general, for electric propulsion systems, power supply mass scales linearly with output power level. In addition, at a fixed thrust, the exhaust velocity scales linearly with thruster input power level.[1] As mission requirements become more energetic, the required power level and the associated power supply mass increases proportionally. Ideally, one would like to minimize power supply mass so that for a fixed rocket mass, more payload can be carried on a particular mission. In order to maximize payload mass for a given rocket mass and exhaust velocity, one requires that the engine operate as efficiently as possible. Understanding and characterizing the efficiency of an electric rocket is an important aspect of engine development. A great deal of insight in terms of understanding the efficiency and life-time of an electric propulsion system can be obtained by understanding the processes that occur at the electrodes of these devices. The relatively large importance that the electrodes play in determining operating characteristics of D.C. plasma devices cannot be overemphasized for it is at the electrodes where significant potential gradients can exist. Such potential differences at the electrodes play an important role in determining the nature of the energy exchange between the plasma and the physical electrodes.

Indeed, the importance of understanding near-electrode processes is dramatically illustrated by energy loss phenomena occurring at the anode of MPD thrusters. Here energy losses to the anode of these devices can account for over 70% of the input discharge power.[2] Of all the electric propulsion systems, only the MPD offers both high exhaust velocities and high thrust.[1] Typically, these devices are operated at power levels in the 100 kW to 1 MW range. With electrical inefficiencies of greater than 70 percent, providing high power to the device to achieve reasonable performance while managing the waste heat becomes a daunting task. Because of such misgivings these systems are not presently being considered for space applications.

The energy inefficiency problem associated with anode power deposition in MPD thrusters has been shown to be related to the large anode fall voltages that form under the influence of the transverse magnetic field present during engine operation.[3] Because a number of electric propulsion systems including MPD engines utilize crossed-field configurations to generate thrust, the need to understand specific plasma-electrode interactions under transverse magnetic field conditions naturally arises. Again such an understanding would not only provide insight into the nature of inefficiencies associated with near-electrode phenomena under the influence of a transverse magnetic field, but also insight into the nature of engine life-time because large potentials at the electrode can drive erosion processes there. The primary goal of this research then is to understand why energy losses at the anode are so large and to determine how these losses can be significantly reduced based on an understanding of how the near-anode plasma behaves in response to changes in an applied transverse magnetic field. These objectives are undertaken by thoroughly investigating the effect that a transverse magnetic field has on anode sheath potentials using a low-pressure arc configuration designed to simulate near-anode conditions found in 100-kW-class MPD thrusters.[2] The relevance of this study to MPD thruster research is related to the fact that both the self-field and the applied axial magnetic field present in MPD thrusters are perpendicular to current flow as is simulated in this investigation. This information is not only of practical value to the electric propulsion community, but also of fundamental importance to understanding the nature of the anode fall region under the influence of a transverse magnetic field.

The general approach to this research is comprised of a number of stages. It is postulated that the changes in local plasma properties near the anode brought on by changes in the magnetic field ultimately affect the anode fall voltage and the associated anode power deposition. Accordingly, the first stage of this research entails characterizing near-anode plasma properties via Langmuir probes, emission spectroscopy, and water calorimetry. The purpose of this stage is to experimentally determine the behavior of the anode fall voltage in response to variations in measured near-anode plasma properties brought on by changes in the transverse magnetic field. In addition, the effect of an axial magnetic field on the anode fall voltage is investigated. With the empirical findings from the characterization study as a guide. the second phase of this research involves externally varying near-anode plasma conditions at a fixed transverse magnetic field to determine if the expected anode fall voltage behavior occurs. Finally, the last stage of this research comprises using scaling relations determined from the previous two stages to develop a model that analytically describes the effect that a transverse magnetic field has on anode sheath voltages and ultimately on anode power deposition. This facet of this investigation also includes comparing the model to experimentally determined results.

1.2. A Physical Description of Phenomena Associated with Arc Discharges

The discharge type utilized in this study is that of a low-pressure electric arc. The electric arc itself is a self-sustaining high current, low impedance plasma discharge. In comparison to glow discharges, the electric arc owing to a relatively high cathode emission current, does not rely heavily upon electron amplification to sustain the discharge.[4] Typically unmagnetized arcs are associated with low discharge voltages (less than 100 V) and correspondingly low potential drops near the electrodes. These potentials at the electrodes are shielded from the rest of the plasma via space charge layers called sheaths. Indeed the only appreciable steady-state electric fields that can exist in a discharge are those that are confined near the electrodes due to the effect known as Debye shielding. In the case of unmagnetized arcs, electrode sheath voltages rarely exceed the ionization potentials of the working gas; as a result, energy loss and erosion phenomena at the electrodes are minimal. The low impedance nature of this type of discharge makes it an attractive plasma sources for electric propulsion applications. Indeed, the electric arc is a common discharge utilized in many electric propulsion systems ranging from arcjets and ion thrusters to MPD engines.

In order to isolate the relevant physics occurring in the near-anode region of an arc discharge under the influence of a transverse magnetic field, a simple D.C. plasma diode configuration consisting of a cathode and coaxial but planar anode is employed (see Figure 1.2). The arrows in Figure 1.2 denote the direction of electron flow. A set-up of this type was chosen not only because of its simplicity but also because it allows for the analysis of the problem in a more fundamental manner, yielding results of a more general nature than would be otherwise obtained if an actual electric propulsion device were used.

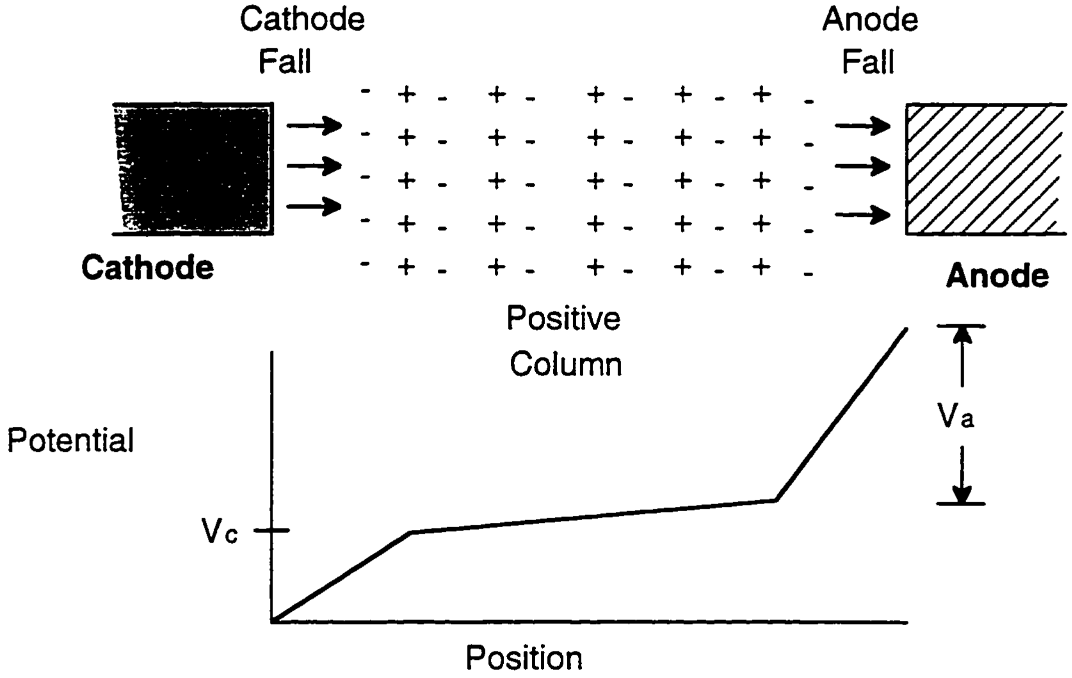

Fig. 1.2. Diagram of an Electric Arc.

1.2.1. The Anatomy of an Electric Arc

The arc discharge can be divided into three regions (see Figure 1.2): 1.) the cathode fall region, 2.) the positive column, and 3.) the anode fall region. Each region performs a task necessary for the maintenance of the arc. The cathode fall region, which is associated with a potential rise between the cathode and the adjacent positive column, has a number of functions. The cathode fall region is a major energy source for the entire discharge. This potential rise injects cathode electrons into the positive column. There the electrons collide with gas atoms thus generating electron and ion pairs as well as exciting heavy particles electronically. The energy gained by electrons accelerated across the cathode fall is not sufficient to sustain arc currents (>1 Amp) through electron amplification; therefore, the electron/ion pairs formed via electron bombardment of neutrals contribute to only a small percentage of the total discharge current. Because the arc's typically low cathode fall voltage is insufficient to achieve large currents via multiplication, large cathode emission rates are necessary. With the cathode electron emission rate accounting for over 70% of the total electron discharge current, it is the cathode that is the major supplier of discharge electrons. Such copious emission is made possible primarily through thermionic emission at the cathode surface. Although thermionic emission is a major source of these discharge electrons, the electric field associated with the cathode fall region does enhance electron emission via field and field-thermionic emission. Another key function of the cathode fall region is to attract and accelerate ions that drift into this region from the positive column. This ion current to the cathode, usually accounting for less than 30% of the total discharge current, deposits energy gained from acceleration across the cathode fall into the cathode body, thus allowing the cathode to maintain its thermionic emission temperature which typically exceeds 2000 C.[4]

The positive column, located between the cathode fall and the anode fall regions, functions as a conductive path that electrically connects the two fall regions together. The electric field associated with this region is typically small owing to the shielding of potentials occurring at the anode and cathode by space charge layers. The non-zero electric field that does exist in this region establishes electron drift toward the anode and ion drift toward the cathode. Electron flow into this region from the cathode and the ionization processes driven by these electrons maintain the conductivity of this region thus offsetting diffusional and recombinational losses.

Because the electric field within the positive column is non-zero, the electrons in this region can acquire energy from this field. A fraction of this acquired energy is lost via inelastic collisions with heavy particles. The power per unit volume dissipated in the positive column by the drifting electrons is $\bar{J} \cdot \bar{E}$. This quantity can be related to the average energy that an electron gives up per collision, ΔU:

$$\bar{J} \cdot \bar{E} = n_e \nu_c \Delta U \tag{1.2}$$

Here ν_c is the electron-heavy particle collision frequency, J is the current density, and E is the electric field. In thermal electric arcs, the energy exchange between the electrons and heavy particles is sufficient to produce an equilibrium system where $T_e = T_i = T_g$. Here T_e is the electron temperature, T_i is the ion temperature, and T_g is the gas temperature. Such conditions prevail in high pressure arcs where the operating pressures range between 0.5 and 1.0 ATM.[4,5] As for this research and for many electric propulsion systems, because $T_e \neq T_i$ prevails, the plasma is in a non-equilibrium state.

The final region of the electric arc, which is the portion that is the subject of this research, is that of the anode fall. This region is associated with a potential change that either increases or decreases as the anode is approached from the positive column depending on the operating conditions of the discharge. The primary function of the anode fall in an electric arc discharge is to collect the current-carrying electrons. Under conditions where the random thermal flux greatly exceeds the discharge current requirements under constant current operation, the anode fall is slightly negative (electron repelling). Such a potential gradient reflects just enough electrons so that the collected current is equal to the discharge current. Under conditions where the thermal current is on the order of the discharge current or slightly below, the anode fall region is positive (electron attracting). Under certain positive anode fall conditions, ionization can occur in the anode fall region thus providing the additional electrons needed to sustain the discharge.[6]

1.2.2. Electrostatic Sheaths and Their Role in Energy Transport Phenomena

As mentioned earlier, unshielded potentials of appreciable magnitude, $V > \frac{kT_e}{2e}$, cannot be supported in the bulk discharge plasma. However, potentials of such magnitude can be found near the electrodes. There these potentials are insulated from the rest of the plasma via a space charge layer called a sheath. The anode and cathode fall regions of the electric arc are actually space charge sheaths. Sheaths form when oppositely charged plasma particles form "clouds" or layers around a body immersed in the plasma. The spatial extent over which the sheath potential is appreciable is called the Debye length:

$$\lambda_D = \sqrt{\frac{kT_e \varepsilon_o}{n_e e^2}} \, . \tag{1.3}$$

Here, n_e is the electron number density, k is Boltzmann's constant, e is the elementary charge of an electron, and ε_o is the premittivity of free space. This length scale, λ_D, is the $1/e$ spatial decay constant for the potential generated by a test charge placed into the plasma. The potential distribution associated with an electrode or test charge is calculated by solving Poisson's equation:

$$\nabla^2 \Phi = \frac{e \cdot (n_e - n_i)}{\varepsilon_o} . \tag{1.4}$$

A Boltzmann distribution is used to describe the electron density :

$$n_e = n_o \cdot \exp\left(\frac{e\Phi}{kT_e}\right) . \tag{1.5}$$

Here, Φ is the potential of the plasma and n_o is the background electron number density. As stated earlier, shielding arises due to the formation of an encapsulating space charge sheath of charge opposite to that of the electrode. A surface integral of electric field over the surface of the sheath surrounding the electrode is essentially zero: $\oint_S \vec{E} \cdot d\vec{A} = 0$, which implies that the electric field at the sheath boundary is also zero. Again, the vanishing surface integral is due to the fact that the total net charge in the volume surrounding the sheath is zero.

In general, any unbiased (floating) body in contact with the plasma develops a sheath. The sheath of such bodies function to regulate the flow of charged particles to that body so that the net current to floating body is zero. The potential difference between a floating body and the adjacent quasi-neutral plasma develops as a result of the disparity in mobilities between electrons and ions. This disparity is a consequence of the small ratio of ion temperature to electron temperature ($\frac{T_i}{T_e} << 1$) prevailing in low pressure discharges and the large ion to electron mass ratio. Under these conditions, a body initially thrust into the plasma will charge up negatively due to the flow of the much more mobile electrons. This initial layer generates a potential that impedes the flow of electrons to the body while at the same time collecting the ions. As such, the potential distribution across the sheath adjusts itself so that in its equilibrium configuration, the flux of electrons impinging upon the body is equal to the flux of ions flowing to the body. The condition for a sheath to form at a floating body is known as the Bohm Sheath Criterion and it requires that ions of mass M enter the sheath at least at the ion acoustic velocity: $c_s = \sqrt{\frac{kT_e}{M}}$ for conditions where $\frac{T_i}{T_e} << 1$.[7] Ion velocities in the bulk plasma in general are not sufficient to satisfy this criterion. In order to satisfy the condition for sheath formation, ions must be accelerated to the ion acoustic velocity. The required acceleration region is called the presheath. This region, which extends beyond the sheath edge, contains the necessary electric field and acceleration length to speed the ions up to the ion acoustic velocity.[8]

The physics of a biased, current collecting electrode immersed in a plasma is similar to that of the unbiased electrode in a plasma. In this case, however, the electron flux to an electron collecting electrode must be regulated in order to maintain a constant net current. The potential difference between the electrode and the nearby plasma may be either positive or negative depending on local plasma conditions. As mentioned earlier, negative, electron repelling sheath potential can be expected to develop if the thermal flux of electrons impinging upon the electrode exceeds the current actually being extracted from the discharge. This potential "hill" serves the purpose of reducing the flux of electrons to the electrode in essence filtering the low energy electrons from entering the sheath while allowing only those electrons with energy sufficient too "climb" the potential hill and reach the electrode. The potential profile is expected to be positive, electron attracting, in the reverse situation where the thermal current is on the order of or possibly less than the current being collected at the electrode. Such a potential distribution can repel ions, impart energy to electrons so that additional electrons are created by ionization in the sheath if the layer is collisional, or increase input electron flux into the sheath by leaking additional electric field into the presheath region, thus increasing the mobility term's $(-\mu \cdot \vec{E})$ contribution to the total electron current.[6] Here, μ is the electron mobility, the proportionality constant between electron current density and the electric field.

Significant amounts of input power can be deposited into the electrodes if the charged particles entering the sheath are accelerated by the potential distribution present there. This power flux that is deposited into the electrodes can be as high as $\Delta V \cdot \mathrm{I}$, where I is the discharge current and ΔV is the potential difference across the sheath. In the case of the cathode, this power flux supplies the energy required for the cathode to emit thermionically. In the case of the anode, this transported energy ends up as waste heat which in general contributes to the overall inefficiency of the discharge device.

1.2.3. The Anode Sheath and its Role in Determining Power Losses at the Anode

As stated earlier, both the anode and cathode fall regions are sheaths. These regions along with the positive column play important roles in determining the nature of energy transport between the power supply, the plasma, and the electrodes. The cathode fall region is the major source of electron energy in the discharge. Inside the positive column, a fraction of this energy is deposited into collision events with the heavy particles. The nature of energy transport in the anode fall region has yet to be discussed. Understanding energy transport phenomena associated with the anode fall voltage, particularly under the influence of an applied transverse magnetic field, is a goal of this research that has significant relevance to electric propulsion devices such as MPD thrusters.

Energy flows from the power supply to the partially ionized gas by way of electric field driven collisions between 1.) electrons and the heavy particles and 2.) primary electrons and secondary electrons. In an ideal situation, these processes primarily account for the energy deposited into the ionized gas. At equilibrium, the input energy equals the energy required to sustain ionization processes plus the energy lost to the surrounding environment. Loss processes include diffusion of electrons, photons, and hot gas to the surrounding (and in many cases cooler) walls of the plasma vessel. With the exception of the fact that the anode is a biased current collection element, the anode too acts essentially as a wall element where plasma cooling processes can take place. Under ideal conditions where the anode sheath potential is small compared to the random thermal energy of the electrons, energy lost from the plasma to the anode consists of essentially electron and gas conduction/convection contributions along with collected radiation emitted from the plasma and the hot cathode. A more complete description of the energy flux flowing into the anode was formulated by Cobine.[9] According to Cobine's treatment, power lost to the anode, P_A, consists primarily of three terms:

$$P_A = (\frac{5kT_e}{2e} + \Phi_{wf} + V_a) \cdot I_d + P_c + P_r. \tag{1.6}$$

The first term, which (set off in parenthesis) is proportional to the discharge current (I_d), primarily expresses the electronic contribution to anode heat flux. The $\frac{5kT_e}{2e}$ component of this term represents the contribution to anode power deposition due to the random thermal energy of the electrons plus the energy contribution associated with the general electron drift toward the anode. The second component of the electronic term is the work function term, Φ_{wf}. This term represents the energy released into the metal when the electron enters the conduction band of the metal electrode. The V_a term is associated with the potential difference across the anode sheath. For positive, electron attracting sheath potentials, each discharge electron that enters the sheath can acquire from the sheath electric field an energy of up to eV_a. This energy contribution is then deposited into the anode upon the electron's collision with the metal surface. For negative, electron repelling potentials at the anode, ion flux to the anode must also be considered. Under these conditions, the energy that is deposited into the electrode due to the electrons is reduced due to the fact that electrons must transverse a retarding potential to reach the anode. The remaining terms P_c, which represents gas heating or cooling of the electrode via conduction or convection, and P_r, which represents power flux incident on the anode due to cathode and plasma radiation, account for the remainder of energy flux into the anode.[9]

Cobine's energy balance relation is used to estimate anode power losses in MPD thrusters and has shown good agreement with water calorimetry measurements of anode power deposition.[10] In MPD thrusters, it is the V_a component of the electronic term that dominates the anode power deposition. In this respect, the nature of the anode fall region essentially dictates the efficiency of the device. Driven by large anode sheath potentials, the magnitude of the anode power deposition in MPD thrusters runs in excess of 70% of the input electrical power.[2] In contrast to MPD devices, ordinary, unmagnetized electric arcs operate under conditions where the anode fall voltage is small or even negative ($V_a < 3$ V).[4] It is the presence of the transverse magnetic field that apparently enhances the anode fall voltage. Again, understanding the mechanisms behind the anode fall growth with the transverse magnetic field is a goal of this research.

1.3. Review of Past Research

Although the research results presented in this work are of direct relevance to many electric propulsion devices, the motivation behind this research is linked to the need to understand and ultimately solve the anode power deposition problem in MPD thrusters. As stated earlier over 70% of the input electrical power goes into waste heat deposited into the anode.

1.3.1. The MPD Thruster

Before elaborating on past research, it is worthwhile to discuss the basic operation of the MPD thruster. MPD thruster operation can be understood by looking at the discharge plasma from a continuum fluid dynamics point of view. The schematic in Figure 1.1 describes the basic MPD engine configuration. An arc on the order of kiloamps is struck between the cathode and anode thus generating a discharge plasma. Typical working fluids include liquid metals, rare gases, or hydrogen. The high currents generate self-magnetic fields which run parallel with the anode surface in the azimuthal direction. As a consequence, electrons must undergo a collision dominated random walk across the field lines to reach the anode. The plasma current interacts with the self-magnetic field via the $\bar{J} \times \bar{B}$ Lorentz force. This force acts on the plasma "fluid elements" and accelerates them out of the discharge chamber to generate thrust. In some MPD thruster configurations, axial magnetic fields are used to help stabilize the discharge. Researchers have found that this axial magnetic field also tends to enhance thrust production.[11] It has also been found that increases in the magnitude of these transverse magnetic fields give rise to increases in anode power deposition.[3] Typically, the anode of these research engines when operated at steady-state are water-cooled so as to prevent the anode from melting due to the large heat flux deposited into it during operation.[10] Understanding and ultimately determining ways of reducing this heat flux to the anode of MPD devices has long been sought after.

1.3.2. Past Research

The search for the underlying mechanisms for large power losses at the anode has gone on for many years. In general, most studies indicate that power deposited into the anode is dominated by the anode fall voltage in the electronic term of the anode power deposition equation. Various parameters such as applied magnetic field strength and local electron number density all influence the potential profile of the anode fall region. This region as was noted earlier is the prime driver that imparts to the electrons the energy which is ultimately deposited into the anode. Below, past research associated with the investigation of the nature of the anode power deposition problem will be reviewed. Major research on this problem has taken place at Princeton University, the University of Minnesota, the Stuttgart University in Germany, the NASA Lewis Research Center, the Los Alamos National Laboratory, and the Massachusetts Institute of Technology.

The mechanical and aerospace engineering department at Princeton University for many years has studied the problems associated with MPD thrusters. Work of interest at Princeton and of direct relevance to this study is that presented in the doctoral thesis of Gallimore.[12] In this study, thermocouples, magnetic, and electrostatic probes were used to investigate the plasma in the near-anode region of pulsed and steady-state MPD thrusters. Anode fall voltages were inferred from the energy balance relation. Anode fall voltage scaling trends were also investigated. In this particular study, changes in the anode fall voltage was shown to correlate with changes in the Hall parameter. The Hall parameter, $\frac{\Omega_e}{\nu_e}$, is the ratio of the electron cyclotron frequency to the electron collision frequency. Small Hall parameters imply electron motion in which magnetic effects can largely be ignored. Large Hall parameters indicate that plasma motion is magnetized with the electrons undergoing many gyrations about a field line before undergoing a collision with at heavy particles. This finding supports previous investigations which indicate that the anode fall voltage is a function of the transverse magnetic field. Apparently the anode fall increases in order to maintain constant current. The study also found that anode power deposition scaled with the anode fall and the Hall parameter. Finally, the study utilized a ring of permanent magnets, which was retrofitted to the MPD thruster anode, to annul the local azimuthal magnetic field in the near-anode region (see Figure 1.3). This approach was taken to locally reduce the Hall parameter. This technique was shown to reduce the anode fall voltage by as much as 45%. This finding pointed to the fact that magnetic field direction and magnitude near the anode may be an important parameter that can be externally adjusted to reduce the anode fall.[12]

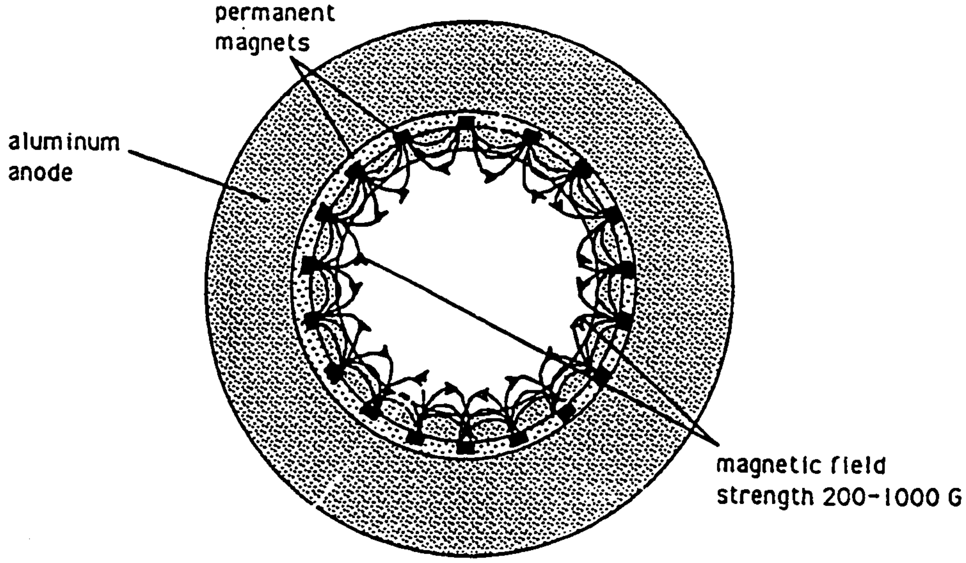

Figure 1.3. Magnetically Annulled Hall Parameter Ring.[12]

Over the years, Pfender of the University of Minnesota has carried out extensive research on anode power deposition in MPD thrusters. One of his studies utilized a segmented anode (see Figure 1.4a.) that was used to test the validity of Cobine's anode power balance equation (Equation 1.6). Each anode segment was electrically isolated from adjacent segments via insulator spacers. The water-cooled segmented anode afforded the opportunity to "float" given segments (no current extraction) to obtain calorimetic estimates of the fraction of power deposited into the anode due to the radiation, conduction, and convection terms of the energy balance relation. The study found that 70-80% of the anode heat flux could be attributed to the electronic term in the energy relation. The anode fall voltage was found to increase with increasing axial magnetic field, but the overall slope of the total arc voltage was much greater, indicating that more power was going into the plasma with increasing axial magnetic field strength. For operating pressures above 1 Torr, the study found that the discharge voltage increased with increasing mass flow rate while the anode fall voltage was measured to decrease. Calorimetric measurements taken from the water-cooled anode segments confirmed the applicability of the energy balance model for the segmented anode. This confirmation was made by measuring the heat flux to the anode segments as current to the segments were varied in such a way that the total current summed over all segments was constant (That is to say the current distribution at the anode was varied while the total discharge current was held constant.). At constant current, the investigators argued that the contribution of anode heat flux via the radiation and the conduction/convection term should be constant depending on total current only and not current distribution. It was also assumed that the term set off in the parenthesis of the electronic contribution of the power flux equation was independent of discharge current. This assumption was justified by experimental evidence which showed that local electron temperature and anode fall voltage did not vary with discharge current. If these assumptions hold, the energy balance relation for a given segment should be a simple linear function of current with the sum of the radiation and conduction/convection terms appearing as the y intercept. Plots of heat flux versus segment current (see Figure 1.4b.) yielded straight lines which is in agreement with the predictions elaborated on above.[10]

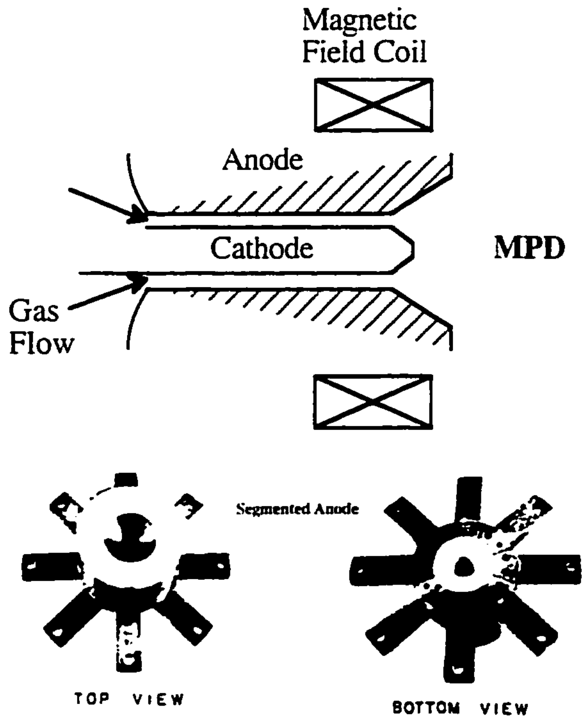

Figure 1.4 a. Segmented Anode MPD Thruster used in the Shih and Pfender Study.[10]

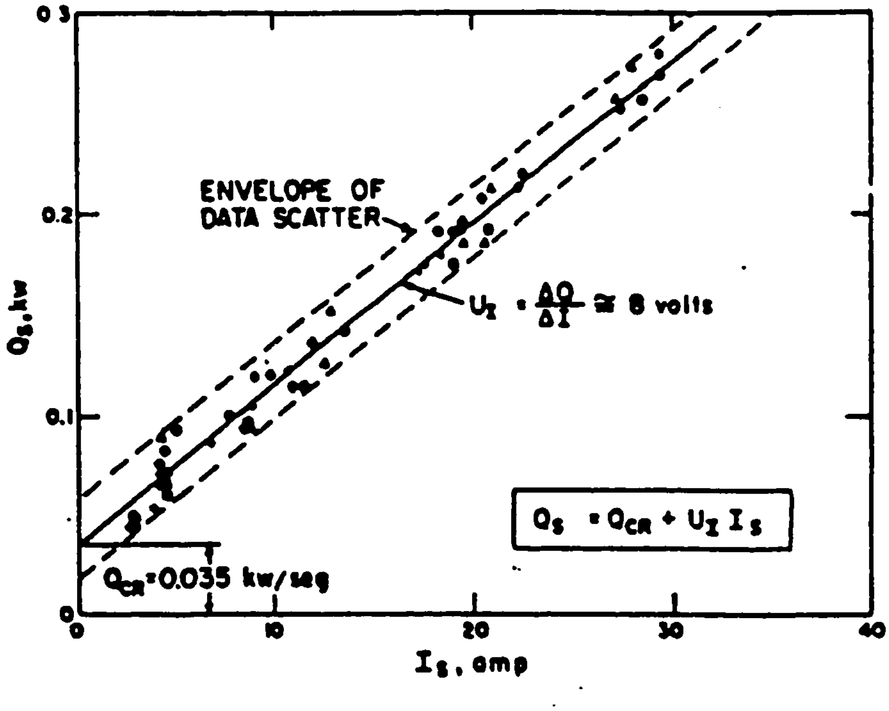

Figure 1.4b. Anode Segment Power Flux Versus Segment Discharge Current.[10]

Another important anode power deposition study was conducted by Wolfgang Schall of DFVLR-Institute of Plasma Dynamics at Stuttgart, Germany.[3] This study was concerned with understanding the effects of magnetic field orientation and magnitude on energy losses to the anode in MPD thrusters. The author used two independent electromagnet coils in the experimental set-up (see Figure 1.5). With this arrangement, the angle between the magnetic field and the anode surface could be varied. The authors pointed out that in the past, under the assumption that the anode fall region was responsible for ion acceleration and thus most of the thrust, researchers attempted to increase the magnitude of the anode fall region's electric field. This fall region, they argued, could be enhanced via magnetic fields and reduced mass flow rates. Upon attempting both approaches, these researchers found that instead of obtaining the desired result (increased thrust power), most of the input electrical power ended up instead as waste heat deposited into the anode. In this study, anode power deposition was measured as a function of magnetic field and anode pressure.[3]

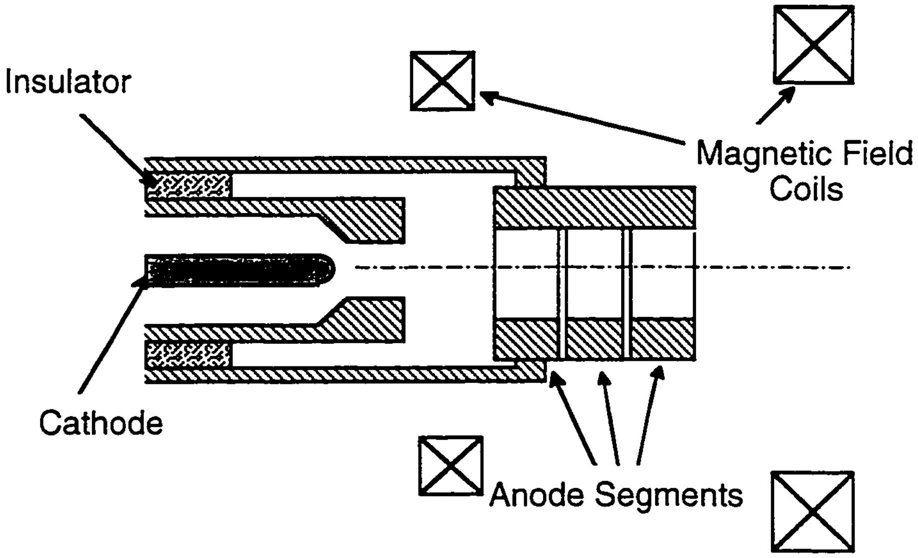

Figure 1.5. Stuttgart Laboratory MPD Thruster.[3]

The Stuttgart study found that in the pressure range above 0.1 Torr, anode heat losses were small and slowly varying functions of magnetic field. At pressures below 0.1 Torr and at magnetic fields above a critical intensity, further increases in the magnetic field was shown to have a large effect on the anode fall. These findings suggest that the anode fall voltage also depends on discharge chamber pressure.

The study indicated that magnetic field geometries where the field lines are strictly parallel with the anode surface give rise to the largest anode fall voltages. Under these conditions, if the electrons are to be collected, they must cross the magnetic field lines; thus, electron collection at the anode can occur only by electrons randomly migrating across field lines via collisions. This collisional random walk apparently gives rise to an effective anode sheath resistance as the field increases. The study also found that increasing the divergence of the magnetic field so that the field lines intersect the anode reduced the rate at which the anode fall voltage increased with increasing magnetic field strength. In this case it is believed that the electrons are being guided to the anode's surface by the magnetic field lines. It was speculated that such magnetic field configurations enhanced electron diffusion into the anode thus reducing the need for large anode fall voltages to maintain the discharge at constant current.[3]

The investigations at Stuttgart also determined that the magnetic field also influences the local plasma pressure at the anode. At magnetic field intensities above a critical field strength, pressure at the anode decreased while anode fall voltage increased. This drop in near-anode pressure occuring while the anode fall voltage increases suggests that the anode fall voltage's magnitude may be related to plasma depletion in the near-anode region.

Finally, the study also showed that for a given operating point, there was a lower limit to the anode fall voltage. This lower limit was found to be independent of near-anode pressure. This important finding appears to imply that there exists an unavoidable lower limit to anode losses. This lower limit as the paper suggest may in fact depend on the physical configuration of the MPD thruster itself.[3]

More recently, a study at NASA's Lewis Research Center was conducted to investigate the nature of anode power deposition in MPD thrusters. The study, conducted by George Soulas and Roger Myers, investigated anode power losses using the apparatus shown in Figure 1.6. The water-cooled anode provided the capability of measuring the power flux into the anode. Near-anode plasma properties were measured using a Langmuir probe placed at a fixed position with respect to the anode. The effect of variations in local magnetic field and gas pressure near the anode on anode power deposition was investigated. The interpretation of the experimental results of this study was based on the energy balance relation discussed earlier.[13]

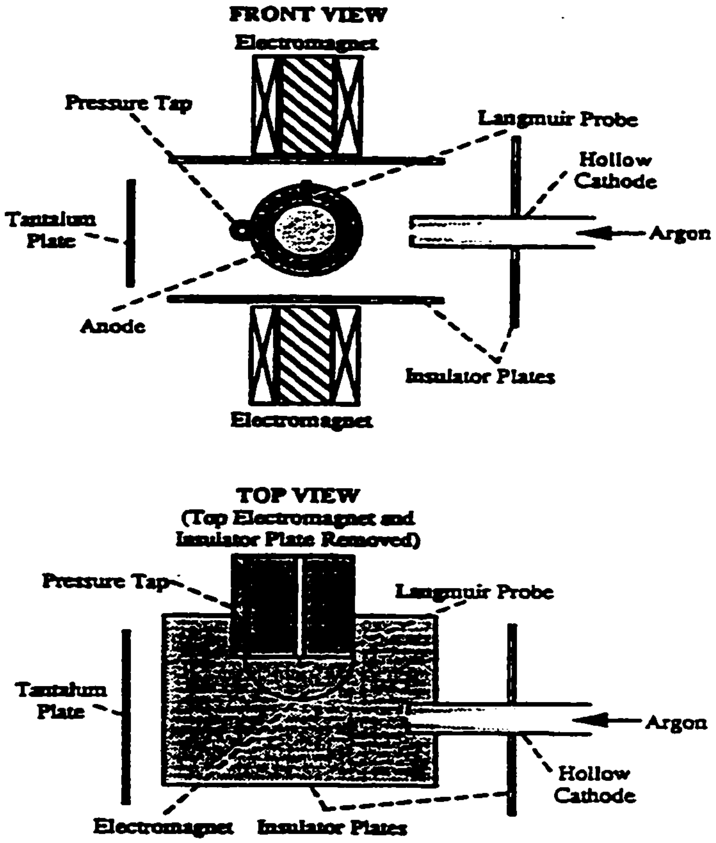

Figure 1.6. NASA Lewis Discharge Apparatus and Diagnostics.[13]

The NASA Lewis study found that at low pressures (< 0.1 Torr), the anode fall and the anode power flux grew monatonically with increases in the applied transverse magnetic field. It was also found that those magnetic field orientations that allowed the magnetic field lines to intersect the anode gave rise to a lower measured anode power flux than that which was observed at the same field strength with the field lines strictly parallel to the anode surface. This observation is consistent with the findings of Schall as discussed earlier. Another finding also similar to the work of Schall was that the anode fall voltage was found to be constant at pressure above 0.1 Torr, regardless of magnetic field strength. Heat flux to anode was shown to increase as the pressure was reduced.[13]

Reduction in anode fall voltage in a pulsed MPD-like device has been reported by a research group at Los Alamos National Laboratories. In a series of conference papers by Scheuer et. al[15], the use of a magnetic nozzle to reduce the anode fall voltage was discussed. This idea is based on "shorting" out the anode sheath by connecting the anode with the adjacent positive column via magnetic field lines. The motivation for the use of the magnetic nozzle to achieve this end is guided by the theoretical findings of Niewood of MIT.[14] Niewood developed a numerical model for the self-field MPD thruster. Results from the model suggest that the Hall effect may be responsible for the large anode fall voltages reported by various MPD thruster experimenters of the past. The interaction of the axial current density, J_{ax}, where $J_{ax} = -\frac{\sigma B_\theta}{en_e} \cdot J_r$, near the anode with the azimuthal magnetic field, B_θ, tends to pinch the plasma toward the thruster axis (see Figure 1.7), thus depleting the near-anode region of charge carriers. Here, σ is the plasma conductivity and J_r is the radial current density. The axial current density can grow as n_e in the near-anode region is reduced due to this plasma contraction toward the axis. Thus growth in J_{ax} depletes the electron population near the anode. This depletion can give rise to the formation of large space charge fields (and thus large anode falls) which may be necessary if the thruster is to operate stably at a given discharge current.

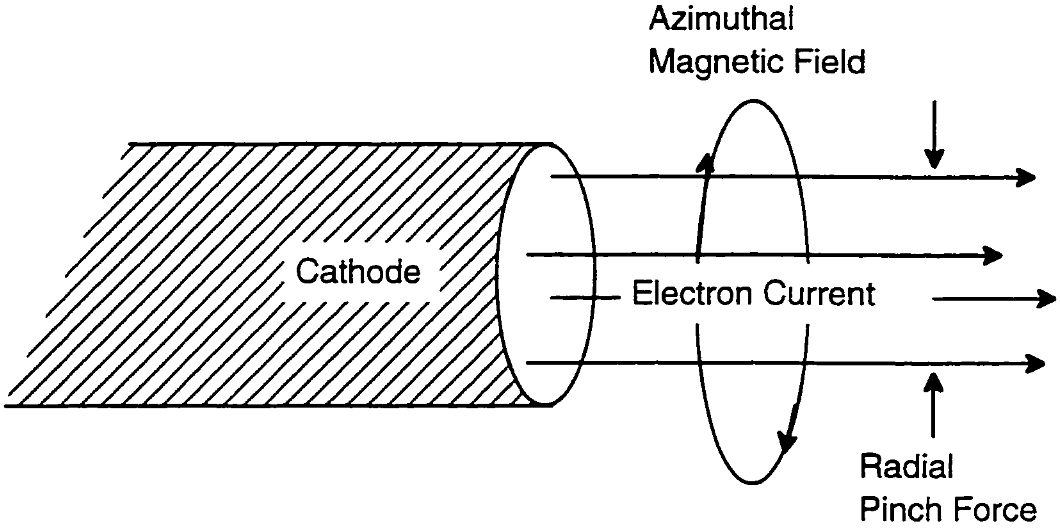

Figure 1.7. The "Pinch" Effect in an MPD Thruster.

The appeal of the magnetic nozzle stems from the following possible benefits: 1.) Electron conduction to the anode is enhanced via magnetic field lines “shorting” the anode sheath; 2.) Electron flux at the anode is more evenly distributed thus enhancing electrode life; and 3.) The applied field leads to the generation of current components that oppose the Hall induced axial currents.[14,15,16]

With the applied field, $B_{z,r}$, of the magnetic nozzle, J_{ax} becomes from the generalized Ohm’s law:

$$J_{ax} = -\sigma \cdot (v_\theta B_r) - \frac{\sigma}{en_e} \cdot (B_\theta \cdot J_r - J_\theta \cdot B_r). \qquad (1.7)$$

Here, It can be seen that the $J_\theta \cdot B_r$ term opposes the Hall term $B_\theta \cdot J_r$, which is responsible for anode plasma depletion. In addition, if the B_r term is sufficiently large, $\bar{E} \times \bar{B}$ motion will tend to rotate the plasma. Here B_r is the radial magnetic field and v_θ is plasma rotational velocity. The rotation gives rise to centrifugal plasma particle motion that tends to reduce near-anode depletion. Experimental measurements of axial current without the magnetic nozzle show that the axial current profiles are similar to those predicted by

Niewood's self-field MPD model. The "tailored" applied field of the magnetic nozzle was shown to reduce the anode fall voltage.[14,15,16]

1.4. Concluding Remarks

As was mentioned in the review section, it is clear that much progress has been made toward isolating macroscopic scaling parameters such as transverse magnetic field and gas pressure that appear to control the relative magnitude of the anode fall voltage. In addition, much progress has also been made in reducing the anode fall voltage in MPD thrusters. Findings related to reducing the anode fall voltage all revolve around minimizing the magnetic field in the near-anode region. In terms of understanding the physical mechanisms for how and why large anode fall voltages form and change as a function of magnetic field, the collective knowledge briefly reviewed is qualitative at best and thus is still incomplete. And although the reduction in the anode fall has been achieved via modifying the near-anode magnetic field environment, the obvious question then arises: What happens to engine performance (thrust production) when these changes are made? Indeed, the anode fall reduction work done at Los Alamos suggests that even though the anode fall voltage was substantially reduced, the thrust power also went down.[17] The experimental approach taken in this thesis to study the problem of the anode sheath in a magnetic field is unique in comparison to previous studies in that it allows the problem to be studied from a vantage point that is independent of other phenomena which would otherwise convolute the findings with influences from other effects (e.g. plasma acceleration). Essentially all previous studies have been done using pulsed MPD engines. In this investigation, near-anode processes are investigated under steady-state conditions. As a result, transient phenomena that are associated with pulsed discharges do not complicate interpretation. In addition, the findings of this study are independent of engine geometry. Further, the investigation is conducted on an apparatus that is well suited for parametric studies. Previous studies concentrated on determining anode fall behavior as a function of thruster parameters. In this respect, the picture is macroscopic and not very general. That is, little emphasis was placed upon characterizing the changes in near-anode plasma properties in response to the transverse magnetic field. Understanding how near-anode plasma processes change in response to the transverse magnetic field is a key aspect of the approach taken in this investigation.

In the chapters that follow, research geared toward understanding what the underlying physical mechanisms responsible for the formation and growth of the anode fall voltage as a function of transverse magnetic field intensity are presented. Because in general the problem of a sheath in the presence of a transverse magnetic field is still not completely understood, these studies can shed light on a relatively old problem.[18] For once this knowledge is completely obtained, only then can one can then go forward in a deliberate fashion to reduce the anode fall without sacrificing engine performance.

Notes to Chapter 1

[1] R.G. Jahn . The Physics of Electric Propulsion (McGraw-Hill Book Company, New York, 1968). Chapter 1: pp. 5-9, Chapter 8: pp. 237-239.

[2] A.D. Gallimore, R.M. Myers, A.J. Kelly, R.G. Jahn, Proceedings of the AIAA 27th Joint Propulsion Conference, AIAA 91-2343, (American Institute of Aeronautics and Astronautics Press, Washington D.C. 1991).

[3] S. Wolfgang, Proceedings of the AIAA 9th Electric Propulsion Conference, AIAA-72-502, (American Institute of Aeronautics and Astronautics Press, Washington D.C., 1972).

[4] Y.P. Raizer, Gas Discharge Physics (Springer-Verlag, New York, 1991), Chapter 4, Sec. 4.6, pp. 68-71, Chapter 10, Sec. 10.2: pp. 246-247, Sec. 10.7: pp. 266-267.

[5] S.C. Haydon, Editor, J.M. Somerville, Contributing author, Discharge and Plasma Physics (University of New England Press, Australia, 1964), Chapter 17, pp. 238-244.

[6] H. Hugul, IEEE Transactions on Plasma Science. Vol. PS-8, No. 4, December (1980).

[7] F. Chen, Introduction to Plasma Physics and Controlled Fusion (Pergamon Press, New York, 1984).

[8] P. Strangeby, Physics of Fluids,vol. 27, no. 3, 682, March (1984).

[9] J.D. Cobine and E.E. Burger. Journal of Applied Physics. vol. 26, no. 7, July (1955).

[10] K.T. Shih and E. Pfender. AIAA Journal. vol. 8, no. 2, Feburary (1970).

[11] H. Tahara, M. Sasaki, Y. Kagauya, and T. Yoshikawa, Proceedings of the 1990 21st International Electric Propulsion Conference, July 18-20 Orlando, AIAA 90-2554, (AIAA Publishing, Washington D.C., 1990).

[12] A.D. Gallimore, Ph.D. Thesis, Department of Mechanical and Aerospace Engineering, Princeton University, 1992.

[13] R.M. Myers and G. Soulas. Proceedings of the 23rd Inrternational Electric Propulsion Conference, IEPC 93-194, (The Electric Rocket Society Press, Columbus OH, 1993).

[14] E.H. Niewood and M. Martinez-Sanchez, Proceedings of the 1991 22st International Electric Propulsion Conference, IEPC-91-099, (AIAA Publishing, Washington D.C., 1991).

[15] J.T. Scheuer et al., Proceedings of the AIAA 23rd International Electric Propulsion Conference, IEPC 93-118, (The Electric Rocket Society Press, Columbus OH, 1993).

[16] R.P. Hoyt et al., Proceedings of the AIAA Joint Propulsion Conference, AIAA 91-2343, (American Institute of Aeronautics and Astronautics Press, Washington D.C. 1991).

[17] Private communication. R.M. Mayo, North Carolina State, Dept. of Nuclear Engineering.

[18] U. Daybelge and B. Bein, Phys of Fluids, 24, (1), (1981).

CHAPTER 2

EXPERIMENTAL HARDWARE AND PROCEDURE

2.1. Experimental Set-Up

The discharge apparatus, illustrated in Figure 2.1, used in this investigation is mounted in a 1 meter diameter by 1.2 meter long cylindrical vacuum chamber that is evacuated by a NRC rotary gas ballast mechanical pump with a pumping speed of 400 cubic feet per minute. As measured by the chamber thermocouple gauge, once the ultimate pressure of 30 mTorr is reached, the tank is then filled to roughly one Torr of argon and flushed several times before the discharge is ignited. Typical operating pressures with the discharge on ranges between 40 and 50 mTorr.

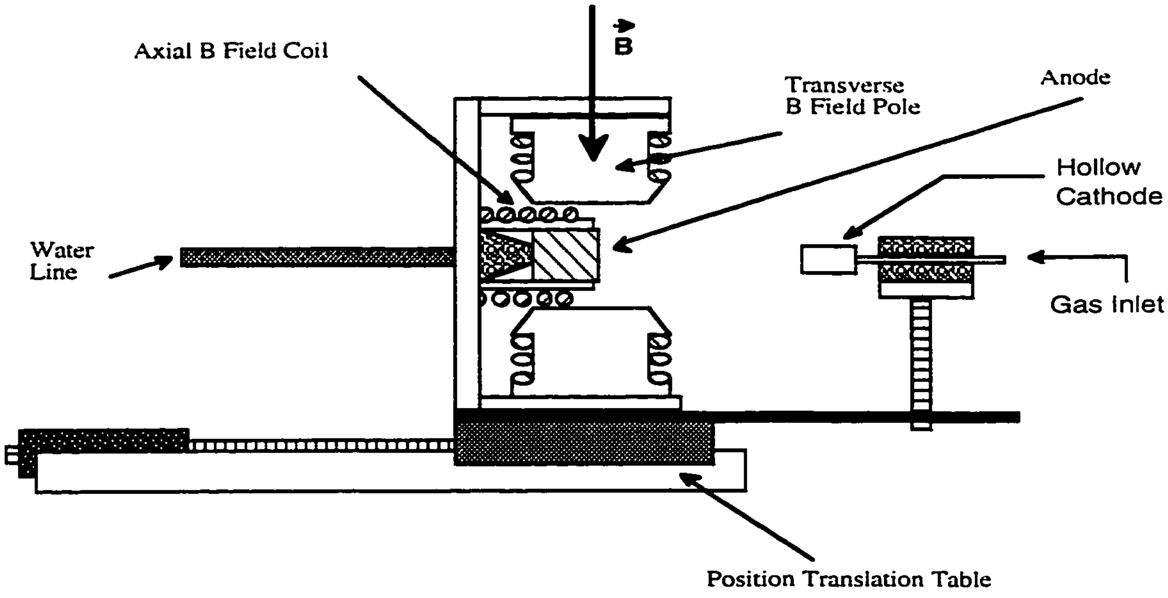

Figure 2.1. Discharge Apparatus.

A gas-fed hollow cathode of the type utilized in many electric propulsion systems is used as the electron source for the discharge. Argon is the working gas for all experiments. The water-cooled anode is a stainless steel 2.5 cm diameter disk which is thermally and electrically isolated from the electromagnet gantry that it is mounted to. The anode is placed within an alumina sleeve such that its only exposed surface is the front plane facing the cathode. For those experiments utilizing the water-cooled anode, the inter-electrode gap is set to 6.0 cm. The temperature of the anode is monitored via thermocouples attached to the rear of the electrode. The electromagnet, with its shaped pole pieces, immerse the anode and the near-anode region in a uniform magnetic field with the flux lines running parallel to the anode's surface. The uniform magnetic field extends to over three centimeters above the surface of the anode. Though for this investigation the largest field strength utilized was just over 120 Gauss, the electromagnet is capable of generating field strengths in excess of 200 Gauss. The entire discharge apparatus is mounted to a position translation table which allows the discharge to be displaced relative to fixed probes so that spatial plasma measurements could be made.

The discharge is initiated by first pre-heating the hollow cathode to remove surface impurities and to condition the cathode for emission. Next, high voltage is applied between the cathode and a tantalum auxiliary electrode. Once ignited, the arc is transferred to the stainless steel anode and is operated in a constant current mode. After the transfer, the initial attachment at the anode usually consists of a very localized spherical spot at the anode surface. It has been found that a weak transverse magnetic field of ~ 7 G tends to smear out the spot so that the attachment at the anode is uniform. Though a subject of another investigation, the mechanism behind the formation of this initial anode spot may be due to anode surface non-uniformity which tends to concentrate the electric field locally. The transverse magnetic field acts to smear out these effects because it limits transverse diffusion, thus forming a smooth, more uniform anode-plasma collection surface so that local anode spot attachments are no longer favored. In other words, because transverse electron flux decreases with increasing magnetic field, a localized attachment at the anode can no longer be supported and thus in order to sustain the discharge at constant current, electron collection must take place over a larger portion of the anode's surface.

For this work, the arc is maintained by a discharge current flowing between the cathode and anode. The anode current densities investigated in this study are on the order of $2\ \frac{A}{cm^2}$, which simulates conditions at the anodes of steady-state 100 kW class MPD thrusters.[1]

This study utilizes invasive Langmuir probe techniques, non-invasive emission spectroscopy methods, and water calorimetry. The Langmuir probe used in this investigation consists of a 3 mm long tungsten wire that is 0.2 mm in diameter. The unexposed portion of the tungsten wire is isolated from the discharge via an alumina sheath. Unless otherwise stated, the probe is oriented such that its axis is parallel with the magnetic field lines. The location of the probe above the anode surface varied from 1 mm to 8 mm, depending on the experiment. For the near-anode characterization studies discussed in Chapters 3-5, the probe was located 2.5 mm above the anode surface. The probe is connected to a programmable bipolar power supply that is driven by a signal generator so that a triangle wave of a few Hertz is applied to the probe. The measured probe voltage and current are then sent to an operational amplifier which in turn sends the signals to a Tektronix digital oscilloscope. The purpose of the digital oscilloscope is to acquire the traces so they can be extracted and stored onto a PC via a National Instruments GPIB interface. In addition to standard Langmuir data, electron energy distribution data are also taken. To make the EEDF measurements, an additional signal generator is used to superimpose a 1 kHz, 1 V sine wave on the probe voltage. The probe current signal is then sent to a digital, dual phase Stanford Research lock-in amplifier which is set to lock-in on frequencies at the second harmonic of the signal 1 kHz superimposed signal. The lock-in amplifier's output is then sent to the oscilloscope. The entire set-up including the computer is plugged into isolation transformers. A block diagram of the Langmuir probe circuit is illustrated in Figure 2.2. All Langmuir probe voltage measurements are made with respect to the anode. Representative plots corresponding to standard Langmuir probe measurements and electron energy distribution function (EEDF) measurements are illustrated in Figures 2.3a and 2.3b respectively.

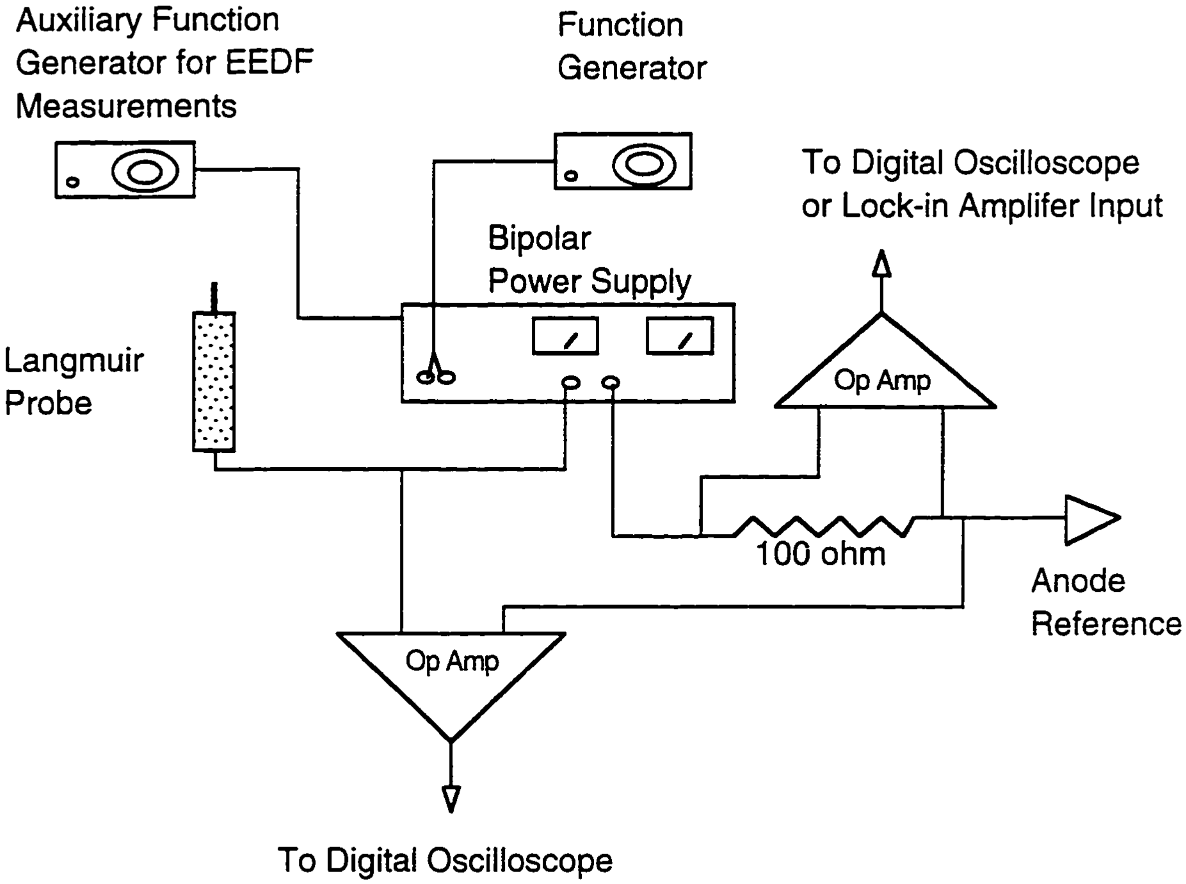

Figure 2.2. Langmuir Probe Circuit.

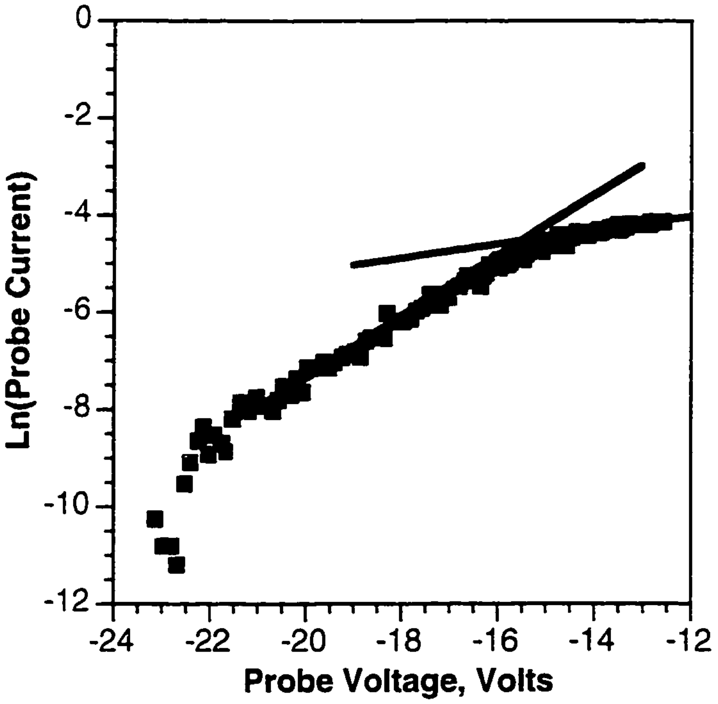

Figure 2.3a. Sample Langmuir Probe Trace.

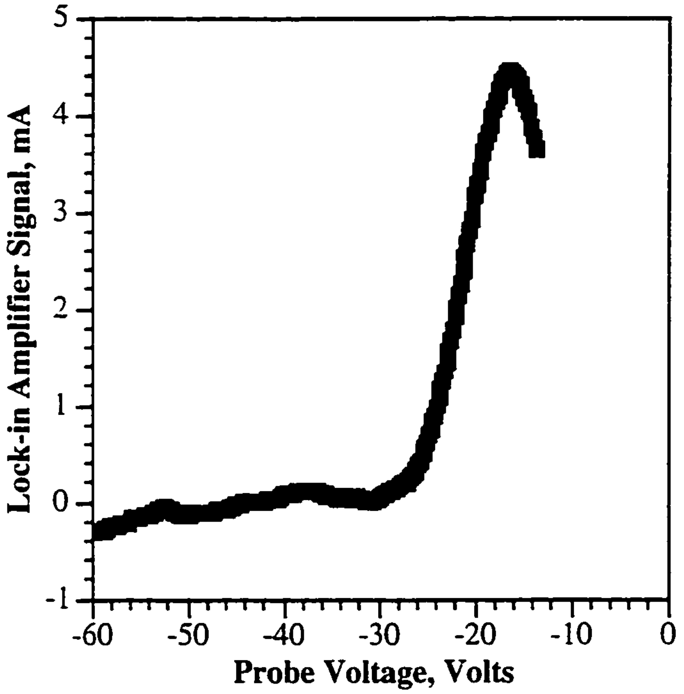

Figure 2.3.b. Sample EEDF Signal from Lock-in Amplifier.

The emission spectroscopy set-up (Figure. 2.4) consisted of an iris, a concave/convex doublet, and a Spex 500M 0.5 m spectrometer fitted with a 1800 groove/mm holographic grating. The spectrometer scanned for argon neutral and ion lines located between 470 nm and 481 nm.

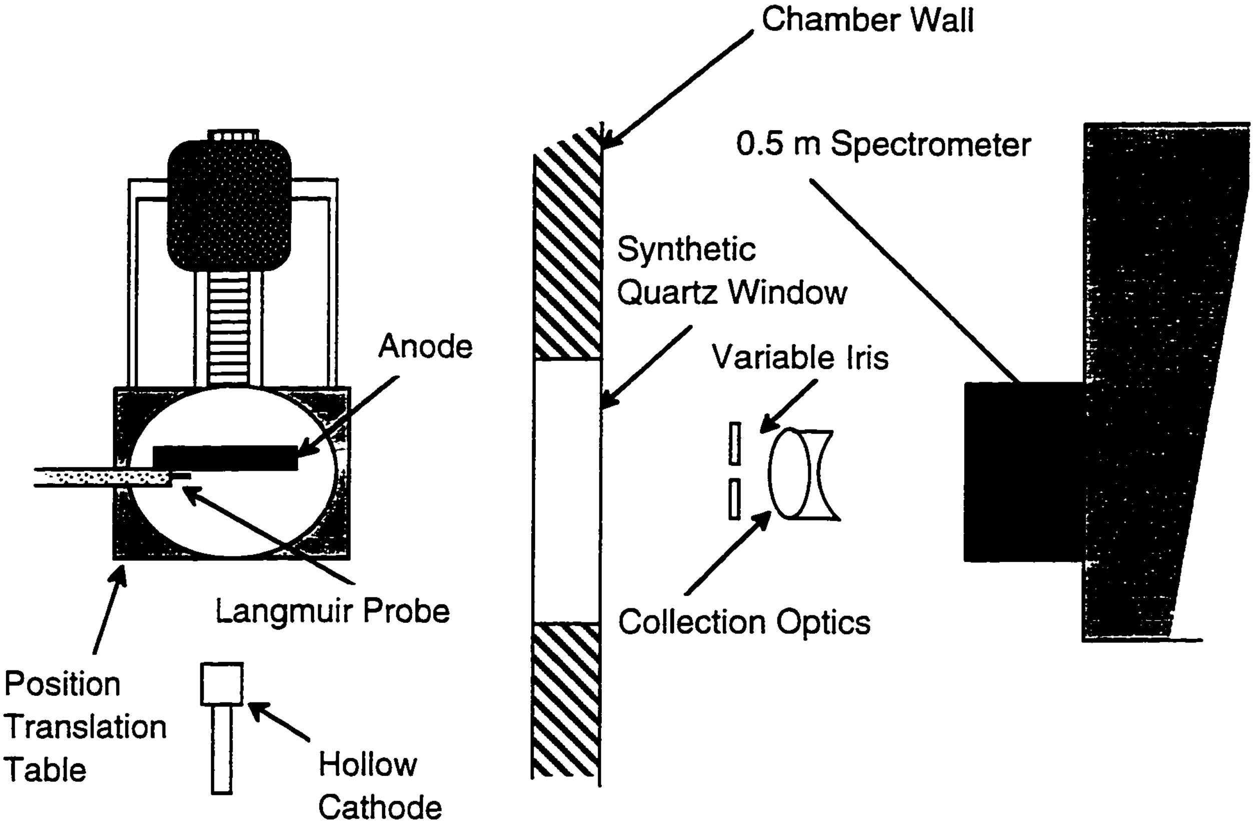

Figure 2.4. Emission Spectroscopy Set-up.

Water calorimetry (see Figure 2.5) is used to determine the rate at which energy is deposited into the anode. By measuring the temperature of the water entering the anode, the temperature of the water exiting the anode, and the water mass flow rate ($\dot{m}$), the rate at which heat is deposited into the anode can be calculated with:

$$\frac{dQ}{dt} = c_v \cdot \dot{m} \cdot \Delta T. \tag{2.1}$$

Here c_v is the specific heat of water at constant volume and ΔT is the water temperature change. The cooling water is provided by a Neslab recirculating chiller with a cooling capacity of 950 Watts. The water flow-rate is measured by a standard spring loaded water flow meter. Though the main utility of the water calorimetry resides in the expedition of the heat flux measurements, it also afforded the opportunity to minimize electrode evaporation by maintaining an anode temperature of no more than a few hundred degrees Celsius as measured from a thermocouple attached to the back surface of the anode.

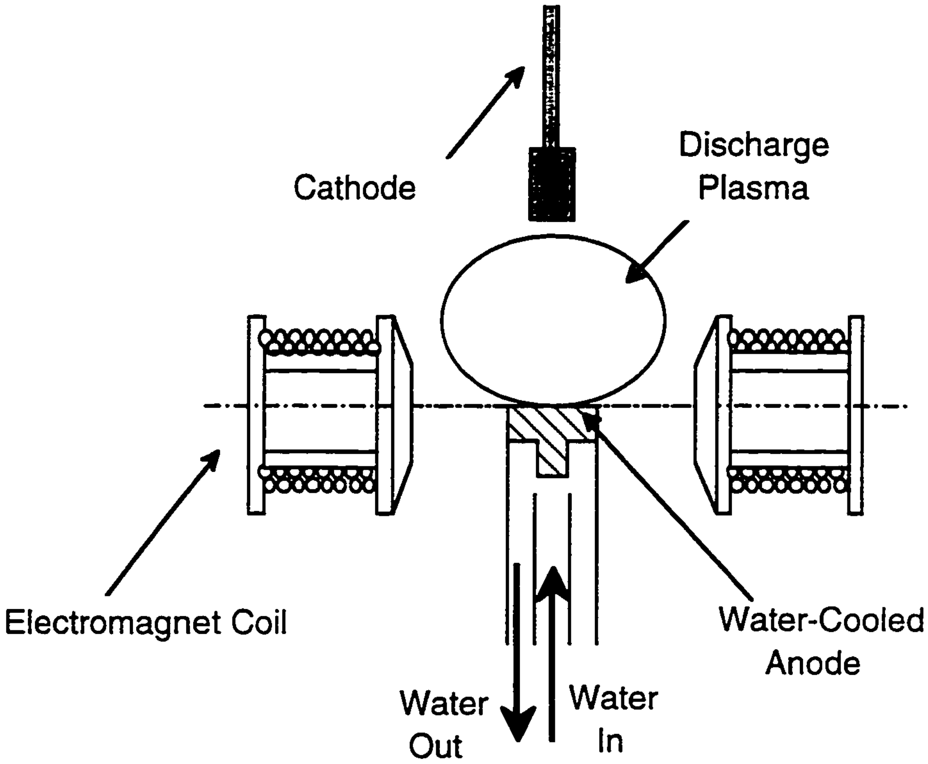

Figure 2.5. Simplified Schematic of Discharge Apparatus.

2.2. Langmuir Probe and Emission Spectroscopic Analysis

Langmuir probe data are acquired as mentioned above by recording collected plasma current as a function of imposed probe voltage. Because the ratio of the probe radius is over an order of magnitude greater than the Debye length, thin sheath analysis applies. The electron number density is obtained from the ion saturation current via the relation:

$$i_+ = 0.61 \cdot e \cdot n_e \cdot \sqrt{\frac{Z_i \cdot kT_e}{M_i}}. \tag{2.2}$$

Here e is elementary charge of an electron, n_e is the electron number density, Z_i is the charge state of the ion species, k is Boltzmann's constant, T_e is the electron temperature, and M_i is the mass of the ion. Because the ion Larmor radius for operating conditions in this experiment is large compared with probe dimensions, magnetic effects are not expected to significantly impact the density measurements. The electron temperature is found by obtaining the slope from the most linear region of a semi-log plot of the electron current versus probe voltage for those voltage values near the floating potential. The electron temperature is then the reciprocal of this slope if the electron energy distribution is Maxwellian. The plasma potential is obtained by locating the "knee" in the collection region of the semi-log plot. In general, the intersection of the electron retarding region and the electron saturation region is taken to be the "knee."[2]

The electron energy distribution function is obtained by using the widely accepted technique of superimposing a small signal onto the probe voltage.[3] A subsequent Taylor expansion of the measured probe current yields terms which are proportional to the various derivatives of the probe current. Recall that the electron energy distribution function is proportional to the second derivative of the probe current:[4]

$$f(E) \propto \sqrt{E} \cdot \frac{d^2 I_p}{dV_p^2} . \qquad (2.3)$$

In the Taylor expansion of the probe current, the second derivative term is proportional to the term containing the second harmonic of the small input ac signal. It is then a simple matter to obtain this second harmonic via a lock-in amplifier. The estimated error in the EEDF measurements is approximately 8%.[5] Most of the uncertainty in the EEDF measurements is associated with higher order derivatives that contribute to the signal detected by the lock-in amplifier.

Experimental electron energy distribution functions, $f(E)$, can be fitted to the following relation:

$$f(E) = C \cdot \sqrt{E} \cdot \exp(-BE^n) . \qquad (2.4)$$

Here E is the electron energy, C is a normalization factor, and B and n are fitting parameters. A Maxwellian distribution corresponds to an n value of one while a Druyveststyn distribution corresponds to an n value of two.[4] Using this model for the electron energy distribution function, one can ascertain the nature of the distribution. Indeed, from a semi-log plot of the lock-in signal versus probe voltage one can determine the nature of n. For example, if the plot of the $Ln|A(E)|$ versus energy, where A(E) is the lock-in signal, is linear then the EEDF is Maxwellian. Once n is known, B and a constant proportional to C can be obtained from a semi-log plot of Ln(A(E)) versus energy raised to the appropriate power.

Emission spectroscopic measurements were carried out using the apparatus shown in Figure 2.4. One important aspect of the spectroscopic measurements is that of monitoring the growth or decay of the energetic electron population:

$$\frac{I}{n_e} = const.\cdot \int_{E_T}^{\infty} \sqrt{\frac{2E}{M}}\,\sigma(E)\cdot f(E)dE. \qquad (2.5)$$

Here the ratio of the intensity, I, of a particular argon line to the local electron number density, n_e, measured in the imaged region is proportional to the excitation rate for that transition which in turn is proportional to the fraction of those electrons with energies above the excitation threshold for that transition as determined by integrating over the electron energy distribution function, $f(E)$. Here $\sigma(E)$ is the excitation cross section as a function of energy, E, and M is the mass of the emitting argon atom or ion. The excitation threshold, E_T, for the excitation of argon neutral lines is roughly 14.5 eV, whereas the excitation threshold for the excitation of argon ion lines is about 35 eV.[6] These emission spectroscopy measurements, therefore, complement the EEDF measurements.

2.3. Error Analysis

2.3.1. Langmuir Probe Measurements Error

Plasma parameters such as the electron temperature, electron number density, plasma potential, and the electron energy distribution function (EEDF) calculated in this investigation are subject to error associated with uncertainty in the measuring electrostatic probe. Under ideal conditions, the Langmuir probe does not disturb surrounding plasma appreciably and the plasma parameters measured reflect the plasma in the region where the probe is located. The non-perturbing nature of the probe is true as long as the probe potential relative to the plasma potential is shielded from appreciable penetration into the bulk plasma. This condition is usually assured by the presence of a space charge sheath that encapsulates the probe and confines appreciable potentials to within its volume. The probe will reflect properties of the plasma outside the sheath if collisional and ionization events are infrequent inside the sheath. However, significant error can arise if there exists appreciable gradients along the body of the probe.[7] In essentially all situations investigated in this study, errors associated with these problems are minimal due to the fact that: 1.) $r_p < l_e$, 2.) $r_p >> \lambda_d$, 3.) $r_p < r_l$, where r_p is the probe radius, l_e is the electron mean free path, λ_d is the Debye length, and r_l is the electron Larmor radius.

As discussed earlier, there are a number of possible error sources associated with probes in an unmagnetized plasma. Because this investigation studies plasma conditions under the influence of an appreciable magnetic field, interpretation of probe measurements must account for this. In the case of determining the electron temperature, magnetic field effects can be ignored provided the field strengths are not too strong (<1 kG) and the probe is sufficiently negative. For a suffiently negative probe, the electrons collected will be described by the Boltzman factor: $n_e = n_\infty \cdot \exp\left[\frac{e\phi}{kT_e}\right]$, where ϕ is the potential of the probe relative to a reference.[9] These electrons collected in the high energy tail of the EEDF provide a sufficient sampling of the energy distribution to yield a temperature. In addition, the Larmor radius of these energetic electrons is much larger than the bulk electrons. In this respect, their motion is only weakly magnetized. Error in the electron temperature measurements for the most part is asociated with the uncertainty in the least significant digits of the probe voltage and current. This average error is estimated to be on the order of 10%.

Because the magnetic field reduces the transverse flux available to the probe, the electron saturation current becomes a function of the magnetic field. From this standpoint, the electron saturation current can no longer be used to obtain the electron number density.[8] Instead, the ion saturation current must be used to determine electron number density. As stated earlier, for weak to moderate fields (0-1 kG) with cold to warm ions (0-10 eV), ion motion unlike the electron motion, is not appreciably influenced by the magnetic field. In this respect, when evaluting Equation 2.5, magnetic field effects can largely be ignored and density may then be obtained by solving this relation given the electron temperature and the ion saturation current. Uncertainty in the electron number density depends on the uncertainty in the determination of the electron temperature and the ion saturation current. The ion saturation curent is evaluated at the knee of the the current-voltage trace in the ion collection region. The error in the ion saturation then depends on the confidence in the location of the knee (see Figure 2.6). The knee is found by fitting a line to the linear portion of the ion current region and a parabola to the rounded portion and determining their intersection or closest approach. The arbitrariness of the location of the knee coupled with the uncertainty in the electron temperature gives rise to a total uncertainty of roughly 50%. This uncertainty is consistent with expected density uncertainty stated in the literature.[10,11]

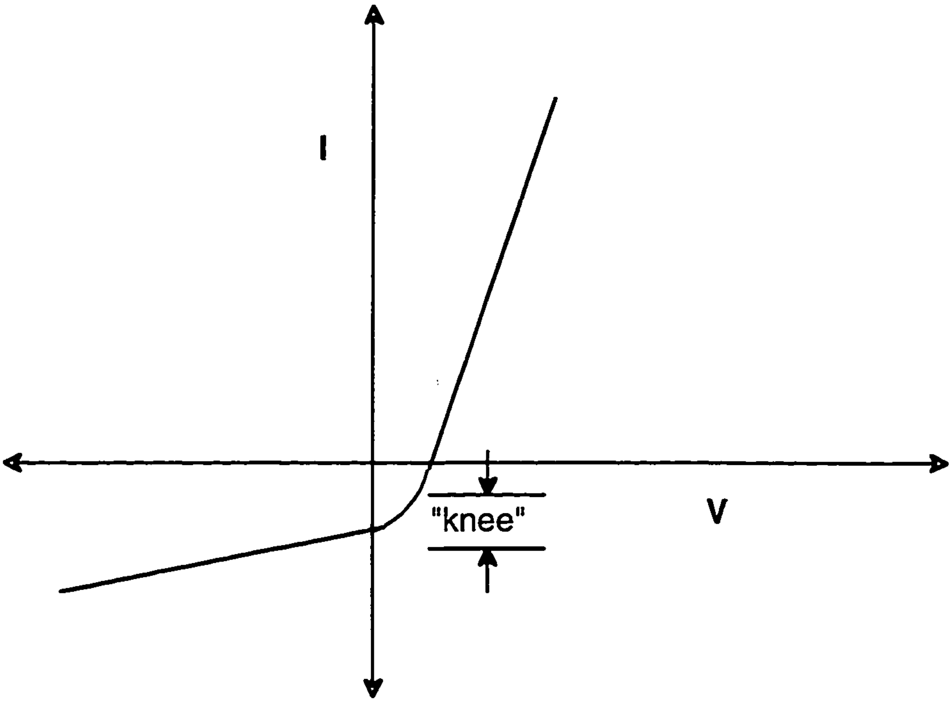

Figure 2.6. Determining the Electron Density via the Ion Saturation Region.

Besides the above mentioned effects, other uncertainties in probe measurements also exist. For example, the plasma potential is usually determined by locating the knee of the electron collection portion of the Langmuir probe trace. By fitting lines to the saturation and the retarding regions, a knee which corresponds to the plasma potential can be readily found. Error in the probe potential, however, must be considered. Because the probe in this investigation is made of tungsten and the anode reference electrode is made of stainless steel, a contact potential difference exists due to unequal work functions. This disparty along with the fact that the stainless steel is made up of several metals with several different work functions yields an uncertainty of roughly 1 Volt in the plasma potential measurement.

2.3.2. Error Analysis in Power Deposition Measurements

Error associated with the water calorimetry measurements can be quantified by identifying uncertainties associated with the calculation of $\frac{dQ}{dt}$ and summing them. The primary experimental uncertainties associated with power deposition measurements lie in determining the change in temperature of water as it flows through the anode . The thermocouple controller used with the type K thermocouple could measure reliably changes in water temperature as small as 0.6 C according to Omega, the thermocouple controller manufacturer. This gives rise to an uncertainty in the calculated $\frac{dQ}{dt}$ of order $c_p \cdot \dot{m} \cdot (0.6)$. The smallest dectectable change in the water flow rate that could be dectected using the Omega flow meter was 0.005 gal/min. The total uncertainty then becomes $\left[\left[\frac{\delta(\Delta T)}{\Delta T} + \frac{\delta(\dot{m})}{\dot{m}}\right] \cdot 100\right]\%$. This error depended on operating condition and ranged from 15% to 20%.

2.3.3. Spatial Resolution and Positioning Error for Emission Spectra Measurements

The intensity of various argon emission lines was spatially mapped by stepping the entire discharge relative to a fixed set of imaging optics. The spatial resolution associated with the translation stage used to displace the discharge was one micrometer. With the spectrometer entrance slit set at 10 micrometers and an optics demagnification of 0.15, the actual width of the point imaged corresponded to a plasma slice of thickness 0.07 mm. This length scale corresponds to the smallest disturbance or structure that can be resolved by this set-up. This thickness ranged from 2 to 10 Debye lengths depending on local electron density and temperature in the vicinity of the imaged point. The actual position of the slice being imaged was set using a He-Ne laser. The laser beam was positioned so that it was parallel to the surface of the anode. Next the anode was displaced so that it intersected roughly half the laser spot. This spot size, which was 0.5 mm in diameter, correponded to roughly a position uncertainty of roughly 0.25 mm (half the laser beam diameter).

Notes to Chapter 2

[1] A.D. Gallimore, R.M. Myers, A.J. Kelly, and R.G Jahn. Proceedings of the AIAA 22st Joint Propulsion Conference, AIAA 91-2343, (American Institute of Aeronautics and Astronautics Press, Washington D.C., 1991).

[2] J. Swift and M. Schwar, Electrical Probes for Plasma Diagnostics (Llife Books, New York, 1970), Chapter 1, Sec. 1.5: pp. 9-15 and Chapter 12, Sec. 12.6: pp. 259-263.

[3] H. W. Rundle, D.R. Clark, and J.M. Dechers, Canadian Journal of Physics, vol. 51, (1973).

[4] M.T. Druyvesteyn. Z. Phys, 24, 781 (1930).

[5] J.E. Heidenreich III, J.R. Paraszczak, M. Moisan, and G. Sauve. J. Vac. Sci. Technol. B 6(1) Jan./Feb. (1988).

[6] T.L. Cox, V. G. I. Deshmukh, D.A.O. Hope, A.J. Hydes, N. St. J. Draithwaite, and N.M.P. Benjamin, J. Phys D: Appl. Phys.,20, 820, (1987).

[7] L.B. Loeb, Basic Processes of Gaseous Electronics (University of California Press: Berkeley, 1955), Chapter 4, Sec. 8, pp. 361-370.

[8] R.H. Huddlestone and S.L. Leonard, Editors, Francis Chen, Contributing author, Plasma Diagnostic Techniques, (Academic Press, New York, 1965), Chapter 4, Sec. 5, p. 163.

[9] I.H. Hutchinson, Principles of Plasma Diagnostics (Cambridge University Press, New York, 1987), Chapter 3, Sec. 3.3, p. 66.

[10] V.A. Godyak, R.B. Piejak, B.M. Alexandravich, J.Appl. Phys., vol. 73, no. 8, 15, 3657 April (1993).

[11] D. Tilley, A.J. Kelly, R. Jahn, Proceedings of the AIAA 21st International Electric Propulsion Conference, AIAA 90-2667, (American Institute of Aeronautics and Astronautics Press, Washington D.C., 1990).

CHAPTER 3

CHARACTERIZATION OF THE NEAR-ANODE REGION AS A FUNCTION OF TRANSVERSE MAGNETIC FIELD

3.1. Introduction

Characterizing the near-anode region as a function of transverse magnetic field is key to understanding the role that the transverse magnetic field plays in driving energy loss processes at the anode. Past studies done on the electromagnetic thruster known as the magnetoplasmadynamic (MPD) thruster have shown that power losses to the anode can be as high as 70% of the input discharge power.[1] Power losses at the anode of MPD thrusters have been shown to be related to the magnitude of the transverse magnetic field inside the discharge chamber.[2] Schall investigated the effect of magnetic field orientation relative to the anode on anode fall voltage and on anode power deposition in MPD thrusters.[3] In addition, Tahara et al. studied the effect of an axial magnetic field on thrust production and thruster discharge stability.[4] Gallimore et al. correlated anode fall growth with increases in the near-anode Hall parameter, a ratio of the electron cyclotron frequency to the electron collision frequency, in a self-field pulsed MPD thruster.[5] More recently, Scheuer et al. utilized an applied-field magnetic nozzle to reduce the anode fall voltage in an MPD device.[6] The relevance of this characterization study to MPD thruster research is related to the fact that an understanding of the behavior of the near-anode plasma under MPD thruster discharge-like conditions is important in that it can provide insight into why the large anode sheath voltages develop in the first place.

Characterization of the near-anode plasma as a function of the transverse magnetic field can yield important insights into the relationship between the magnetic field and the anode fall voltage. The focus of such an investigation would thus concentrate on how plasma properties themselves are related to the formation and growth of the anode fall voltage as a function of transverse magnetic field with the objective being to relate this microscopic viewpoint to the macroscopic one which includes an understanding of anode power deposition in actual MPD thrusters. From this, conclusions based on phenomenological arguments that relate changes in paramaters such as near-anode electron number density and electron flux with the evolution of anode sheath voltage can be drawn.

For the most part, many of the past studies attribute the depletion of charge carriers as the main reason for anode fall growth.[3,6,7] In this study, the changes in the charge carriers in the near-anode region are characterized as a function of the transverse magnetic field. In this respect, this study investigates long held suspicions concerning near-anode charge carrier depletion and the associated growth in the anode fall region as a function of the transverse magnetic field using an apparatus that is well adapted for parametric studies. Another important aspect of this study is related to the fact that the experimental set-up allows for the study of the variations of the near-anode plasma as a function of the transverse magnetic field at a fixed discharge current. In pulsed, self-field thruster studies, the magnitude of the magnetic field cannot be varied independently of the discharge current, and hence electron temperature, electron number density, pressure, etc.

3.2. Theory and Motivation

As mentioned earlier, an understanding of why the large anode sheath potentials arise and grow with the transverse magnetic field is important to the electric propulsion community. Such large potentials give rise to lower engine performance because power that could be channeled into thrust production processes is instead deposited into the anode as waste heat.

In general, the potential distribution that defines the magnitude and sign of the anode fall region is determined by the space charge distribution in the near-anode region through Poisson's equation. The transverse electron flux at the anode sheath boundary in turn determines the steady-state space charge distribution throughout the anode sheath. This transverse flux, Γ_e, is ultimately controlled by the transverse magnetic field:

$$\Gamma_e = -D_\perp \cdot \frac{dn_e}{dz}, \tag{3.1}$$

where the transverse diffusion coefficient, $D_\perp$, is represented classically by :

$$D_\perp = \frac{D}{1+\frac{\omega_{ce}^2}{\nu^2}}, \tag{3.2}$$

though for many experiments the empirically derived relation of Bohm better describes the experimental observations:

$$D_\perp = \frac{kT_e}{16 \cdot eB}. \tag{3.3}$$

Here, $\frac{dn_e}{dz}$ is the electron density gradient, ω_{ce} is the electron cyclotron frequency, ν is the electron collision frequency, k is Boltzmann's constant, T_e is the electron temperature, e is the elementary charge, D is the diffusion coefficient, and B is the transverse magnetic field.[8] It is this relationship between the magnetic field and transverse flux that ultimately controls the anode fall voltage.

The plasma discharge can be expected to be stable so long as the ratio of the available current from the plasma, $e \cdot \Gamma_e \cdot A$, where A is the effective electrode collection area, to the discharge current, I_d, is of order unity or greater. In order to test the above mentioned assertions, Langmuir probes have been employed to measure the electron number density and the corresponding anode fall voltage as a function of the transverse magnetic field strength. The probes are also used to make electron energy distribution measurements so that ionization rates can be calculated. Correlations in the calculated ionization rates and transverse magnetic field can be in turn related to changes in anode fall voltages. Emission spectroscopy is also used to validate electron energy distribution measurements in the tail of the electron energy distribution function (EEDF). Finally. changes in measured anode power flux as a function of transverse magnetic field strength are determined so that the magnitude of larger anode fall voltages can be put into perspective from a power balance standpoint.

3.3. Experimental Considerations

For this investigation. a 9.25 A arc is maintained between the cathode and anode. This operating point gives rise to an anode current density of roughly 2 $\frac{A}{cm^2}$, which simulates conditions at the anodes of steady-state 100 kW class MPD thrusters.[1]

3.4. Results and Discussion

3.4.1. Anode Fall and Electron Density Variations with Magnetic Field

In general, one major aspect of this study is essentially to characterize how the anode sheath potential, known as the anode fall, varies with transverse magnetic field. This measurement is expedited by determining the plasma potential near the anode surface. If the potential variation across the positive column is fairly flat, then this technique can be used to approximate the anode fall. In this study, error in the anode fall measurements using this procedure was calculated to be less than 10% (see Chapter 2, Section 2.3.2). Positive anode fall voltages as referred to here are associated with an electron attracting anode. As is seen from an examination of Figure 3.1, the anode fall voltage is not strictly a monatonically increasing function of magnetic field as would be expected. What instead is observed is a local maxima in the anode fall voltage where additional increases in transverse magnetic field result in an abrupt decrease in the anode fall. After the sudden drop, it is observed that the anode fall voltage increases with magnetic field but at a much slower rate than before. The region where the anode fall increases with increasing transverse magnetic field appears to be in part related to the decrease in available electron flux which in general should drop off as $\frac{1}{B}$ for Bohm-like diffusion or $\frac{1}{B^2}$ for classical diffusion.[8] It appears that other mechanisms may be at work to increase available flux in the near-anode region for those

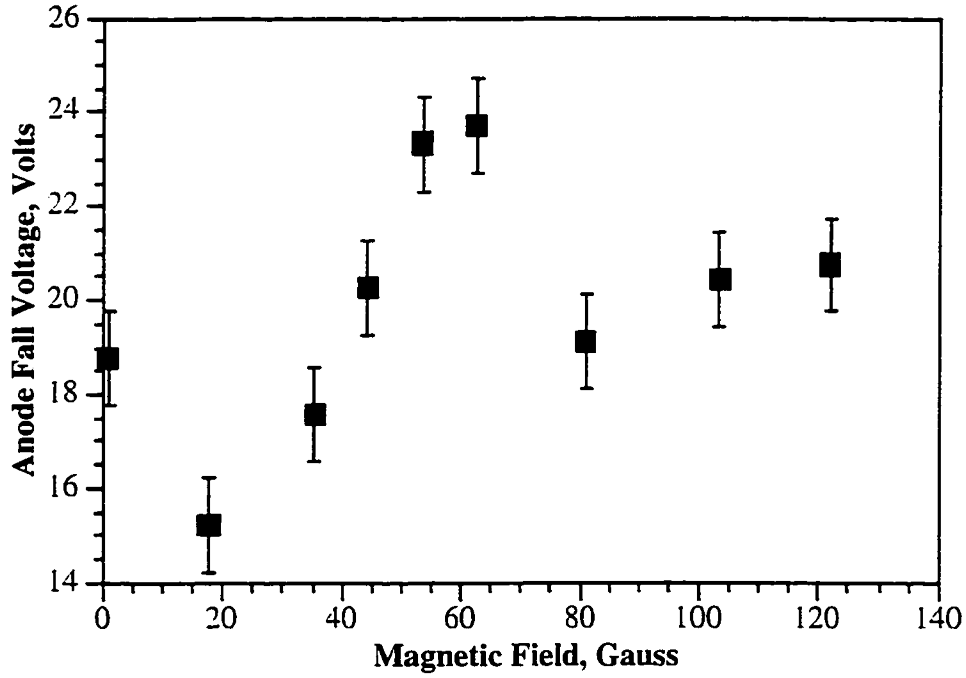

Figure 3.1 Variations in Anode Fall as a Function of Transverse Magnetic Field.

transverse field strengths that correspond to values beyond the anode fall maximum. In general, the magnitude of the available electron flux depends on ionization phenomena taking place in the main discharge column. This ionization is expected to be a function of the EEDF which in general varies with bulk discharge conditions such as pressure, magnetic field, and discharge voltage. The transverse diffusion flux determines the steady-state value of the electron number density throughout the column and up to the anode sheath edge. The measured electron density near the sheath edge reflects the behavior of the available transverse flux with the changes in magnetic field. This relationship follows from the scaling between the charge production rate, density, and flux: $n_e \propto \dot{n}_e \propto \Gamma_e$. Here $\dot{n}_e$ is the charged pair production rate. This behavior is illustrated in Figure 3.2 where the available transverse current is shown to vary linearly with electron number density. Here the available transverse current is approximated by using experimentally determined plasma parameters in the relation derived by Sugawara:

$$I_{e\perp} = \frac{1}{4} e n_o \bar{v} \cdot A_p \cdot [\frac{16}{3} \cdot \frac{\lambda_e \cdot \alpha^{\frac{1}{2}}}{K(k) \cdot r_o}] \cdot \frac{1}{[1 + \frac{16}{3} \cdot \frac{\lambda_e \cdot \alpha^{\frac{1}{2}}}{K(k) \cdot r_o}]}, \tag{3.4}$$

which describes the saturation current available to a planar probe for a given magnetic field strength.[9] Here, λ_e is the electron mean free path, r_o is the anode radius, A_p is the anode surface area, n_o is the electron number density, and K(k) is the elliptic integral of the first kind. The variable α is the classical relation for the ratio of the transverse diffusion coefficient to the diffusion coefficient when the magnetic field is zero. This quantity is proportional to the reciprocal of the square of the Hall parameter in the limit of large magnetic field strength.

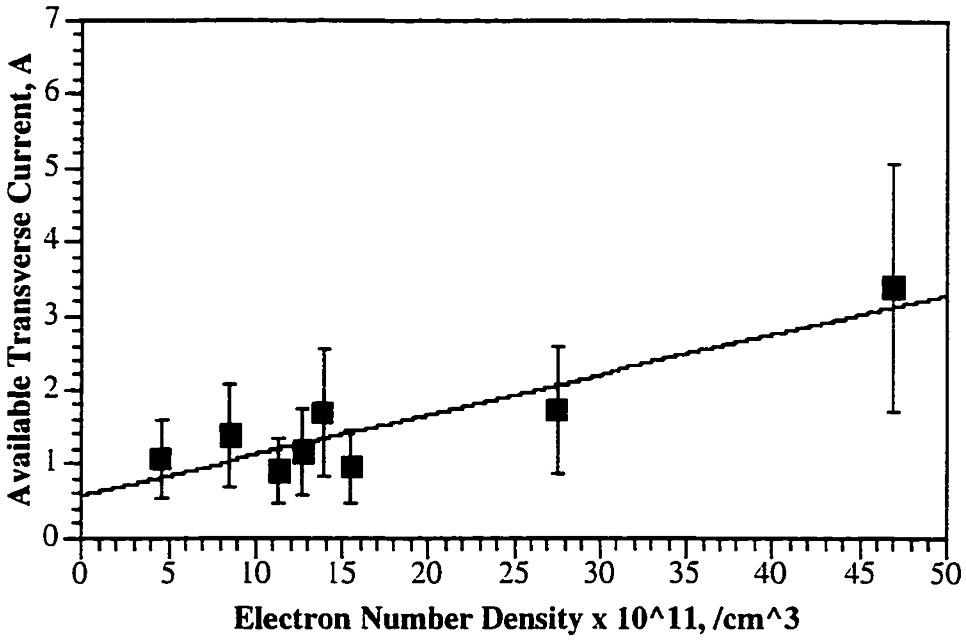

Figure 3.2 Variation in Available Current as a Function of Electron Number Density.

It should be pointed out that the available current calculated by this relation is actually smaller than the discharge current. This under-estimation is most likely attributed to the deviation in the true transverse diffusion coefficient from the classical behavior (see Equation 3.2) used in the Sugawara relation. This linear scaling of available current with electron density is fortunate in that the determination of density is not dependent on the large number of parameters that are required to calculate available current in the presence of a magnetic field. It is interesting to note that the variations in the anode fall appear to be a response to changes in the transverse flux as reflected in the related changes in the electron number density (compare Figures 3.1 and 3.3). Indeed, for the portion of the plot where the anode fall is growing rapidly with increasing magnetic field, the electron number density is either slowly rising or slowly falling. The local minima in the electron number density corresponds to the local maxima in the anode fall voltage. Further increases in the transverse magnetic field results in a rather dramatic growth in electron number density, a trend that continues for increasing magnetic field. Under these conditions, the anode fall and discharge voltage are observed to saturate. These findings suggest that the changes in the local electron number density may be an indicator of expected anode fall voltage behavior as the transverse magnetic field is varied.

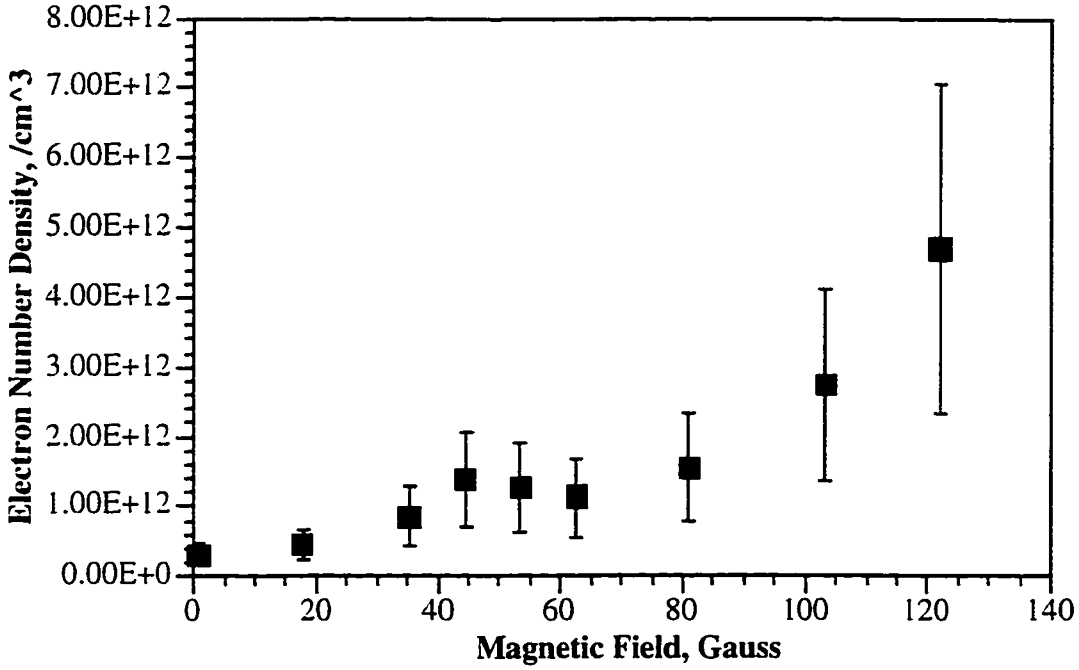

Figure 3.3. Variations in Electron Number Density with Transverse Magnetic Field.

The actual mechanism of how anode fall growth occurs is subject to debate. One possible mechanism for anode fall evolution with the transverse magnetic field may be obtained by again examining the transverse flux. For the operating conditions where the transverse field is very small, the available transverse flux is large compared to the discharge current. Under these conditions, all of the electron flux that enters the anode sheath is not needed and therefore is not collected. As a result, electron space-charge accumulates at and near the anode surface. This electron space-charge assumes a steady-state value as a consequence of the balance between entering charge and electron loss processes. The net result of the negative space-charge is primarily to reduce that potential of the anode relative to the sheath edge thus decreasing the anode fall to a lower value as the ratio of available current to discharge current increases. The magnitude of the steady-state anode surface charge or near-anode space-charge depends on the available flux which is in turn controlled by the transverse magnetic field. As the transverse magnetic field increases. the anode surface charge must decrease to a lower steady-state value if electron surface loss processes are constant. Decreases in this surface charge give rise to increases in the anode potential relative to the sheath edge which essentially corresponds to an increase in the anode fall voltage. Thus, when the measured electron number density is slowly varying or decreasing in magnitude, the problems associated with the reduction in transverse flux is enhanced because the transverse diffusion coefficient is dropping as is the case with an increasing transverse magnetic field and because local density growth is insufficient to offset the decrease in negative space-charge in the anode sheath. Under these conditions. the anode fall voltage can be expected to increase with increasing transverse magnetic field. These trends are experimentally observed as is illustrated in Figures 3.1 and 3.3. The measured jump in electron number density is associated with a jump in measured transverse flux and an increase in transverse flux gives rise to an increase in the uncollected negative space-charge density at the anode. This negative space-charge reduces the potential of the anode relative to the sheath edge so that the measured drop and subsequent saturation of the anode fall with increasing magnetic field under these conditions is in accordance with the proposed model mentioned earlier.

It is interesting to note that the work of Diamant et al. discusses experimental findings which allude to the importance of electron number density near the anode in a pulsed MPD thruster.[10] The Diamant et al. study asserts that at large anode falls, a transition into a spot mode attachment ensues which essentially functions to evaporate anode surface material. Ionization of this metal vapor is postulated to increase the number of charge carriers in the near anode-region and to ultimately prevent subsequent increases in the anode fall, thus leading to a saturation in anode sheath potential. In this respect, anode surface vaporization and subsequent ionization of the metal vapor controls the anode fall in the spot mode. This finding is consistent with observations in this study where variations in the anode fall voltage appear to occur with changes in the local electron number density. In this case, however, the effect of the magnetic field on ionization rate (see section 3.4.2) controls charge carrier production in the near-anode region as opposed to the vaporization processes discussed in the Diamant et al. study.

3.4.2. Electron Energetics and Ionization Phenomena

The measured electron temperature appears to decrease with increasing magnetic field. Although this measured decrease is fairly slight, see Figure 3.4, this behavior appears to suggest that the plasma is cooling as it diffuses across field lines on its journey to the anode. In order to reach the anode, the electrons must undergo a collisional "random walk" to the anode. Through each collision with a neutral or ion, there is an opportunity for the electron to liberate a fraction of its energy. Because the transverse drift distance between collisions of an electron in a magnetic field is on the order of a Larmor radius, the distance that an electron will travel between collisions decreases with increasing magnetic field; as a result, the rate at which electrons lose energy via collisions with slow ions and neutrals can be expected to increase as the transverse magnetic field increases. It is important to note that the trends in average electron energy as calculated from the measured EEDF as illustrated in Figure 3.5 does not appear to corroborate the Langmuir probe measurements. An effective electron temperature is obtained from the average energy resulting in an integration over all energies using the measured EEDF. EEDF measurements suggest that the electron temperature profile as a function of magnetic field is actually flat. This flatness suggests that for most conditions the energy obtained from the discharge electric field balances the energy lost due to inelastic collisions with neutrals and ions. Also, EEDF measurements suggest that the magnitude of the average energy is actually a factor of two larger than that measured using standard Langmuir probe theory.

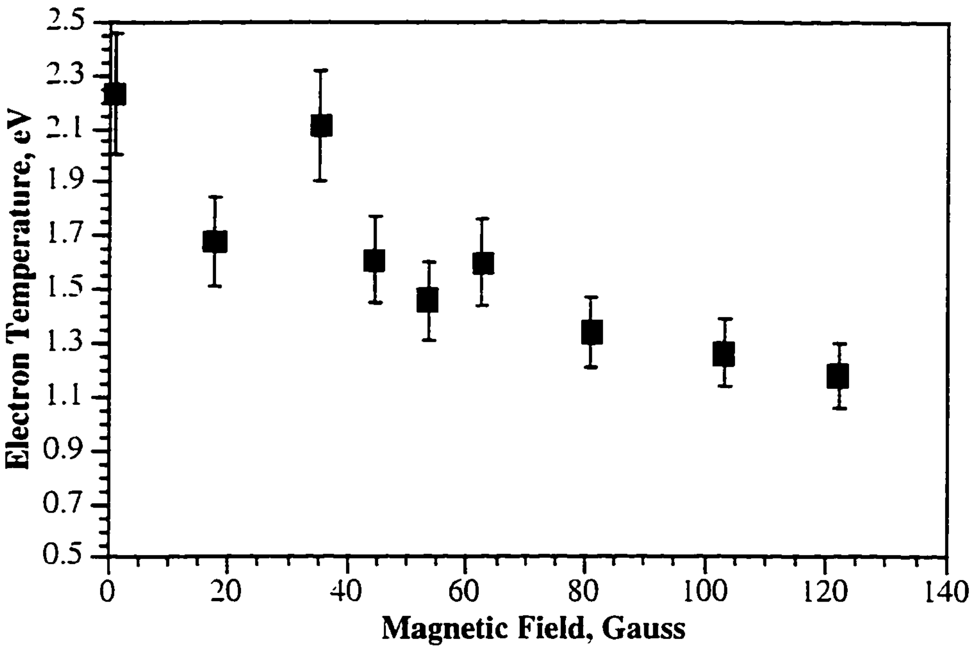

Figure 3.4 Variations in Electron Temperature with Transverse Magnetic Field.

These differences between the electron temperature behavior and magnitude may be related to the fact that the measured EEDFs are not Maxwellian (see Figure 3.6) as is assumed in single Langmuir probe theory, but instead Druyvesteyn-like (see Figure 3.7); here the energy exponential is two instead of one. Distributions of this nature are associated with significant fractions of the electron populations having their energies close to the average energy. Also, it should be pointed out that care must be taken in interpreting the fits here because deviations from experimental data at higher energies are significant.

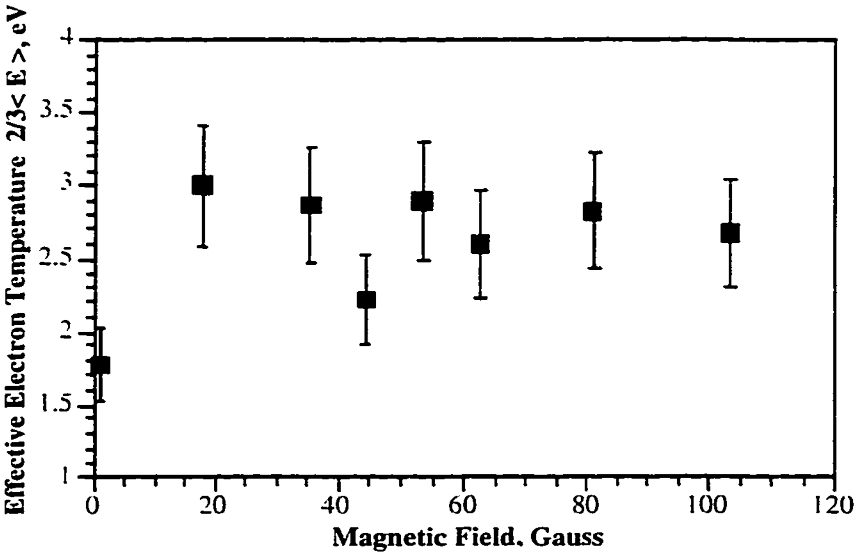

Figure 3.5. Variations in the Effective Electron Temperature with Transverse Magnetic Field.

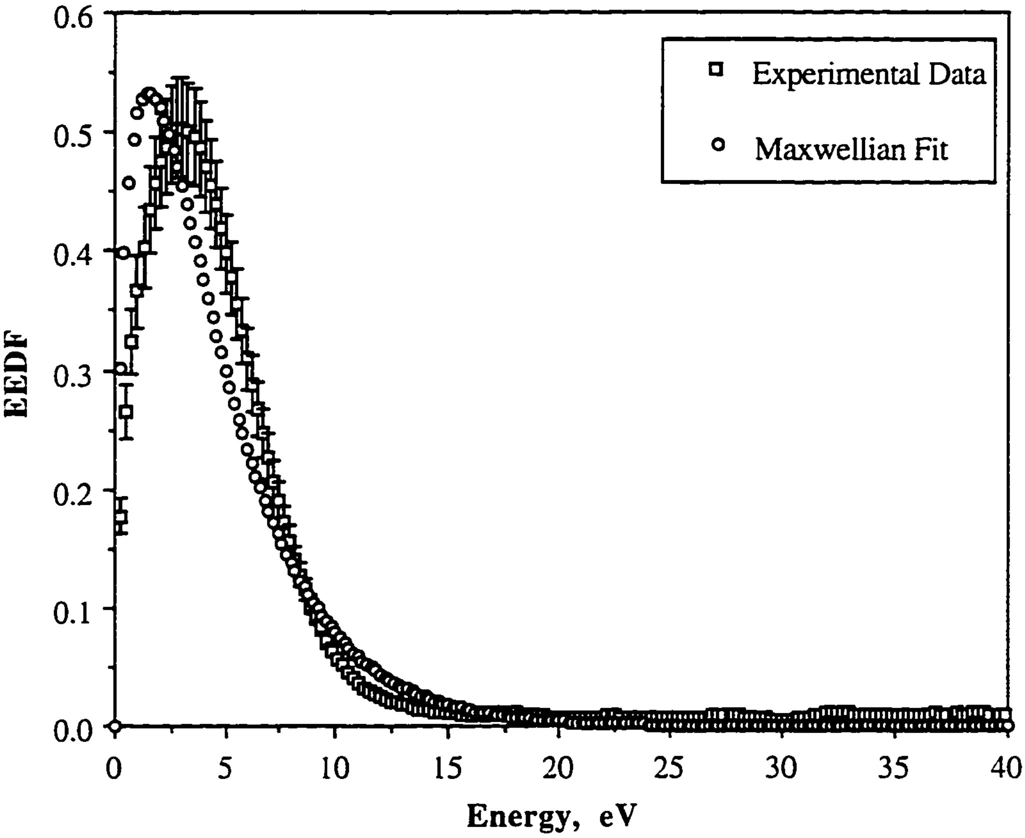

Figure 3.6. Non-Maxwellian Electron Energy Distribution Function.

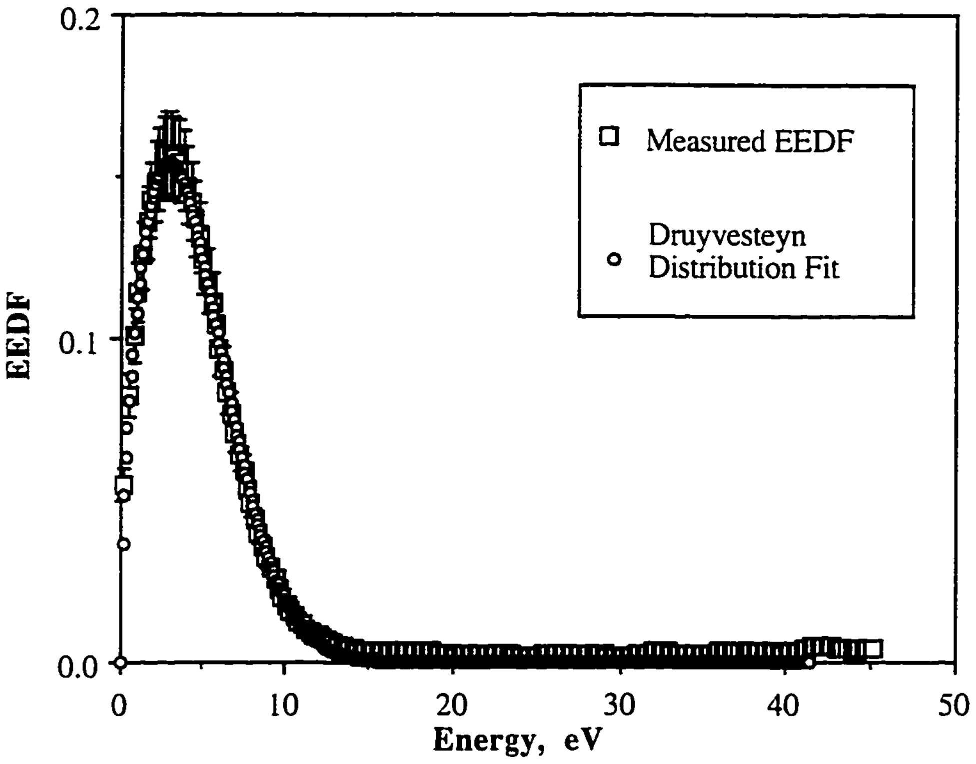

Figure 3.7. Druvesteyn-like Electron Energy Distribution Function.

Also observed was the expansion of the electron energy distribution function to higher energies as the magnetic field increases. This observation, displayed in Figure 3.8, suggests that an increasing amount of the discharge power is coupled into the plasma as the magnetic field becomes larger. This assertion appears to be supported by the anode heat flux measurements which indicate that the fraction of discharge power associated with anode losses decreases with increasing magnetic field strength, suggesting that as the magnetic field increases, an increasing fraction of the input power goes directly into the plasma as opposed to the anode.

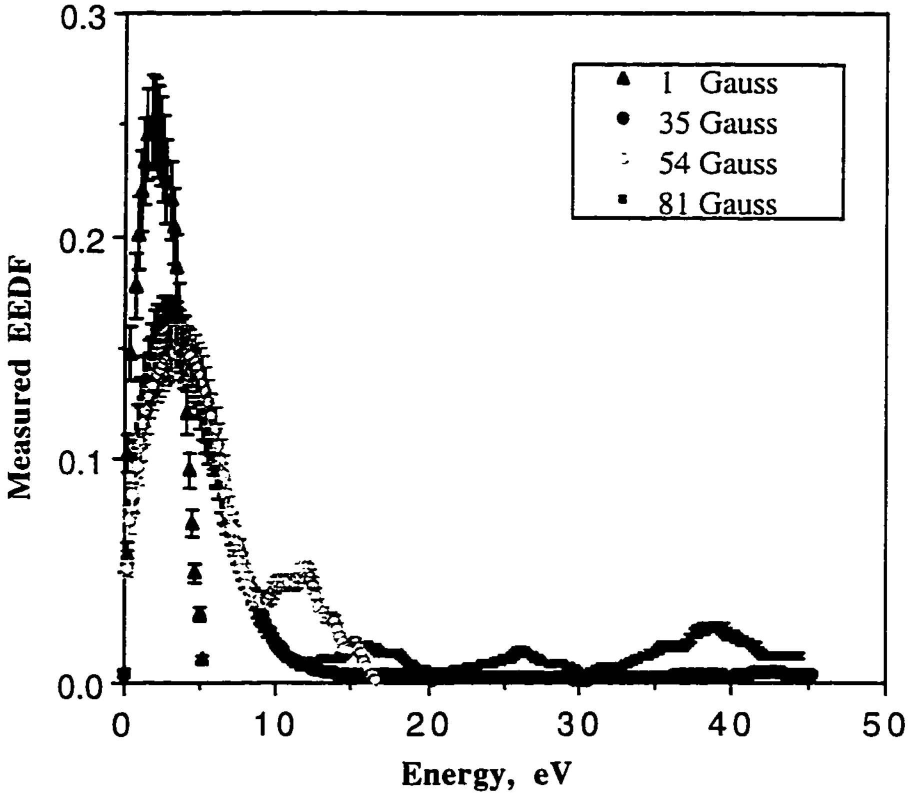

Figure 3.8. EEDF Variations with Transverse Magnetic Field Strength.

It should be pointed out that deviations from this Druyvesteyn-like form are seen in the tails of these electron energy distribution functions (see Figure 3.8). Peak structure observed to be present in the tails of the EEDFs may be remnants of an electron beam component associated with the cathode fall. This beam component may be necessary to sustain the ionization processes needed to maintain the discharge. The observed suppression of these components with increases in applied magnetic field strength appears to be a consequence of the magnetic field enhancing the coupling of the beam component to the gas. The observed increases in plasma density and the associated saturation of the anode fall voltage under such conditions may be a consequence of this coupling. The basis of this coupling appears to be related to increases in the electron residence time in the discharge with increasing transverse magnetic field strength. This increased residence time enhances the probability for an electron to have a thermalyzing collision with an electron from the cooler, bulk population or an inelastic collision with a neutral particle, thus smoothing out the bumps in the tail by transporting energy out of these higher energy regions. These observations allude somewhat to the notion that an electron beam component may be useful in reducing the growth of the anode fall due to its ability to enhance ionization rates.

The EEDF measurements are used in the calculation of ionization rates in the near-anode region as a function of transverse magnetic field. The ionization rate per electron was calculated at a given transverse magnetic field by using the low-energy electron ionization cross section data from Rapp and Golden-Englander[11] in the following relation:

$$K = n_{gas} \cdot \int_{E_T}^{\infty} \sigma(E) \cdot \sqrt{\frac{2E}{M}} \cdot f(E) \cdot dE. \tag{3.5}$$

Because the magnitude of the ionization frequency controls charge production, changes in this rate should be reflected in changes in the measured anode fall voltage. That is, it is to be expected that when the ionization frequency as a function of transverse magnetic field is decreasing, the rate at which the anode fall grows with magnetic field should increase. Figure 3.9 illustrates the response of the experimentally estimated ionization rate per electron to changes in transverse magnetic field strength in the near-anode region. It should be pointed out that the changes in the anode fall voltage as a function of transverse magnetic field roughly follow the observed trends in the near-anode ionization rates. It is also worth noting that the local minimum in the ionization rate approximately corresponds to the local maximum in the anode fall voltage (see Figure 3.1). Also, the ionization rate appears to flatten out at the higher magnetic field strengths even though the measured electron number density increases quite dramatically. This relative flatness of the ionization rate at the higher field strengths is due to the non-varying shape of the electron energy distribution functions in this range which translates into average energies and ionization path lengths that are also similar. What is not so similar between the operating points at higher magnetic field strengths, however, is the Hall parameter ($\frac{\omega_{ce}}{\nu}$). The Hall parameter is a measure of how many orbits an electron executes about its guiding center between collisions. The total distance the electron must travel, including the distance traveled along the gyro-orbits between collisions, is significantly different due to increases in the Hall parameter as the magnetic field increases. Indeed, increases in the effective path length due to the application of a transverse magnetic field has been exploited to enhance the ionization probability in hollow cathode discharges.[12] Therefore, if the ionization mean free paths are similar for the electrons at the 81 G data point and the 103 G data point, then the operating conditions in which the electron is forced to traverse a longer total distance to the anode due to gyro-rotation will generate, in general, more electrons than in the case of an

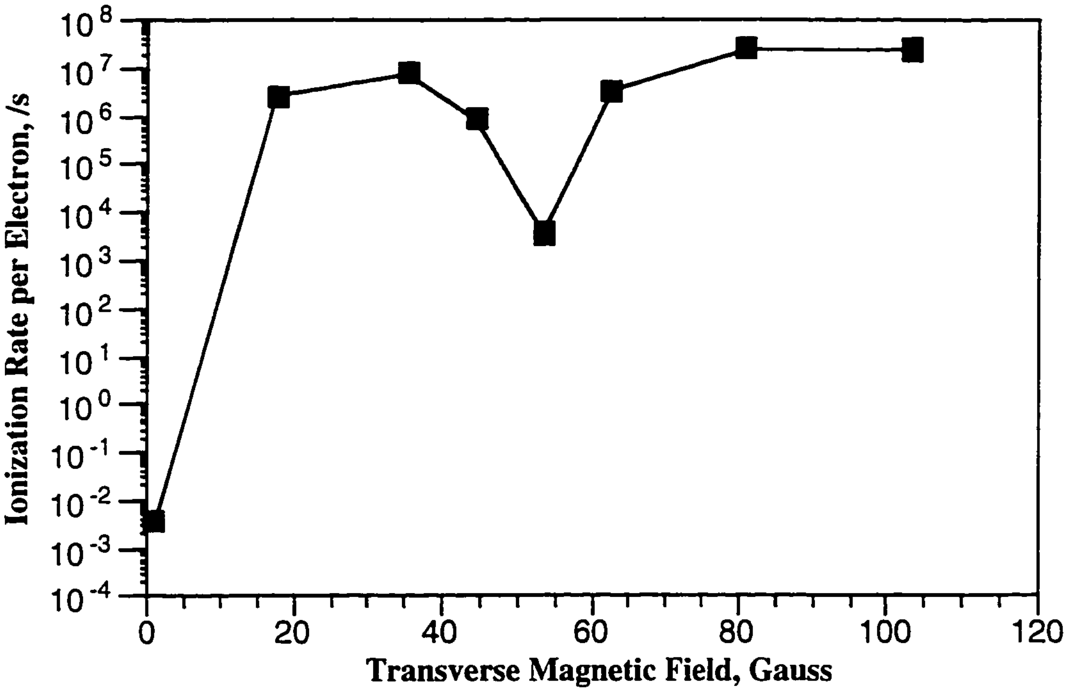

Figure 3.9. Variations in the Ionization Rate per Electron with Magnetic Field Strength.

electron traveling a shorter total distance to the anode. The measured increase in electron number density at the 103 G data point relative to the 81 G data point is then expected.

Variations in the intensity of two argon ion lines and one argon neutral line in a 0.2 mm thick imaged volume of plasma adjacent to the anode appear to be related to changes in the local electron number density. The spectral behavior is illustrated in Figure 3.10. The puzzling aspect of these data, however, is related to the observation that for a range of magnetic field strengths the behavior of the neutral line appears to be fairly flat while the ion line intensities vary significantly under the same conditions. The intensity of the argon ion lines correlate best with the measured changes in the near-anode electron number density. One explanation for the sensitivity of the argon ion lines to changes in discharge conditions as opposed to the apparent insensitivity of the neutral lines measured under the same conditions resides in the very nature of the neutral emission. In general, ion emission lines reflect the ion production rate because these newly formed ions can also be excited in the ionization process. In this respect, the ion lines provide density information convoluted with additional information on electron energetics. Argon neutral lines on the other hand are not expected to provide much information on electron densities or production rates because such lines reflect only the population of electrons with energies above the excitation threshold of that particular line. Also measured was the rate of growth of energetic electrons as a function of transverse magnetic field (see Figure 3.11). This measurement is accomplished by normalizing the measured spectral intensity to the electron number density. This quantity (see Equation 2.5) is proportional to the fraction of those electrons with energies above the excitation threshold for a specified transition. As mentioned earlier, the excitation threshold for the neutral line 470.2 nm is 14.5 eV while the excitation threshold for the ion line 480.6 nm is 35 eV. In general, with the exception of the initial jump for small transverse magnetic fields, the fraction of energetic electrons decreases with increasing magnetic field.

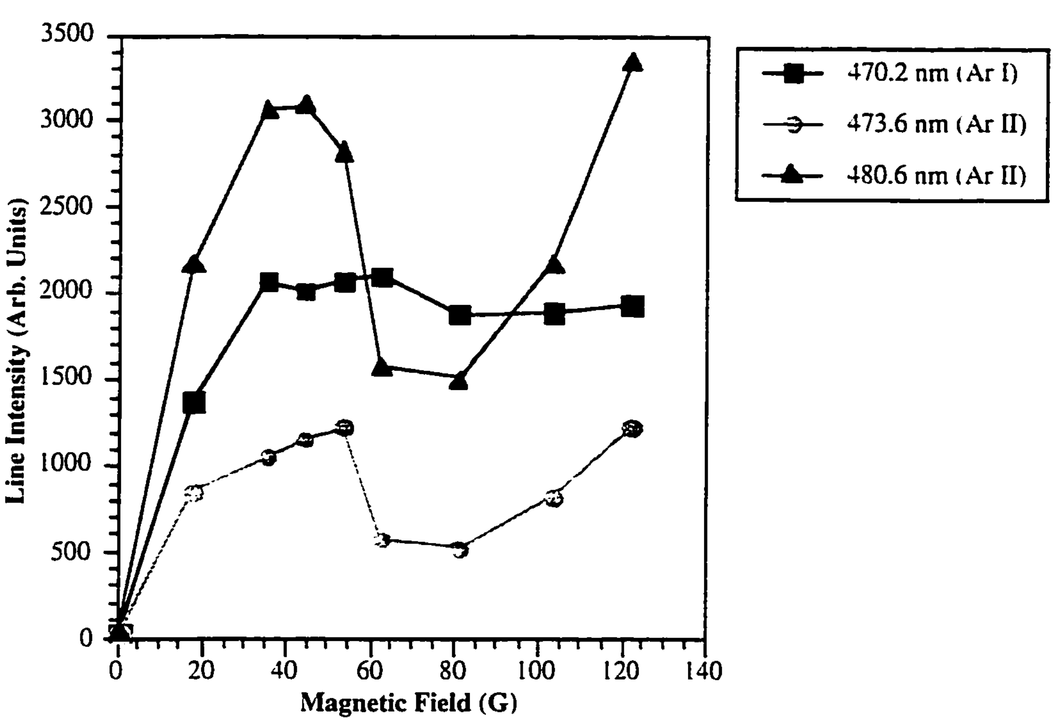

Figure 3.10. Variations of Line Intensity with Transverse Magnetic Field.

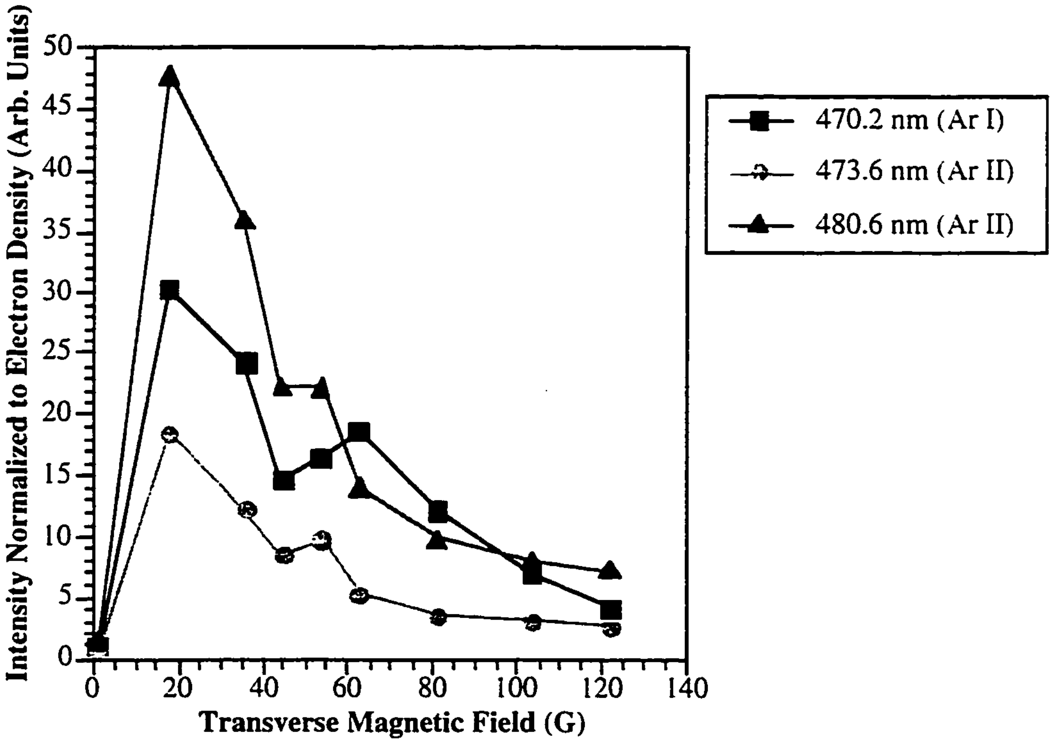

Figure 3.11. Variation in the Fast Electron Population with Transverse Magnetic Field.

However, as the magnetic field associated with the local maximum in the anode fall is approached from lower field strengths, there does appear to be growth in the electron population with energies above 14.5 eV. This assertion is based on the observation of local growth in the electron density normalized intensity of the argon 470.2 nm neutral line with increasing transverse magnetic field. EEDF measurements indicate additional structure in the higher energy region when the anode fall is at its maximum which is consistent with the observed spectra especially for those electrons with energies over 12 eV (see Figure 3.8). Beyond this critical magnetic field strength of 63 G (associated with the large anode fall), the rate at which the population of the high energy electrons decreases with increasing magnetic field is reduced somewhat.

3.4.3. Measured Anode Power Deposition

Measured anode power deposition determined via water calorimetry correlates well with variations in the energy balance model:[13,14]

$$P_A = I_d \cdot (\frac{5kT_e}{2e} + V_A + \phi_{wf}) + P_c + P_r \, . \tag{3.6}$$

Here the total power deposited into the anode, P_A, can be divided into an electronic term which consists of the discharge current, I_d, multiplied by an electron thermal energy term which is proportional to T_e, an anode sheath potential term, V_A, and a work function term, Φ_{wf}. Also included in the equation is P_c, which accounts for convection, and P_r, which accounts for radiation from the plasma and the glowing cathode. This model has been shown to represent the power flux into the anode of MPD thrusters quite well.[14] The deviation between the measured anode power flux and the expected heat flux as calculated using the energy balance relation was found to be on the average roughly 20% (see Figure 3.12). The overestimation of the predicted anode flux may be due to the uncertainty in the work function. The work function of iron was used in the equation for the stainless steel. Given the variations in the work functions of the components that make up the stainless steel alloy, the error contribution associated with using the work function of the stainless steel should not exceed 3%.[15] Another source of error could be due to thermocouple inaccuracies in which temperature measurements could be off by as much as 0.6 °C. This error in temperature contributes a power flux measurement error of roughly 20%.

The anode fall contribution, $I_d \cdot V_A$, in which V_A is the anode fall voltage as measured by the Langmuir probe, was always on the order of 80% of the measured anode power flux, thus dominating anode power deposition. The fact that this term appears to dominate is best illustrated in Figure 3.13. Here the trends in measured anode heat flux are seen to correlate quite well with variations in the product $I_d \cdot V_A$.

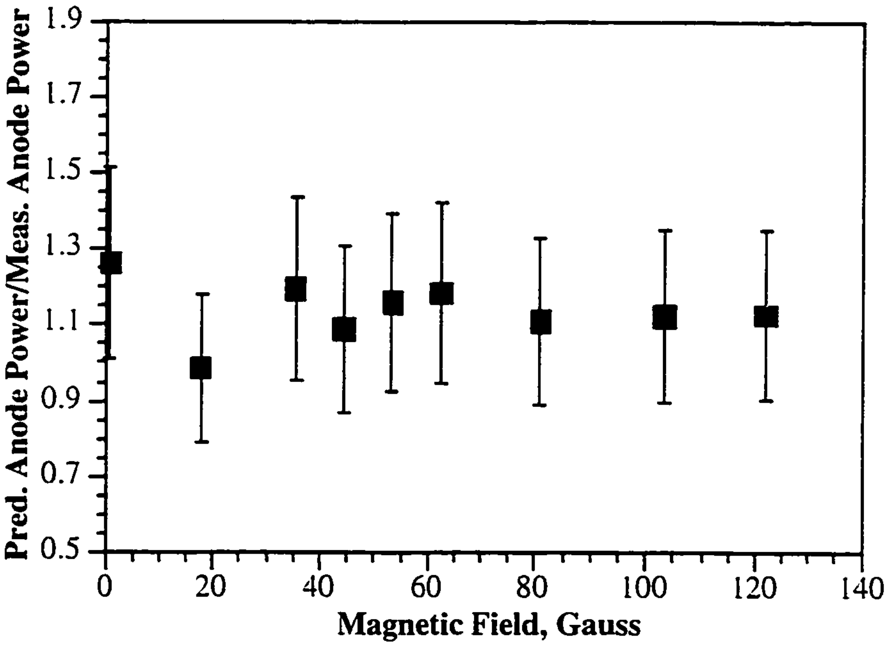

Figure 3.12. Comparison Between Predicted and Measured Anode Power Deposition.

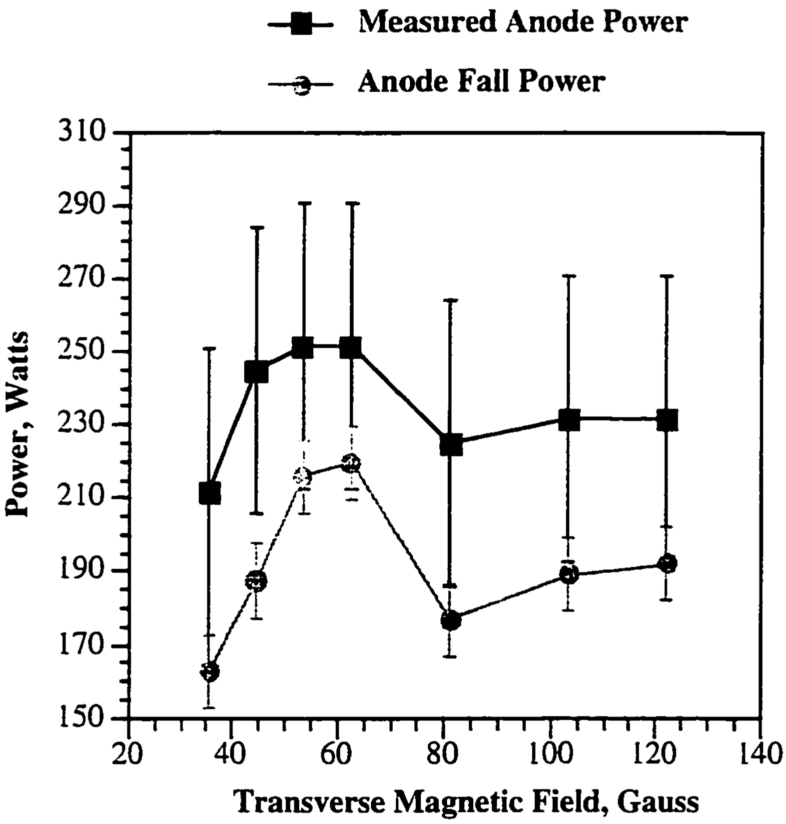

Figure 3.13. Comparison between Anode Fall Power and Total Anode Power Deposition.

The fraction of total discharge power that is associated with the anode heat flux decreases linearly with increasing magnetic field strength (see Figure 3.14). Again, this suggests that a larger fraction of the input power is being coupled into the plasma rather than the anode as the magnetic field is increased. It should be pointed out that similar behavior is observed in MPD thrusters.[2]

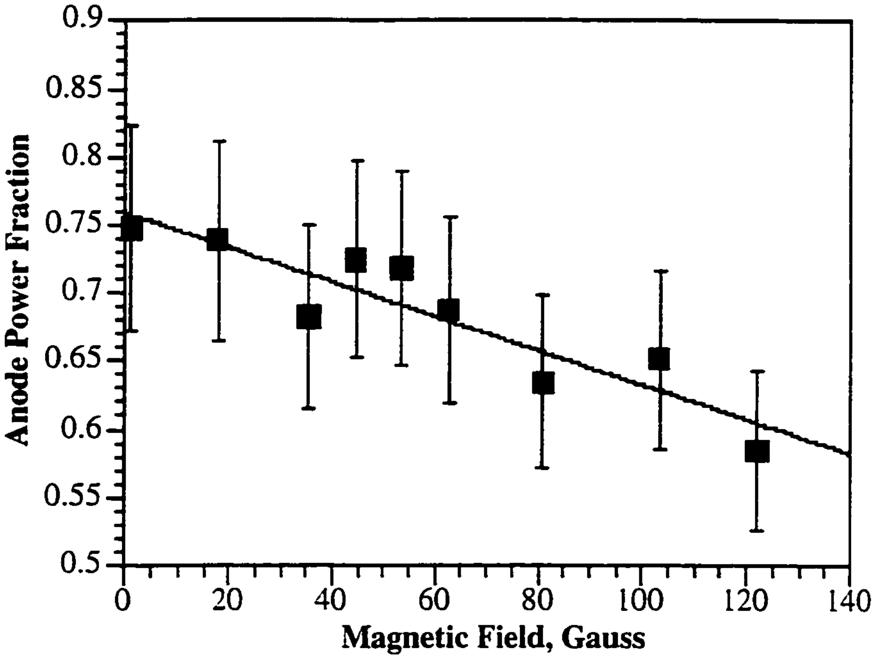

Figure 3.14. Variation in Anode Power Fraction with Transverse Magnetic Field.

3.5. Conclusions

The main purpose of this characterization study was to emphasize the proposed relationship between electron number density and anode fall voltage based on experimental observations and phenomenological arguments. The measured variations in the anode fall voltage appear to be related to changes in the electron number density. This assertion, based on supporting data, is readily explained. The electron density at the sheath edge is proportional to the transverse flux. It is this flux that ultimately determines the space charge distribution and the potential distribution in the anode sheath. This potential distribution defines the anode fall voltage. The measured variations in electron number density with transverse magnetic field can be attributed to changes in the ionization rate as the magnetic field is varied. It then follows that external modification to ionization processes in the near-anode region may be one means of controlling and ultimately reducing the anode fall voltage.

Notes to Chapter 3

[1] A.D. Gallimore, A. Kelly, and R. Jahn, AIAA Journal of Propulsion and Power, vol. 9, no. 3, 361 (1993).

[2] R. Myers, Proceedings of the 1991 AIAA Joint Propulsion Conference, AIAA-91-2342, (American Institute of Aeronautics and Astrounautics Press, Washington D.C., 1991).

[3] W. Schall, Proceedings of the AIAA 9th Electric Propulsion Conference, AIAA-72-502, (American Institute of Aeronautics and Astrounautics Press, Washington D.C., 1972).

[4] H. Tahara et al., Proceedings of the AIAA 21st International Electric Propulsion Conference, AIAA 90-2554, (American Institute of Aeronautics and Astrounautics Press, Washington D.C., 1990).

[5] A.D. Gallimore, R. Myers, A. Kelly, and R. Jahn, AIAA Journal of Propulsion and Power, vol. 10, no. 2, 262 (1994).

[6] J.T. Scheuer et al., Proceedings of the AIAA 23rd International Electric Propulsion Conference, IEPC-93-118, (The Electric Rocket Society Press, Columbus, OH, 1993).

[7] H. Hugel, IEEE Transactions on Plasma Science, Vol. PS-8, No. 8, 437, December (1980).

[8] F. Chen, Introduction to Plasma Physics and Controlled Fusion (Plenum Press, New York, 1984), Chapter 5, Sec. 5.10, pp. 190-195.

[9] M. Sugawara, The Physics of Fluids, vol. 9, no. 4, 797, April (1966).

[10] K.D. Diamant, E.Y. Choueiri, and R.G. Jahn, Proceedings of the 25th International Electric Propulsion Conference, IEPC-95-234, (The Electric Rocket Society Press, Columbus, OH, 1995).

[11] D. Rapp and P. Englander-Golden, J. Chem. Phys. 43, 1464 (1965).

[12] H. Kerkow, D. Boubetra and K. Holldack, Nucl. Instrum. Methods Phys. Res. B68, 41 (1992).

[13] J. Cobine and E. Burger, J. Appl. Phys. 26, 895 (1955).

[14] K. Shih and E. Pfender, AIAA Journal, vol. 8, 211 (1970).

[15] D.R. Lide, Editor in Chief, CRC Handbook of Chemistry and Physics (CRC Press, Ann Arbor, 1994), 12-113.

CHAPTER 4

THE EFFECT OF AN AXIAL MAGNETIC FIELD ON NEAR-ANODE PROCESSES

4.1. Introduction

Studies in the past have suggested that the anode fall voltage depends on the angle between the magnetic field vector and the anode surface normal.[1,2,3,4] In these studies as illustrated in Figure 4.1, the magnetic field direction vector is varied relative to the anode normal. As the angle Ψ is reduced, a decrease in the anode fall voltage is observed. The Soulas and Myers study[2] utilized an electromagnet that could be rotated relative to the anode surface normal so that the angle Ψ could be varied (See Figure 4.2). At small, Ψ, they observed reductions in the anode fall voltage and in the deposited anode power. Studies performed by Schall and later by Scheur et al. have suggested that the decrease in Ψ gives rise to conditions where the magnetic field can short out the anode sheath by directly connecting plasma electrons to the anode by way of flux tubes.

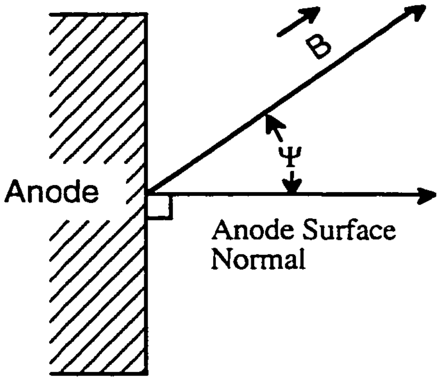

Figure 4.1. Schematic of Plasma-Anode Region in an Oblique Magnetic Field.

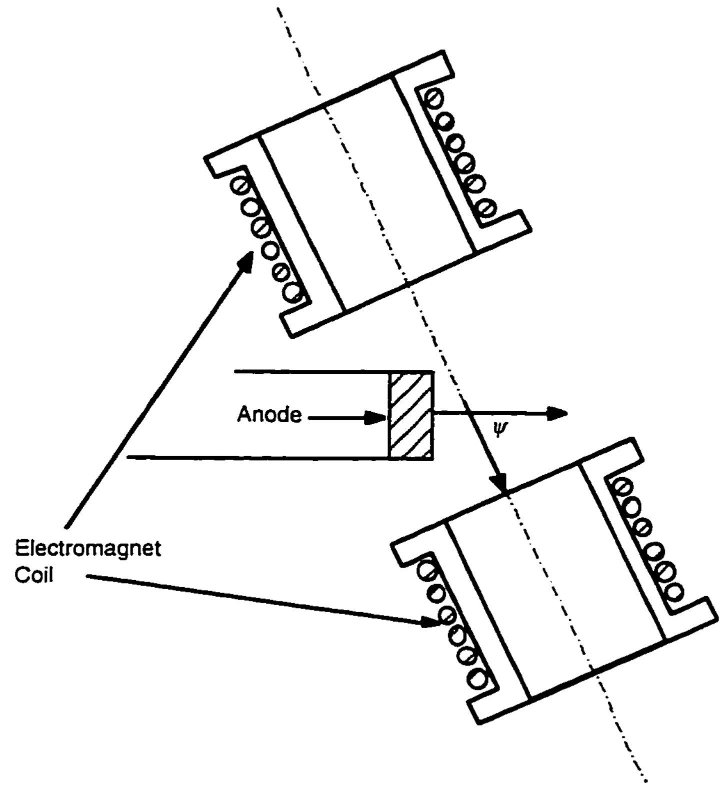

Figure 4.2. Soulas and Myers Experimental Set-up.[2]

One concern in regards to such studies is that of determining what varying the field geometries does to overall discharge processes. One major point that is emphasized in this thesis is that the ratio of the available transverse current to the discharge current controls the evolution of the anode fall voltage. This is due in part to the space charge distribution in the anode sheath which is ultimately determined by this ratio. In this respect, it is the magnitude of the transverse component of the magnetic field that should dictate how the anode fall voltage evolves. With this in mind, the findings in the Soulas and Myers study are readily interpreted. In this study it was found that as the angle Ψ decreased from 90 degrees, the anode fall voltage also decreased. This effect was attributed to an increase in electrical conductivity and transverse electron diffusion.[2] Another explanation for the reduction in the anode fall voltage as Ψ is reduced is related to the fact that as Ψ decreases, the transverse magnetic field component, $|B| \cdot \sin(\Psi)$, also decreases. Because this component controls the magnitude of available transverse current, it is no surprise that the anode fall voltage decreases as this angle is reduced. Because the angle is varied at a fixed magnetic field strength, the effect is akin to reducing the transverse component: as a result, the transverse current increases and the anode fall voltage decreases as reported and as expected.

Schall[1] and later Scheuer et al.[3] also investigated the effect of magnetic field angle and divergence on the anode fall voltage. The work of Schall entailed the use of two electromagnet coils which were used to generate an applied field whose divergence could be varied. In this study, the effect of increasing the divergence of an applied magnetic field on the anode fall voltage was determined. Here it was shown that the anode fall voltage was smallest when the magnetic field is most divergent. In this study, however, there was no comparison between cases which included the varying magnetic geometries and the case where the applied magnetic field is zero. Instead, comparisons are made among varying non-zero field orientations relative to the anode surface. The variations in the anode fall with magnetic field divergence appears to be consistent with the notion that the anode fall voltage depends on the transverse magnetic field component only because it is this component that decreases with increasing divergence.[1]

In a more recent study, Scheur et al.[3] used two sets of electromagnets to generate a diverging magnetic "nozzle" geometry in a coaxial plasma thruster. To generate this field, an electromagnet was placed in the cathode of the thruster while the other electromagnet was placed coaxial with the anode but outside of the anode collection surface. With this arrangement, the field lines generated by the electromagnets in the bulk plasma have substantial radial components so that the plasma electrons are magnetically "connected" to the anode. In this investigation, the anode fall was shown to decrease with increasing intensity of the applied nozzle field, $B_{r,z}$.[3,4] One concern with regards to investigations of this nature is that of separating other effects which can also give rise to reductions in the anode fall from that of anode sheath "shorting" due to magnetic focusing phenomena.

Because one coil is located in the cathode itself, the discharge cathode assumes a geometry similar to that of a hollow cathode with an axial magnetic field. It is well known that such arrangements enhance ionization in the cathode region.[5] Such enhanced ionization is a function of applied field. Enhanced ionization increases the available current which is in general proportional to the electron number density. It is more likely then that anode fall reductions are a consequence of increases in the available current rather than being attributed to "sheath shorting."

In the studies mentioned, varying the angle of the magnetic field with respect to the anode surface normal is utilized to achieve the desired effect: anode fall reduction. In two of these studies, the angle that the magnetic field makes with the anode normal is varied at a fixed magnetic field strength so that the transverse component decreases as the angle increases. Again, in the Scheur et al. study, the anode fall reduction may in fact be due to enhanced ionization in the cathode region. These effects can profoundly influence the magnitude of the anode fall voltage. In order to cleanly investigate the effect of the magnetic field angle on the anode fall voltage, the magnetic field angle must be varied at a fixed transverse magnetic field strength. In addition, so as not to affect ionization processes at the cathode, the magnitude and the variation in the axial field at the cathode must be minimal as the axial field is changed locally at the anode. In order to achieve these ends, an axial field whose maximum intensity at the anode surface drops off rapidly with distance is utilized. Figure 4.3 shows the spatial variations of the axial magnetic field used in this study as a function of position at specified peak axial intensities at the anode surface. Here, the rapid reductions in the axial field strength as the cathode is approached is illustrated. The drop off in field intensity with distance is essentially exponential in nature.

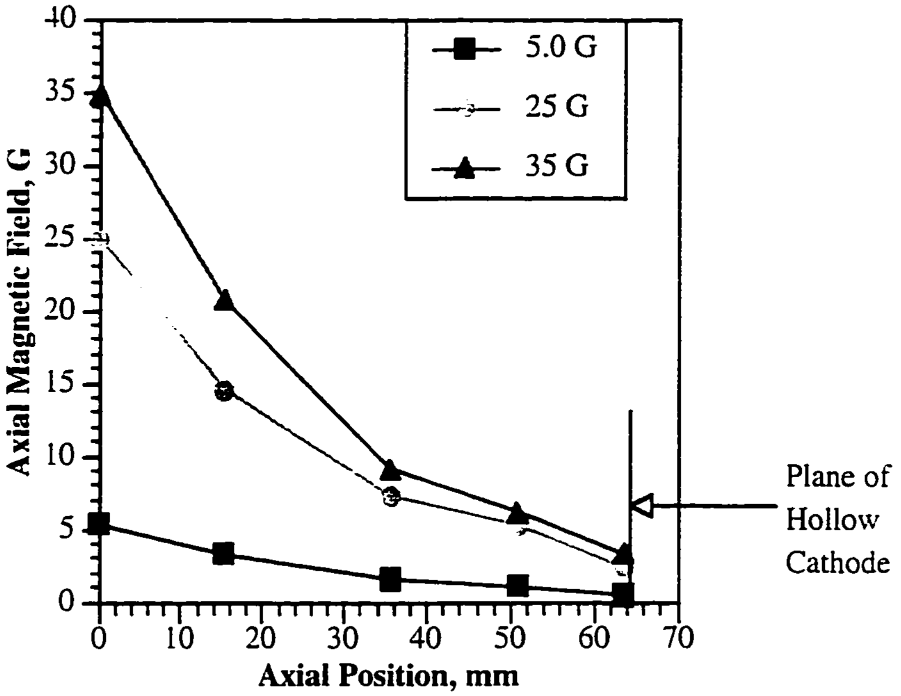

Figure 4.3. Axial Variation in Axial Magnetic Field.

4.2. Theory

One key question that this study is attempting to answer is what effect does the axial magnetic field have on near-anode processes? In particular, how do these processes change with the magnetic field angle relative to the anode surface normal? In general, the magnetic angle can be varied at fixed transverse magnetic field if the axial component is allowed to vary. Because the transverse magnetic field is fixed, the experimental conditions are somewhat analogous to those in applied field MPD thrusters where the transverse self-field and the applied axial field are always present. As asserted by past investigators[1,3] the magnetic field can short the anode sheath by directly guiding electrons from the cathode to the anode. In general, an electron tends to gyrate about field lines due to the v x **B** forces. Electron diffusion along the magnetic field is similar to the unmagnetized case in that the diffusion coefficient is $D = \frac{kT_e}{m\nu}$. Addition of a transverse magnetic field component reduces this diffusion rate. Consider the case of an electron with a directed velocity primarily along a purely axial magnetic field. As the transverse component is allowed to increase from zero, the fraction of this directed velocity along the axial direction decreases and thus the purely axial component of the electron flux decreases. Physically, this is the reason why the transverse magnetic field reduces the available axial current. With this in mind, discharge processes should be more sensitive to changes in the transverse component of the magnetic field than the axial component. Indeed, the magnitude of the available current parallel to the anode surface normal depends primarily on the transverse component of the magnetic field. The available current, as discussed in proceeding chapters, is described by the Sugawara relation:[6]

$$I_{e\perp} = \frac{1}{4} \cdot e n_o \bar{v}_e A \cdot [\frac{16}{3} \cdot \frac{\lambda_e \alpha^{\frac{1}{2}}}{K(k) \cdot r_o}] \cdot \frac{1}{1 + \frac{16}{3} \cdot \frac{\lambda_e \alpha^{\frac{1}{2}}}{K(k) \cdot r_o}}. \tag{4.1}$$

Here α is the ratio of the transverse diffusion coefficient to the unmagnetized diffusion coefficient and is thus a function of the transverse magnetic field.[6] In addition, because the axial magnetic field is pointed along the direction of the electric field in the sheath and pre-sheath regions, it cannot appreciably affect axial diffusion of electrons and ions into the anode sheath itself.[7] Hence, significant changes in electron transport properties along the discharge axis will accompany magnetic field angle changes only if the transverse field component is also varied or if the angle changes ionization phenomena in the process.

4.3. Experimental Considerations

This experiment utilizes the axial field coil shown in the experimental set-up section of this work (see Figure 2.1). The anode is located along the axis of the 7 cm diameter electromagnet spool. The field generated by the spool is confined to the near-anode region. The field decays rapidly over the length of the positive column (Figure 4.3). The field is not expected to influence cathode operation because the largest axial field generated at the anode in this study decayed to a near-cathode field of no more than 3 G. In addition, the axial field generated at the exit plane of the hollow cathode was fairly insensitive to variations in the axial magnetic field at the anode's surface. At such small field strengths, the electron Larmor radius is orders of magnitude ($\sim 10^4$ times) larger than the cathode sheath thickness. Thus, this field is not expected to appreciably affect near-cathode ionization processes.

4.4. Results and Discussion

The applied axial magnetic field imposed on a 8.25 A low-pressure arc discharge (50 mTorr) was varied between 0 and 35 G at three different transverse magnetic field strengths: 1 G, 26.5 G, and 53.5 G. As the axial magnetic field is varied, the magnetic field angle relative to the anode surface normal varies as $\Psi = \arctan\left[{}^{B_\perp}\!/_{B_\parallel}\right]$ (see Figure 4.1). Here $B_\perp$ is the transverse field component while $B_\parallel$ is the axial field component. In each case, Langmuir probe, emission spectroscopy, and anode power deposition data were obtained. The Langmuir probe was located 2.5 mm above the anode surface.

Application of an axial magnetic field to a low-pressure arc has the effect of reducing radial diffusion thus enhancing electron confinement. In general, a measure of radial electron confinement due to the presence of the axial field component is the ratio of the electron Larmor radius to the discharge radius, r_l/r_d. For this investigation, the discharge radius is approximated as the radius of the anode: 12.7 mm. This estimate yields a lower limit to the active discharge radius. A plot of this quantity, r_l/r_d, as a function of the axial field strength with the transverse field fixed at 1 G is illustrated in Figure 4.4. Axial confinement is illustrated as the electron's radial mean free path decreases to Larmor radii smaller than the radial dimensions of the discharge column. An analysis of the plasma's response to such confining effects and possibly other processes associated with the application of the axial field are elaborated upon in the following sections.

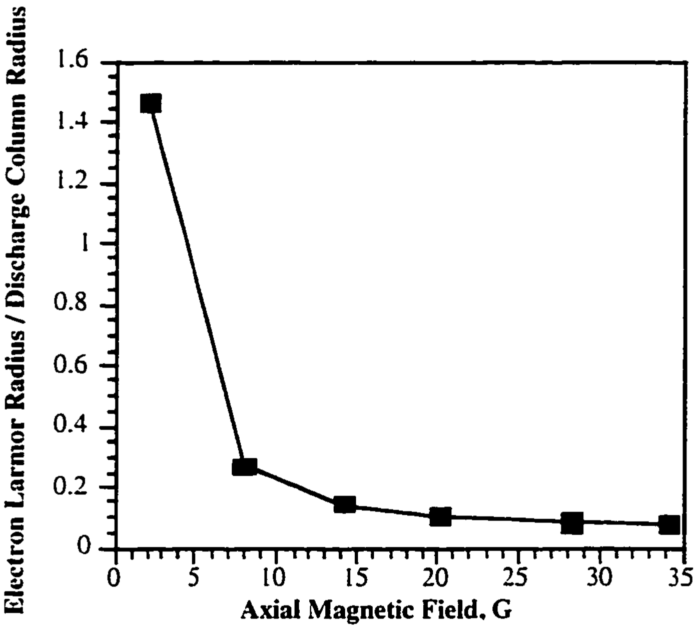

Figure 4.4. Variations in r_l/r_d with Axial Magnetic Field.

4.4.1. Case 1: Transverse Magnetic Field = 1 G

The anode fall and the normalized available transverse current are shown in Figure 4.5. The transverse available current as calculated from Equation 4.1 is normalized to the available current corresponding to a fixed transverse magnetic field and the lowest axial field strength investigated. As illustrated in Figure 4.5 the anode fall voltage did not change significantly under the 1 G transverse field operating condition as the axial field was varied. There was, however, a measured dip in the electron number density (see Figure 4.6) which gave rise to similar structure in the normalized available current. The measured variations in the anode fall voltage are consistent with observed changes in the available electron current. Because the transverse component of the magnetic field is so small at this operating point, the magnetic field angle does not vary appreciably with changes in axial magnetic field. For completeness, however, variations in the anode fall voltage with field angle is shown in Figure 4.7. In this case the anode fall for all practical purposes is fairly unresponsive to such small changes in the magnetic angle.

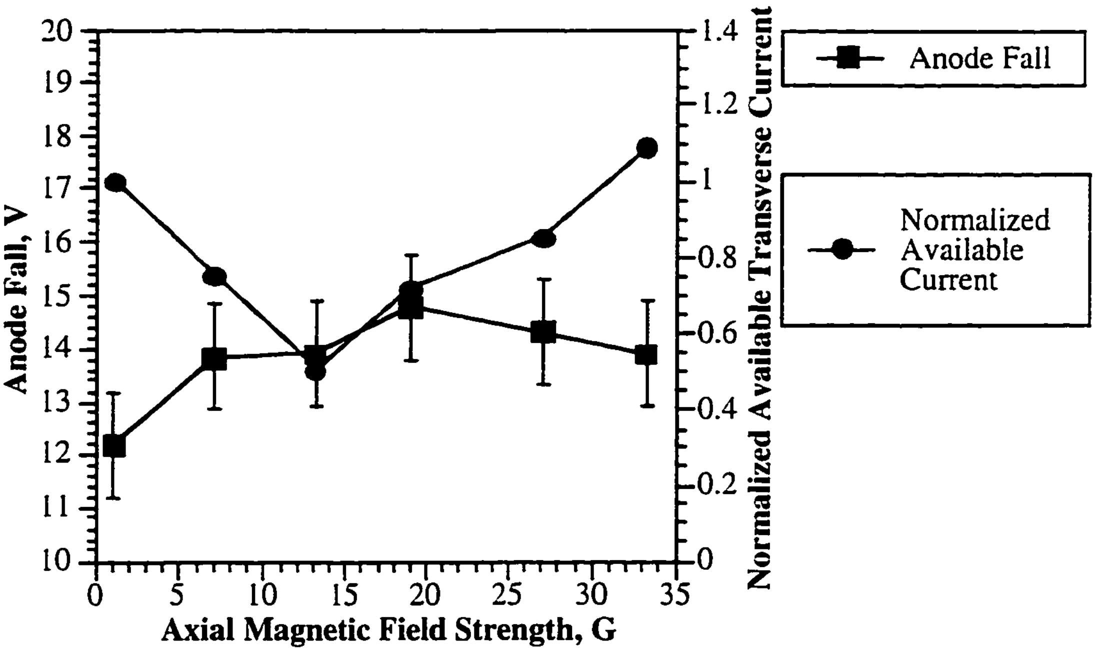

Figure 4.5. Anode Fall and Transverse Current Variations with Axial Magnetic Field: Transverse Magnetic Field=1 G.

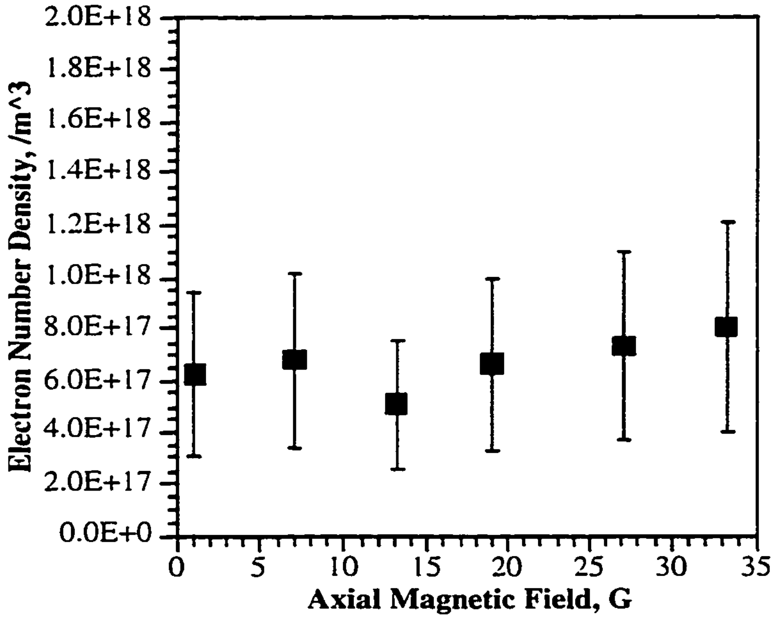

Figure 4.6. Electron Number Density Variations with Axial Magnetic Field: Transverse Magnetic Field=1 G.

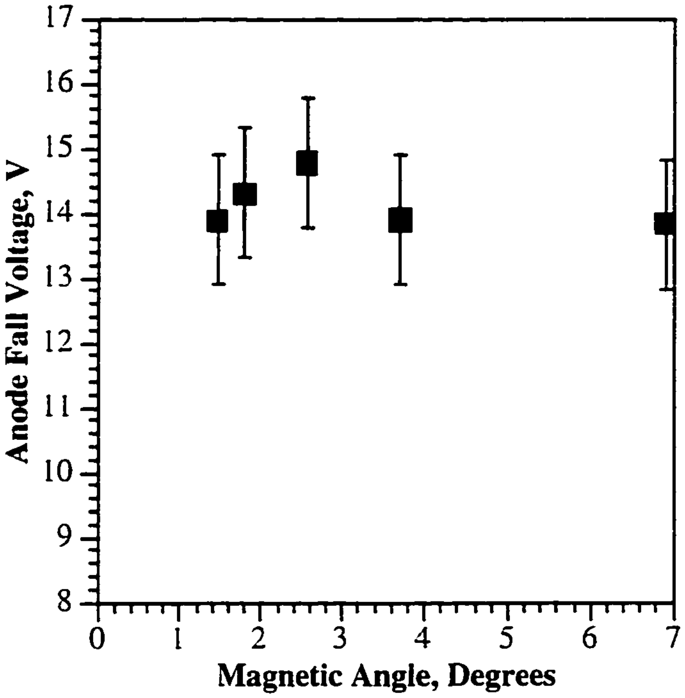

Figure 4.7. Anode Fall Variations with Changes in Magnetic Field Angle Relative to the Anode Surface Normal: Transverse Magnetic Field=1 G.

In terms of changes in measured power deposited into the anode, the calorimetric measurements indicated that there was virtually no change in the anode power deposition as the axial magnetic field was varied at this operating point. This observation is consistent with the small recorded changes in the anode fall voltage and the discharge voltage.

The emission spectra obtained from the near-anode region is presented in Figure 4.8. Here, growth is observed in the spectral intensity of the argon 472.6 nm and 476.4 nm ion lines as the axial magnetic field is increased. This growth is consistent with the expected increased electron confinement as the axial field increases. Confinement enhances the coupling of the electrons to the discharge by restricting radial diffusion outward. In this respect, a given electron has a better opportunity to excite an ion before diffusing away radially. On the other hand, other than a slight rise in intensity between 0.0 G and 15 G, the argon neutral lines appear to be insensitive to the changes in the axial magnetic field strength. The observed insensitivity of the neutral lines relative to the variations observed in the ion lines is most likely related to the transition probabilities of these lines which are two orders of magnitude smaller than the ion lines used in this study.[8] In addition, neutral line intensity variations are not expected to reflect changes in ionization rates brought on by the confinement effects associated with the axial magnetic field. These lines are responsive to only those electrons with energies above a certain excitation threshold.

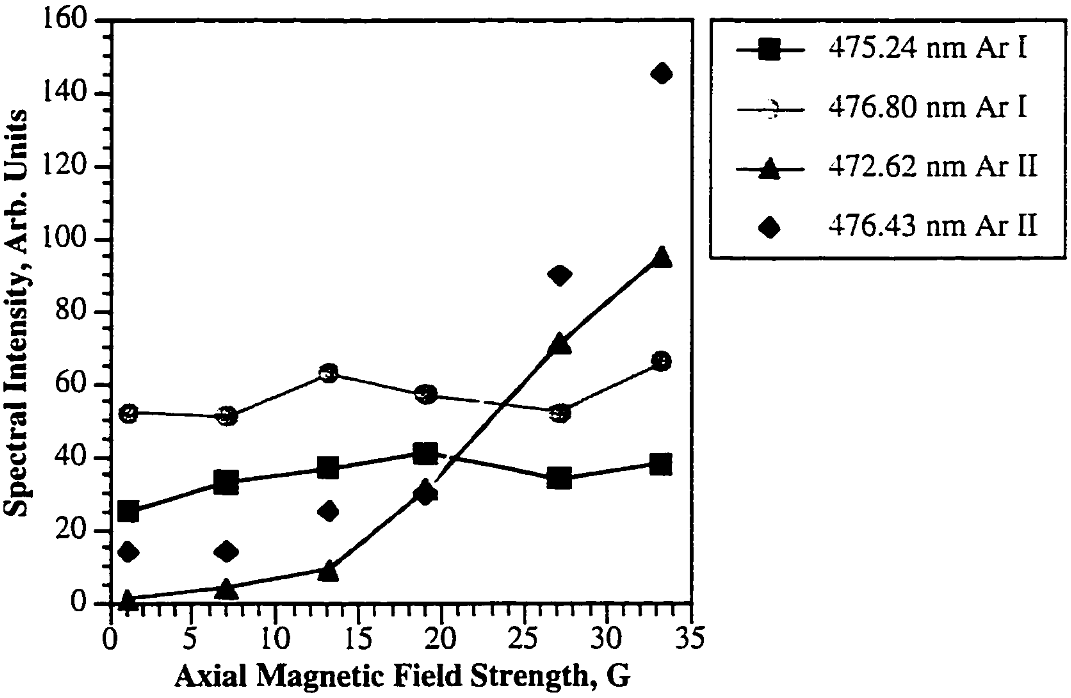

Figure 4.8. Argon Ion Intensity Variations with Transverse Axial Magnetic Field: Transverse Magnetic Field =1 G.

Figure 4.9 shows intensity normalized to the measured local electron number density. The behavior of this parameter yields information on the growth of the fraction of electrons with the ability to excite the argon neutral and ion transitions. The excitation threshold for argon neutrals exceeds 14 eV whereas the excitation threshold for the argon ion lines exceeds 35 eV.[9] The behavior of this parameter reflects changes in the population of energetic electrons in the discharge. The density normalized argon ion lines suggest that the fraction of energetic electrons becomes larger as the axial field is increased. As the axial field is increased, an increase in the overall discharge residence time of the more energetic electrons is expected to occur due to a reduction in radial diffusion rates. The increase and subsequent saturation in the magnitude of the density normalized neutral spectra suggests that the excitation rate of the neutral line is not a monatonically increasing function of the axial field at this operating condition. This behavior is quite puzzling in that it is expected that this parameter should follow the general trends of the density normalized ion lines. These trends in the density normalized neutral spectra are similar to that which is observed in the raw neutral spectra data though much more exaggerated. One explanation for this behavior may be related to possible neutral density variations in the near-anode region. The electron confinement due to the application of the axial field enhances the coupling of the electrons to the neutral gas. Such coupling can give rise to heating of the gas thus rarefying the neutral density locally and thus reducing the number of neutral emitters in the region. This postulate is consistent with the behavior of the observed spectra and the trends in the electron number density particularly in the region beyond 15 Gauss. This would also partially explain the apparent insensitivity of the neutral lines to increases in the axial field.

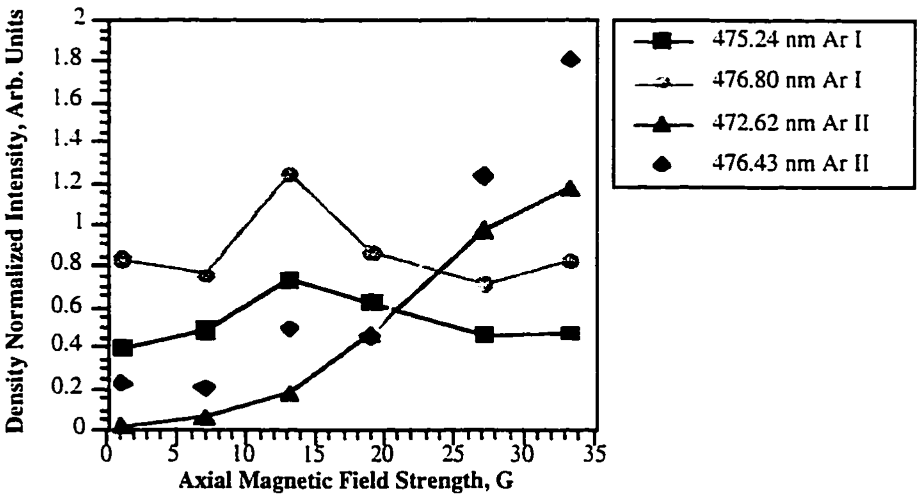

Figure 4.9. Normalized Intensity Variations of Argon Ion Spectra with Axial Magnetic Field Strength: Transverse Magnetic Field = 1 G.

4.4.2. Case 2: Transverse Magnetic Field = 26.5 G

As illustrated in Figure 4.10, the changes in the anode fall voltage and the calculated available transverse current (Equation 4.1) as the axial magnetic field was varied at the fixed transverse field of 26.5 G were small. It is worth noting though that the small changes that do occur in the anode fall voltage do appear to be consistent with changes in the transverse current and electron number density (Figure 4.11). Over the entire axial field range, the discharge voltage changed by only +1 V. The relative sensitivity of the discharge to changes in axial and transverse field is emphasized by the fact that the discharge voltage at zero axial magnetic field with a 1 G transverse field increased by 3 V when the transverse field changed from 1 G to 26.5 G. Figure 4.12 illustrates the behavior of the anode fall as a function of magnetic field angle, Ψ, relative to the anode surface normal. The anode fall voltage remains relatively flat for nearly transverse field geometries. As the angle decreases below 50 degrees, a rise in the anode fall voltage was observed. This rise in the anode fall at small angles is most likely attributed to the possible constriction of the anode attachment caused by the axial field component so that the actual collection area at the anode surface may be somewhat smaller. The anode fall voltage rise due to possible attachment constriction illustrated in Figure 4.13 is expected to be most noticeable at the larger transverse magnetic field strengths. Such behavior is attributed to the fact that the transverse flux decreases as the transverse magnetic field increases. In addition to these reductions in transverse flux, charge collection at the anode is further hampered by the reduction in anode collection surface area due to constriction. Constriction of the arc at the anode surface forced by the axial magnetic field may necessarily be accompanied by an increase in the anode fall voltage if the product of the attachment flux and the effective anode surface area is insufficient to sustain the discharge at a certain current.

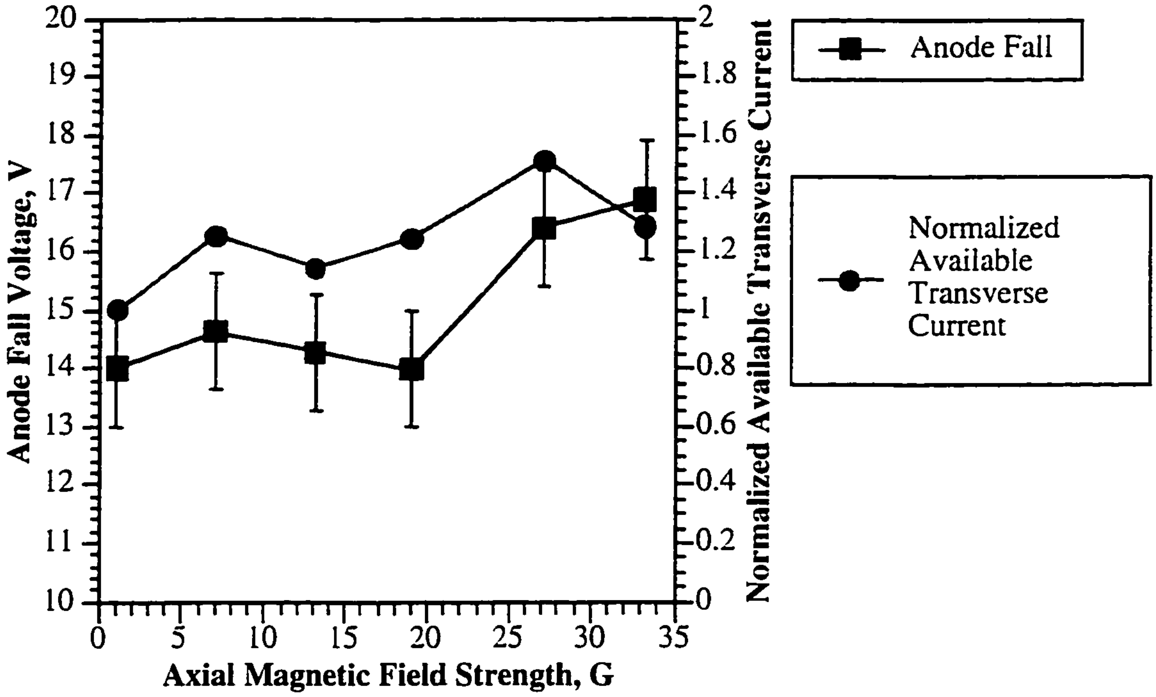

Figure 4.10. Variations in Anode Fall And Transverse Current with Axial Magnetic Field: Transverse Magnetic Field= 26.5 G.

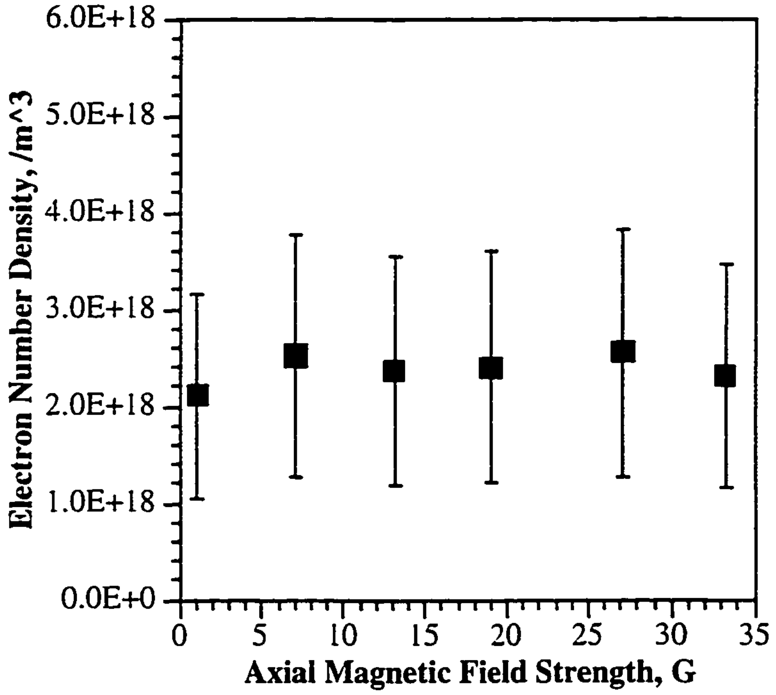

Figure 4.11. Variations in Electron Number Density with Axial Magnetic Field Strength: Transverse Magnetic Field= 26.5 G.

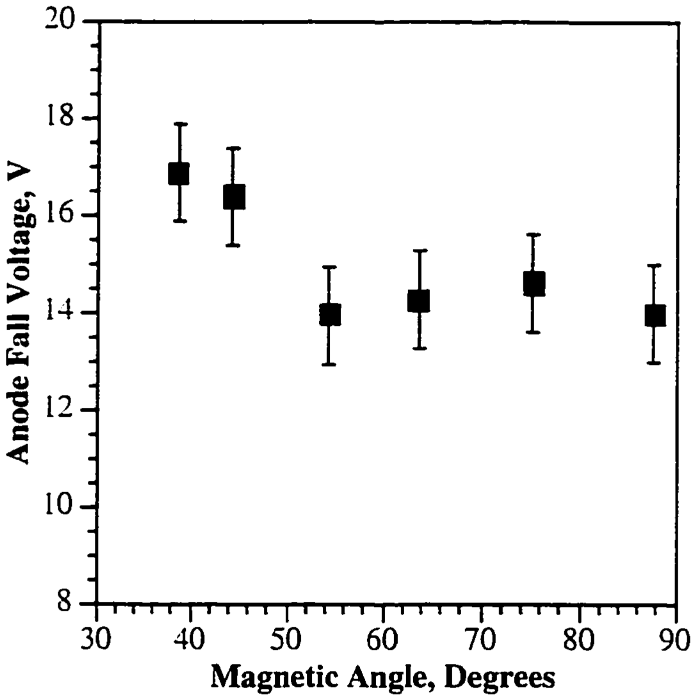

Figure 4.12. Variation in Anode Fall Voltage with Magnetic Field Angle Relative to Anode Surface Normal: Transverse Magnetic Field = 26.5 G.

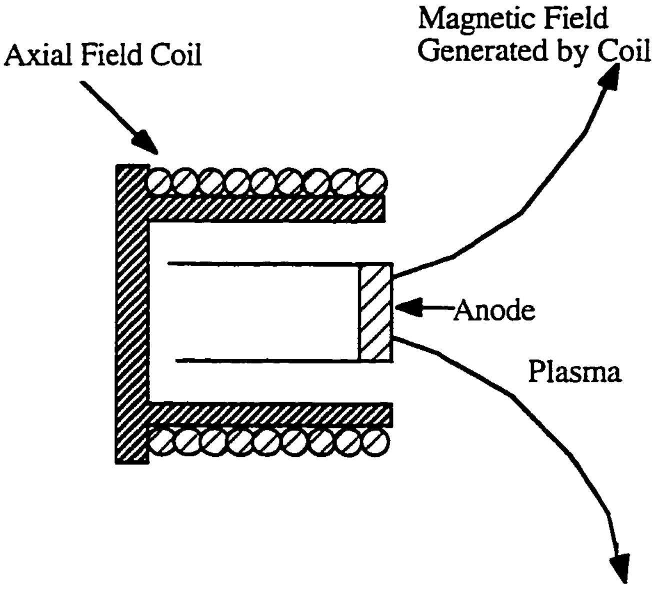

Figure 4.13. Constriction Effects due to an Axial Magnetic Field.

The power deposited into the anode was constant up until an axial field strength of ~35 G. Here, the power flux increases by roughly 20 W. This increase in power is almost entirely accounted for by the roughly 3 V rise in anode fall voltage (3 V* 8.25 A ≈25 W).

Raw emission spectra displayed in Figure 4.14 taken at this operating point suggest that both the intensity of argon neutral and ion lines on the average are fairly insensitive to changes in the axial magnetic field strength at this particular operating point. This insensitivity implies that at the transverse field strength of 26.5 G, excitation processes are not appreciably affected by variations in the axial magnetic field. Density normalized spectra illustrated in Figure 4.15 possess structure similar to the that of the raw spectra suggesting that the fraction of energetic electrons (> 14 eV) does not vary appreciably with axial magnetic field strength under these conditions.

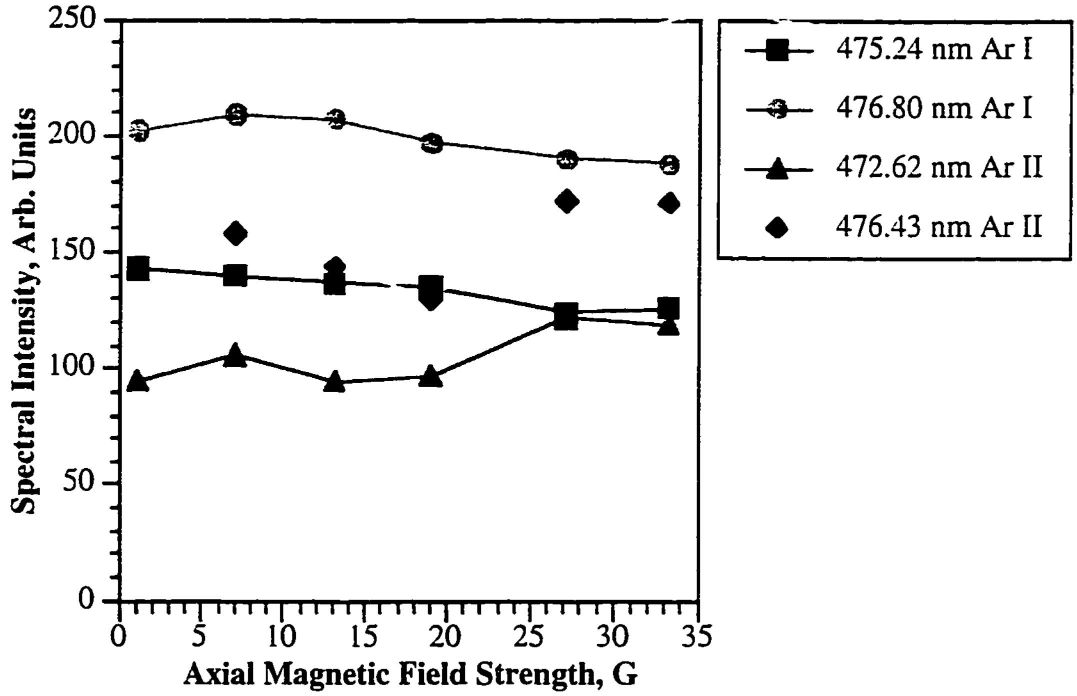

Figure 4.14. Spectral Intensity Variations as a Function of Axial Magnetic Field Strength: Transverse Magnetic Field=26.5 G.

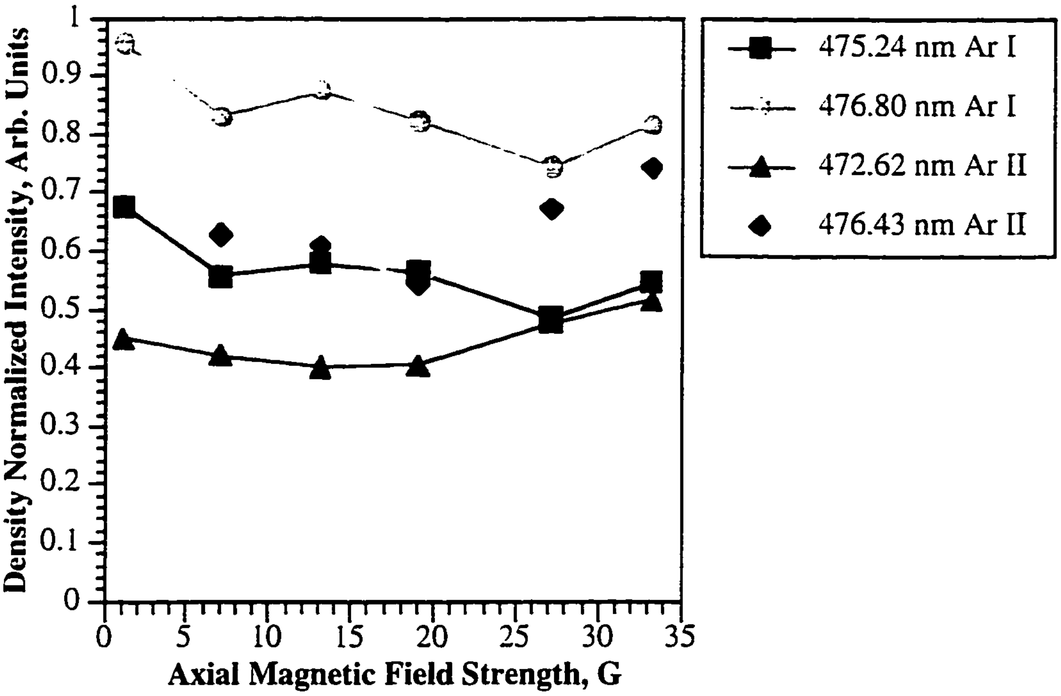

Figure 4.15. Variations in Density Normalized Intensity as a Function of Axial Magnetic Field: Transverse Magnetic Field=26.5 G.

4.4.3. Case 3: Transverse Magnetic Field = 53.5 G

As shown in Figure 4.16, the anode fall voltage increases slightly only to saturate as the axial field strength increases. The calculated available transverse current decreases in variation with the electron number density (see Figure 4.17) as the axial field strength increase. The response of the anode fall voltage to these changes appear to be consistent with expected behavior. Besides the initial slight rise in voltage, over the axial field range investigated, the variations in anode fall voltage with magnetic field angle is very small, with the anode fall voltage changing by only 1 V over the axial magnetic field range (see Figure 4.18). The discharge voltage decreases by roughly 1 V over this axial magnetic field range. The change in discharge voltage associated with the transition in transverse magnetic field strength from 26.5 G to 53.5 G is roughly 8 V. At this higher transverse field, the electron number density and anode fall voltage are also larger. Current constriction effects at this operating point are minimized due to a larger local electron number density and the tendency of the transverse field to stretch out the attachment over the surface of the anode. This behavior is expected when the transverse field is much larger than the axial field. In addition, this coupled with confinement effects, which in general should enhance charge production near the anode surface, may also play a role in the slight reduction in the anode fall.

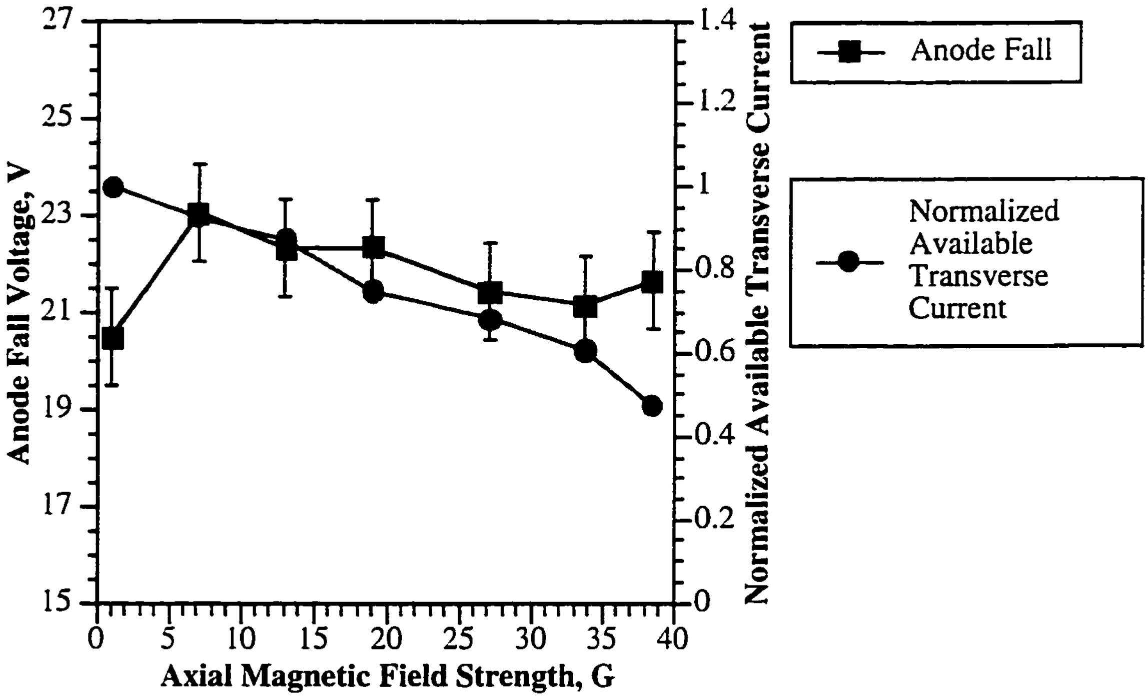

Figure 4.16. Variation in Anode Fall and Normalized Transverse Current with Axial Magnetic Field Strength: Transverse Field=53.5 G.

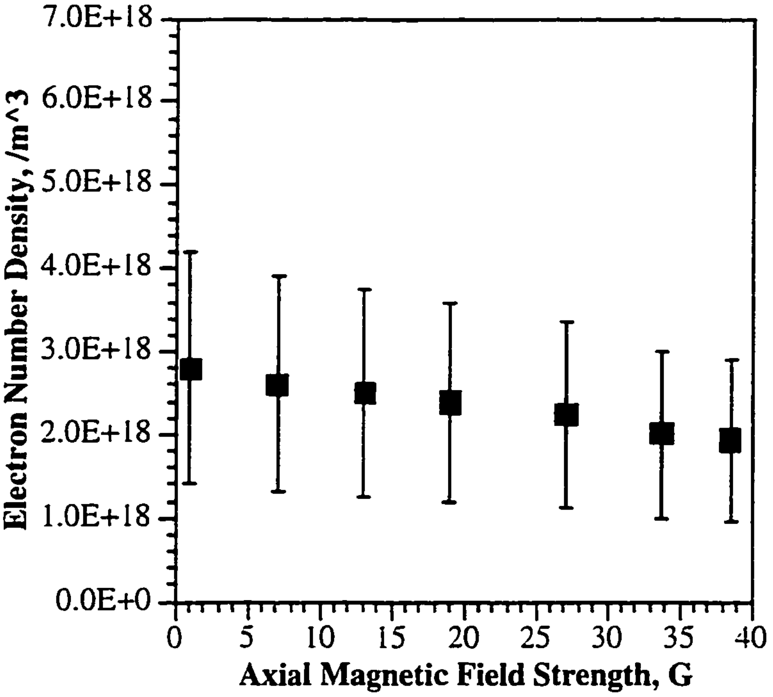

Figure 4.17. Variation in Electron Number Density with Axial Magnetic Field Strength: Transverse Field=53.5 G.

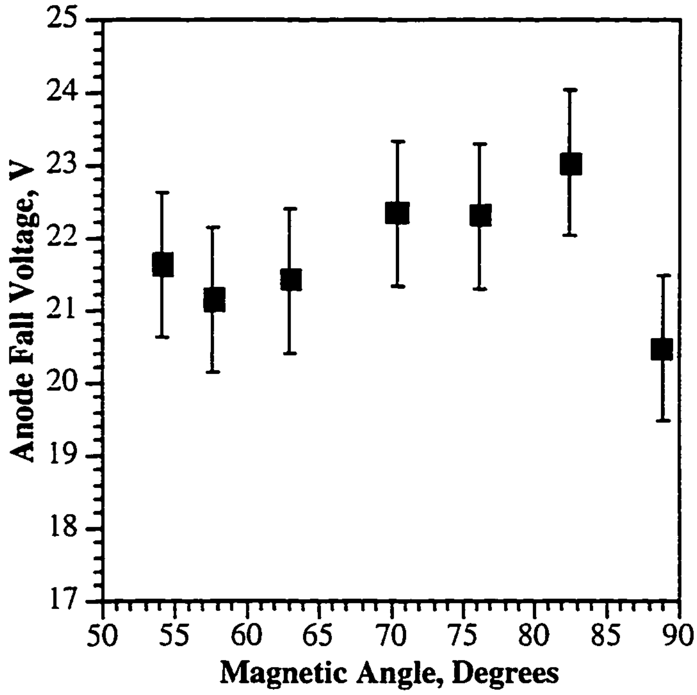

Figure 4.18. Variation in the Anode Fall Voltage with Magnetic Field Angle: Transverse Field=53.5 G.

Power deposition measurements indicate that even though the discharge voltage and the anode fall voltage decreased slightly, the measured power flux changes from the zero axial field case to the end of the range was too small to be detected given the sensitivity of the apparatus.

The argon spectra showed no appreciable variations at the higher magnetic field strength (See Figure 4.19). The density normalized spectra data shown in Figures 4.20 show slightly more structure than the raw spectra as the axial field is varied. The density normalized neutral lines were more responsive to changes in the axial magnetic field than the ion lines at this operating point. Here, as seen from the neutral line variations, the density normalized spectra suggest that there is a gradual increase in the average energy per electron as the axial magnetic field increases. Such trends are attributed to better confinement of primary electrons due to the axial magnetic field.

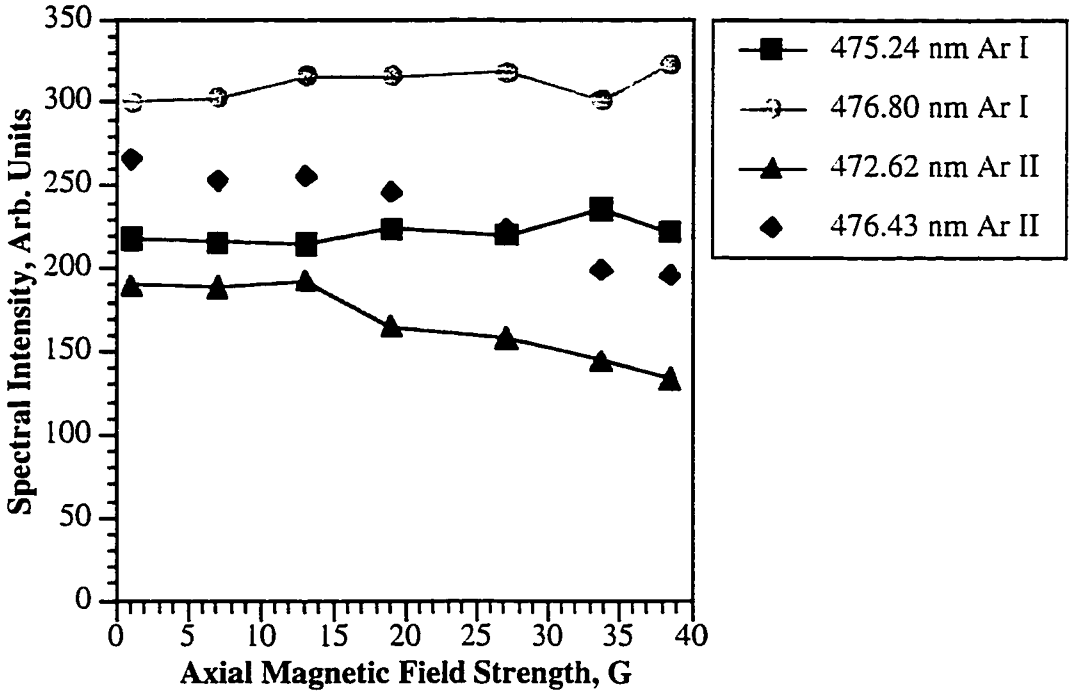

Figure 4.19. Argon Ion Intensity Variations with Axial Magnetic Field: Transverse Magnetic Field=53.5 G.

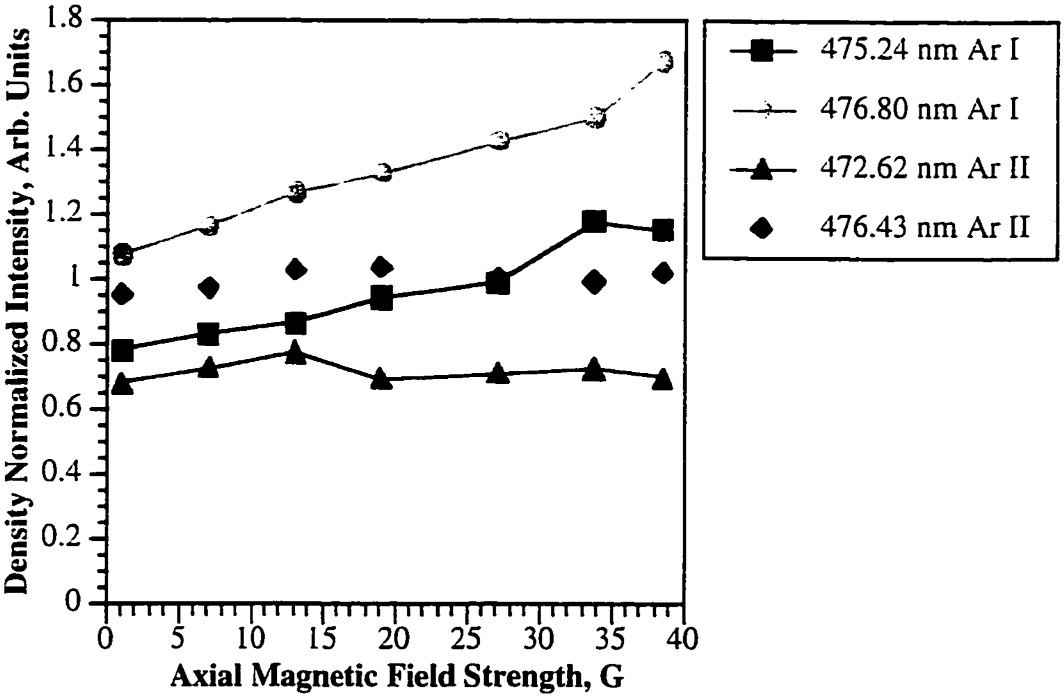

Figure 4.20. Argon Ion Density Normalized Intensity Variations with Axial Magnetic field: Transverse Magnetic Field= 53.5 G.

4.5. Conclusion

All in all, the axial magnetic field appears to have no significant effect on the measured anode fall voltage. For the most part, the axial field gives rise to changes in available current and local electron number density. These changes are most likely related to the influence of the axial magnetic field on radial electron confinement. Such an effect should in general give rise to decreases in the electric field in the positive column.[10] These effects apparently do not trickle down into the near-anode region. This is possibly a consequence of the localized nature of the axial field used in this investigation. The anode fall voltage changes with axial magnetic field strength do appear to be consistent with the measured variations in the available current and the local electron number density. These changes, however, are small. In general it is found here that it is the transverse magnetic field that dominates anode fall behavior. As the transverse magnetic field increased, the effect of the axial field on plasma properties such as spectra appeared to lessen. In addition, the anode fall is on average unresponsive to changes in magnetic field angle as long as the transverse component is fixed. Indeed, the "focusing" or sheath shorting effects are expected to occur only if the transverse component decreases at fixed or increasing axial magnetic field strength.

Notes to Chapter 4

[1] W. Schall, Proceedings of the AIAA 9th Electric Propulsion Conference, AIAA-72-502, (American Institute of Aeronautics and Astrounautics Press, Washington D.C., 1972).

[2] R. Myers and G. Soulas, Proceedings of the 23rd International Electric Propulsion Conference, IEPC-93-194, (The Electric Rocket Society Press, Columbus, OH, 1993).

[3] J.T. Scheuer, et al., Proceedings of the AIAA 23rd International Electric Propulsion Conference, IEPC-93-118, (The Electric Rocket Society Press, Columbus, OH, 1993).

[4] R.P. Hoyt et al., Proceedings of the AIAA 30th Joint Propulsion Conference, AIAA 94-2992, (The Electric Rocket Society, Columbus, OH, 1994).

[5] H. Kerkow, D. Boubetra, and K. Holldack, Nucl. Instrum. Methods Phys. Res. B68, 41 (1992).

[6] M. Sugawara, The Physics of Fluids, Vol. 9, No. 4, 797 April (1966).

[7] K. Gon-Ho, Ph.D. Thesis, Department of Nuclear Engineering, University of Wisconsin. 1993.

[8] D. Lide, Editor, CRC Handbook (CRC Press, New York, 1996), pp. 10-130 - 10-133.

[9] T. Cox et al., J. Phys. D: Appl. Phys. 20, 820 (1987)

[10] F. Chen, Introduction to Plasma Physics and Controlled Fusion (Pergamon Press, New York, 1984), Chapter 5, p. 174.

CHAPTER 5

THE EFFECT OF AN AUXILIARY DISCHARGE ON ANODE SHEATH POTENTIALS IN A TRANSVERSE DISCHARGE

5.1. Introduction

Findings from the characterization experiment elaborated upon earlier suggest that ionization phenomena in the near-anode region influence the magnitude of the anode fall voltage.[1] These findings also suggest that such ionization phenomena are a function of the transverse magnetic field. Because of the anode fall voltage's dependence on the local ionization rate and electron number density, the anode fall voltage indirectly becomes a function of the transverse magnetic field. Led by this reasoning, experiments were designed to specifically modify charge production in the near-anode region at a fixed transverse magnetic field strength in an attempt to reduce the anode fall voltage. Of these experiments, the one that was most successful in altering the magnitude of the near-anode electron number density was that which utilized an auxiliary discharge.

The primary aim of the auxiliary discharge study was essentially three-fold:

1.) To determine to what degree that the near-anode plasma can be modified by the use of an auxiliary discharge;

2.) To determine the effect of an auxiliary discharge on measured anode fall voltage and anode power flux; and

3.) To determine possible correlations between changes in the anode fall voltage and anode power deposition with changes in near-anode plasma conditions such as electron number density and transverse flux caused by the operation of the auxiliary discharge.

The effect of the auxiliary discharge on the near-anode plasma is analyzed using a near-anode single Langmuir probe, emission spectroscopy, and water calorimetry.

5.2. Motivation and Theory

As was pointed out earlier, large power losses at the anode of certain classes of plasma accelerators preclude them from serious consideration for near-term space application. A model for the power flux into the anode is given by Cobine:[2]

$$P_a = I_d \cdot [V_a + \frac{5kT_e}{e} + \phi_{wf}] + P_{c,r} . \qquad (5.1)$$

Here P_a is the energy deposited into the anode per unit time, I_d is the discharge current, V_a is the anode fall voltage (sheath potential drop), T_e is the electron temperature, ϕ_{wf} is the work function of the anode, and finally $P_{c,r}$ is the power contribution due to plasma convection and cathode radiation. Past studies related to $\bar{E} \times \bar{B}$-type plasma accelerators indicate that the anode fall term is the dominant anode heating source. These findings have been verified by more recent experiments in a transverse discharge diode configuration.[1,3]

Changes in the magnitude of the transverse magnetic field has been shown to have a marked effect on the magnitude and possibly the sign of the anode fall voltage.[1,4] In this study only positive, electron attracting sheath potentials have been observed in the presence of a transverse magnetic field and thus only potentials of this type will be discussed.

In general, the magnitude of the transverse magnetic field controls the transverse flux. Both the transverse diffusion coefficient, $D_\perp$, and the transverse electrical conductivity, $\sigma_\perp$, are reduced when the transverse magnetic field is increased from zero.[5,6] The reduction in the magnitude of these two parameters is on the order of the factor: $\frac{1}{[1+\frac{\omega_{ce}^2}{\nu_c^2}]}$. Here $\frac{\omega_{ce}}{\nu_c}$, referred to as the Hall parameter, is the ratio of the electron cyclotron frequency to the electron collision frequency. At large transverse magnetic field values, the amount of current that can be supported by the discharge is significantly reduced. Sugawara derived and experimentally tested an expression for the transverse current available in a given plasma for a planar Langmuir probe with a collection surface of area S as a function of transverse magnetic field strength:[7]

$$I_{e\perp} = \frac{1}{4} \cdot e n_o \bar{v}_e S \cdot [\frac{16}{3} \cdot \frac{\lambda_e \alpha^{\frac{1}{2}}}{K(k) \cdot r_o}] \cdot \frac{1}{1 + \frac{16}{3} \cdot \frac{\lambda_e \alpha^{\frac{1}{2}}}{K(k) \cdot r_o}}. \tag{5.2}$$

Because Equation 5.2 is evaluated at the plasma potential, $I_{e\perp}$ corresponds to the electron saturation or diffusion current available to the anode. The potential distribution across the anode sheath is determined by the charge distribution in the sheath itself. This charge distribution in turn is controlled by the available flux diffusing into the sheath from the adjacent positive column. In this respect, the magnetic field can control the anode sheath potential difference by controlling the flux in the near-anode region. Experimental results suggest that it is this relationship between the magnetic field and the response, flux and ultimately local electron density, that is responsible for the anode sheath potential variations with the transverse magnetic field.[1]

Again, findings from earlier investigations suggest that the magnitude of electron number density, whose steady-state value is determined by the transverse flux, play a major role in determining the magnitude of the anode sheath potential difference. Led by these observations, methods to artificially alter near-anode plasma properties at a fixed magnetic field strength were investigated. The most successful method investigated consisted of the operation of an additional, quasi-independent discharge. The main idea behind the concept is based on the fact that an auxiliary electron source could be used to generate additional electron-ion pairs, thus enhancing the conductivity in the both the positive column and the near-anode region in particular. The application of auxiliary discharges to help sustain an otherwise non-sustaining discharge plasma has been used to enhance the performance of CO_2 lasers.[8,9] In certain cases, an electron beam or an auxiliary discharge is used to maintain the proper ionization levels to sustain the discharge while the main discharge electrodes are used to develop an ideal electric field to neutral particle density ratio so as to optimize electron excitation of the laser transition.[8,9] The auxiliary discharge electrons are shared between discharges, benefiting both. The auxiliary discharge essentially plays the role as another energy source that enhances the electron density which in turn increases the electron flux.

5.3. Experimental Considerations

For this investigation, an 8.8 A arc is maintained between the cathode and anode. This operating point gives rise to an anode current density of roughly $2 \frac{A}{cm^2}$, which is comparable to conditions observed at the anodes of steady-state 100 kW class MPD thrusters.[10]

5.4. Description of the Auxiliary Discharge Apparatus and Operation

As mentioned earlier, the purpose of the auxiliary discharge is to modify discharge plasma properties particularly in the near-anode region. The auxiliary discharge apparatus itself is illustrated in Figure 5.1. The unit consists of three rectangular molybdenum (Mo) plates 2.8 cm by 4.3 cm and a filament cathode bus all mounted to but electrically and thermally isolated from an aluminum mounting frame. The cathode consists of three oxide-coated, thoriated tungsten wire coils. The oxide paint enhances thermionic emission by lowering the cathode's work function. During operation, electron collection occurs at plate A only (see Figure 5.1). As such, electrons emitted from the filament are launched and confined along the magnetic field lines. For this investigation, plates B and C were allowed to float to provide a measure of radial confinement of electrons in the discharge gap enclosed by the auxiliary apparatus. An additional benefit of the arrangement of the plates is the formation of a higher pressure region within the auxiliary region between the plates which enhances ionization processes there. Also, the floating plates B and C shielded the spectrometer from radiation emitted by the glowing filaments.

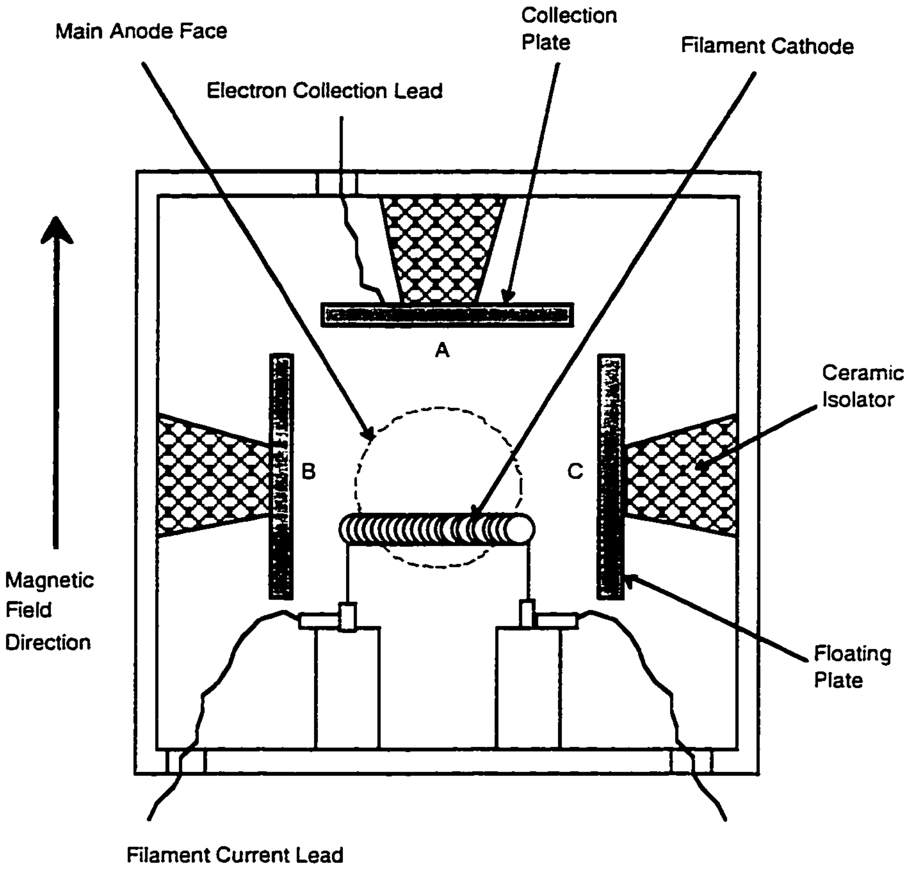

Figure 5.1. Auxilary Discharge Apparatus.

The auxiliary discharge apparatus was placed downstream of the anode (see Figure 5.2) with the Mo collection plate edge lying only 3 mm downstream of the anode. The filaments used in this investigation were operated at emission currents which ranged from 0.0 to 1.3 A. Though the precise mechanisms underlying the enhancement of electron number density in the near-anode region due to the application of an auxiliary discharge is not totally understood, the benefits of the operation of the auxiliary discharge on overall main discharge characteristics, however, are surmised to be associated with:

1.) Enhancing of electron bombardment events from an additional electron source;

2.) Increasing ionization due to an additional electric field associated with the auxiliary discharge; and

3.) Replacing plasma electrons lost to the collection plate by electron emission and production driven by the auxiliary cathode.

This final point is of significance in that the auxiliary anode can collect electrons from the main discharge that would ordinarily diffuse away along the magnetic field. As is the case, the electrons emitted from the filament cathode can contribute more directly to main discharge processes, acting as a source by both direct emission and charge pair production when the associated auxiliary discharge ionization is taken into account. All in all, the apparatus itself is a tool that provides the means by which discharge plasma properties can be significantly altered. The goal of this investigation is to show that the changes in the main discharge voltage and the anode fall voltage brought on by the auxiliary apparatus are consistent with the expected changes in electron number density and flux.

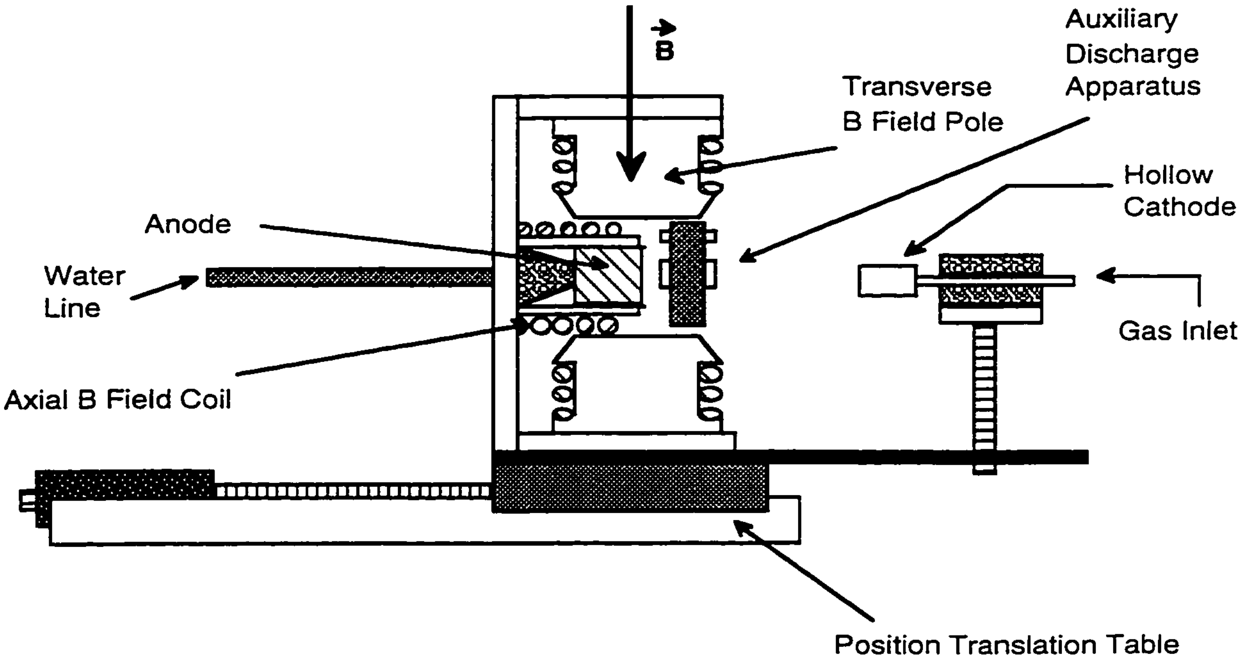

Figure 5.2. Auxiliary Discharge Apparatus with Main Discharge Hardware.

While operating the auxiliary discharge, the glow from the cathode filaments contribute to the power flux deposited into the anode. In order to account for this, the filament is operated at its nominal heating current of 15 A before the experiment with the discharge off. Power flux due to the filament radiation is then measured. This power is subtracted from the measured anode power flux when the discharge is operating so as to obtain the anode power deposition associated with the discharge only. In addition, this glow has the potential for skewing the intensity profile of collected emission spectra taken by the spectrometer. This effect was found to be fairly small (<3%). The effect of this continuum radiation was reduced for a number of reasons: 1.) The filaments were located between the molybdenum plates and thus were obscured from view of the spectrometer; 2.) The continuum radiation that did scatter into the spectrometer does not change significantly over the wavelength range scanned; and 3.) The peak of the blackbody-like radiation lies far from the wavelength range scanned.

5.5. Experimental Results

One major goal of this study was to artificially modify the electron number density and the transverse flux in the near-anode region and measure the effect of these changes on the anode fall voltage and the anode power deposition. Changes in near-anode plasma properties are measured as a function of filament discharge current at a fixed transverse magnetic field intensity and a fixed main discharge current. In this study, the effect of the auxiliary discharge on a 8.8 A argon discharge was investigated at two representative magnetic field strengths: 38 G and 108 G.

5.5.1. Correlations between Measured Anode Fall Voltage, Electron Number Density, and Available Transverse Current

Figure 5.3 shows that for the 38 Gauss case, the anode fall was relatively insensitive to changes in the auxiliary discharge current of 0.6 A or less. This behavior is also reflected in the measured electron number density (Figure 5.4) and the available transverse current. The available transverse current as calculated using Equation 5.2 is normalized to the transverse current available at zero auxiliary discharge current (see Figure 5.3). The flatness of the anode fall voltage for these auxiliary currents is interpreted as being directly related to the flatness observed in density and transverse current. Here the plasma conductivity, which should scale with the Hall parameter, is also expected to be constant. In addition, the ratio of the available current to the discharge current inside the anode sheath is also constant. The anode fall voltage should not change under these conditions because excess space charge in the sheath does not vary with the auxiliary discharge current for this current range. For auxiliary discharge currents above 0.6 A, a marked drop in the anode fall voltage is observed. Also accompanying the change in imposed auxiliary discharge current was a significant jump in electron number density and available transverse current. The ratio of available transverse current to discharge current consequently increases under these fixed magnetic field conditions. At this point, there is an increase in negative space charge in the anode sheath. This uncollected space charge suppresses the potential of the anode relative to the sheath edge thereby lowering the anode fall voltage. As illustrated in Figure 5.5, the relatively large drop in the anode fall voltage and the large jump in the electron number density and calculated available current appear to be related to the significant jump (~20 V) in the auxiliary discharge voltage required to sustain the auxiliary discharge currents greater than 0.6 A. The jump in the auxiliary discharge voltage, which is most likely related to changes in filament operation, is postulated to have primarily two effects on the discharge plasma: 1.) Increases in the auxiliary cathode fall voltage enhances ionization along the magnetic field lines because at higher fall voltages the electrons are injected into the positive column at higher energies; and 2.) Increases in the E/p (electric field/gas pressure) ratio along the magnetic field also enhances ionization along the magnetic field.[8] Subsequent increases in the auxiliary discharge current following the jump did not give rise to any appreciable change in the anode fall voltage. The saturation of the anode fall with increasing auxiliary discharge current is also observed in the electron number density and the available transverse current. Again, this observed saturation suggests the relationship between anode fall voltage, electron number density, and available current as predicted by the proposed physical model.

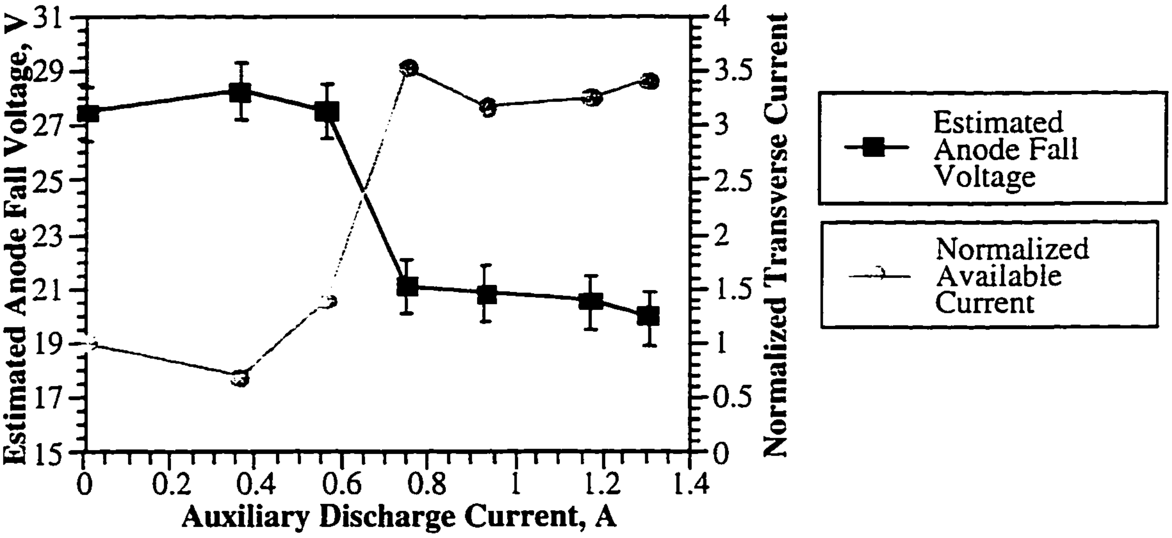

Figure 5.3. Variation of Anode Fall and Normalized Transverse Current with Auxiliary Discharge Current: Transverse Magnetic Field=38 G.

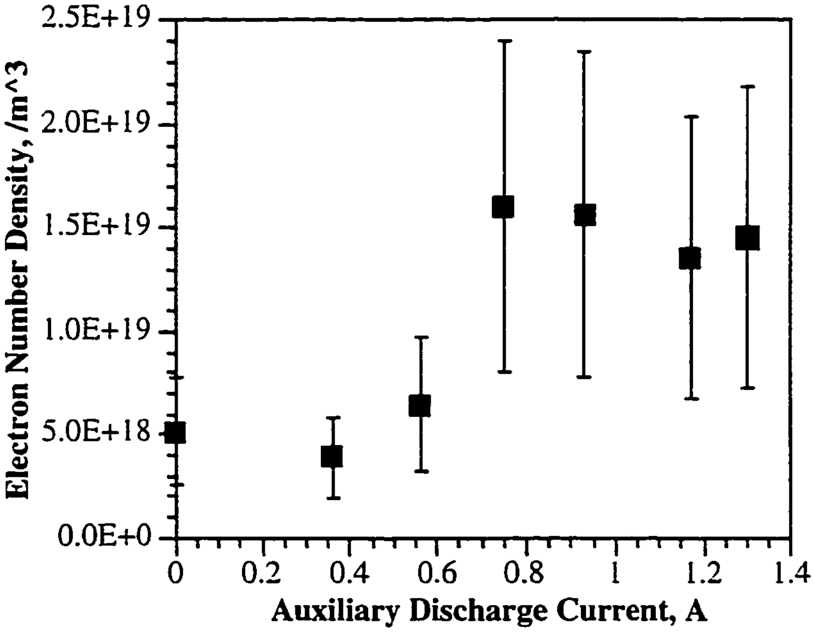

Figure 5.4. Variation of Electron number density with Auxiliary Discharge Current: Transverse Magnetic Field=38 G.

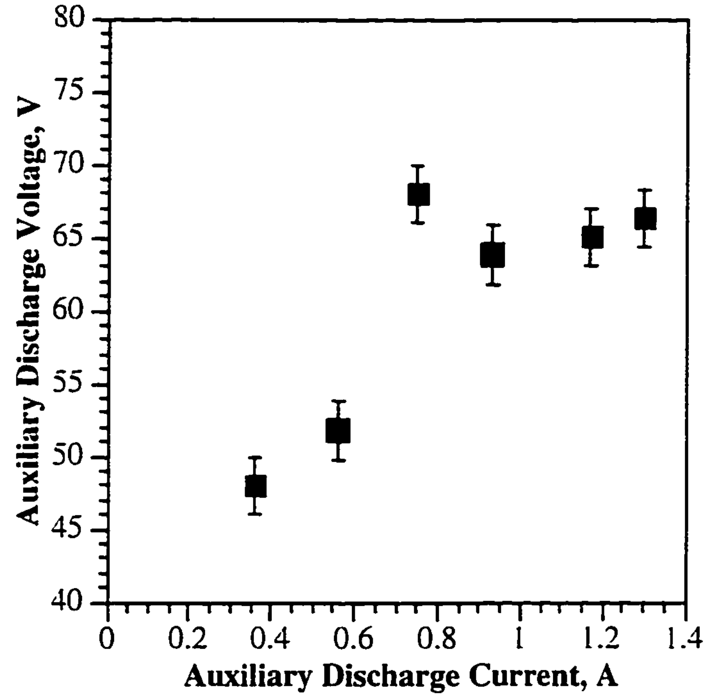

Figure 5.5. Variation of the Auxiliary Discharge Voltage with Auxilary Discharge Current: Transverse Magnetic Field=38 G.

Variations in the anode fall voltage with auxiliary discharge current in the 108 G case (see Figure 5.6) behaved similarly to that which was observed in the 38 G case. Initially, however, the anode fall voltage decreases with increasing auxiliary discharge current until the anode fall saturates with increasing values of auxiliary discharge current. The saturation occurred near an auxiliary discharge current of roughly 0.7 A. Variations in the electron number density and available transverse current were consistent with the observed changes in the anode fall voltage. Here, as the density (Figure 5.7) and the available current (Figure 5.6) increases the anode fall voltage decreases. Saturation in the electron density and available current occur over the same auxiliary current range that the anode fall saturates. Again, this observed behavior is consistent with expected physical processes postulated to occur as the available flux varies.

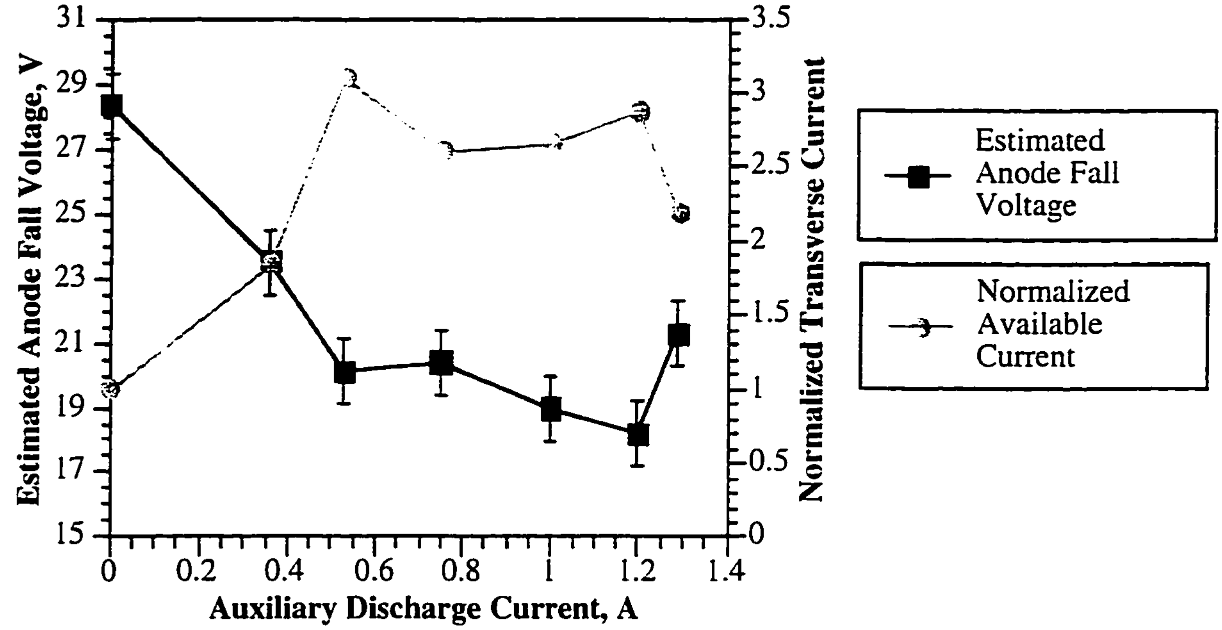

Figure 5.6. Variation in Anode Fall and Normalized Available Current as a Function of Auxiliary Discharge Current: Transverse Magnetic Field=108 G.

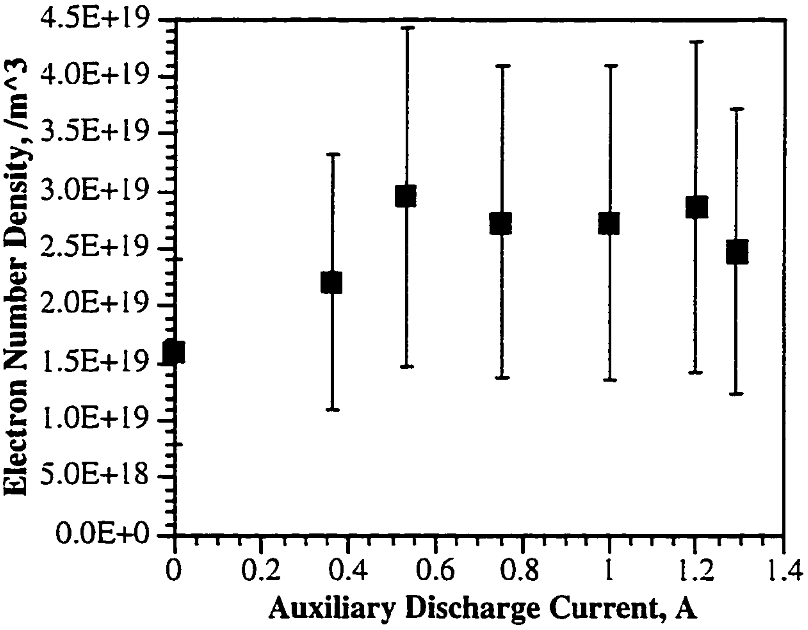

Figure 5.7. Variation in Electron Number Density with Auxiliary Discharge Current: Transverse Magnetic Field=108 G.

For both cases, one possible reason for the apparent insensitivity of the electron number density to changes in auxiliary discharge current at higher emission currents may be a consequence of recombination losses. As the density increases, three body recombination contributes more as a loss mechanism. Still another possible reason for the saturation in the near-anode electron number density as auxiliary discharge current is varied may be related to electron losses at the auxiliary anode itself. As the auxiliary cathode emission current increases, more plasma electrons in the auxiliary discharge region have to be collected by the auxiliary anode. Under these conditions, the auxiliary anode begins to compete with the main discharge for electrons created in this volume as the auxiliary discharge current requirements increase. Saturation in the electron number density is then a consequence of the volume electron/ion production rate balancing losses to the auxiliary anode, the main discharge anode, the chamber wall due to radial diffusion out of the positive column, and the losses due to volume recombination.

Finally, it should be pointed out that in both the 38 G case and the 108 G case, the auxiliary discharge demonstrates its utility in significantly modifying discharge plasma properties such as density and available flux which in turn is associated with marked reductions in the anode fall voltage. It is also worth noting that the main discharge voltage in both transverse magnetic field cases followed the same general trends observed in the anode fall (see Figures 5.8 and 5.9). Indeed, the ratio of the anode fall voltage to the discharge voltage was for the most part independent of the auxiliary discharge current. This constancy is associated with the observation that on average the changes in the main discharge voltage can be directly attributed to changes in the anode fall voltage. This behavior suggests that the effect of the auxiliary discharge on the potential distribution across the arc is most pronounced in the anode fall region.

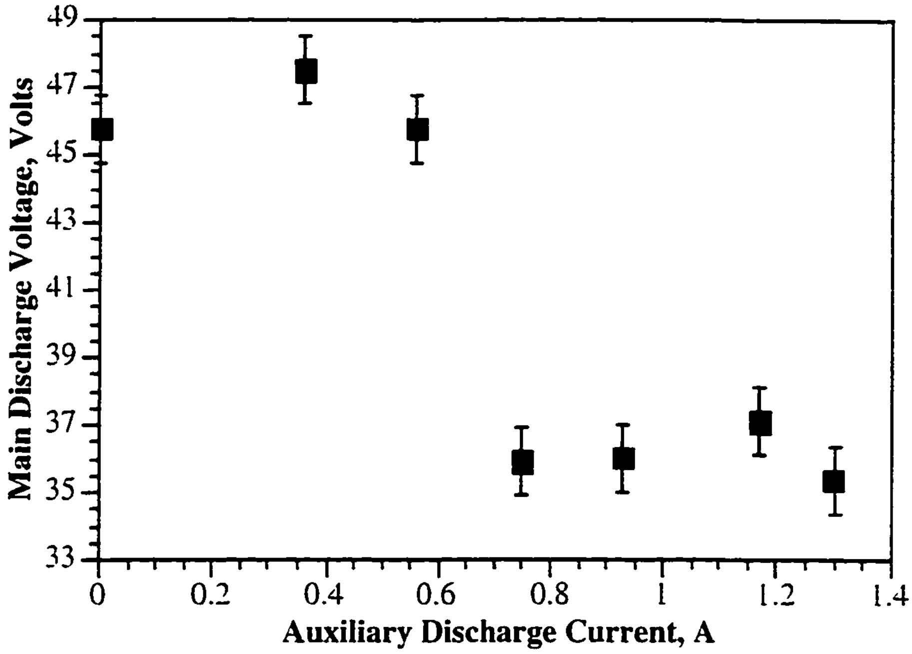

Figure 5.8. Main Discharge Voltage Dependence on Auxiliary Discharge Current: Tranverse Magnetic Field=38 G.

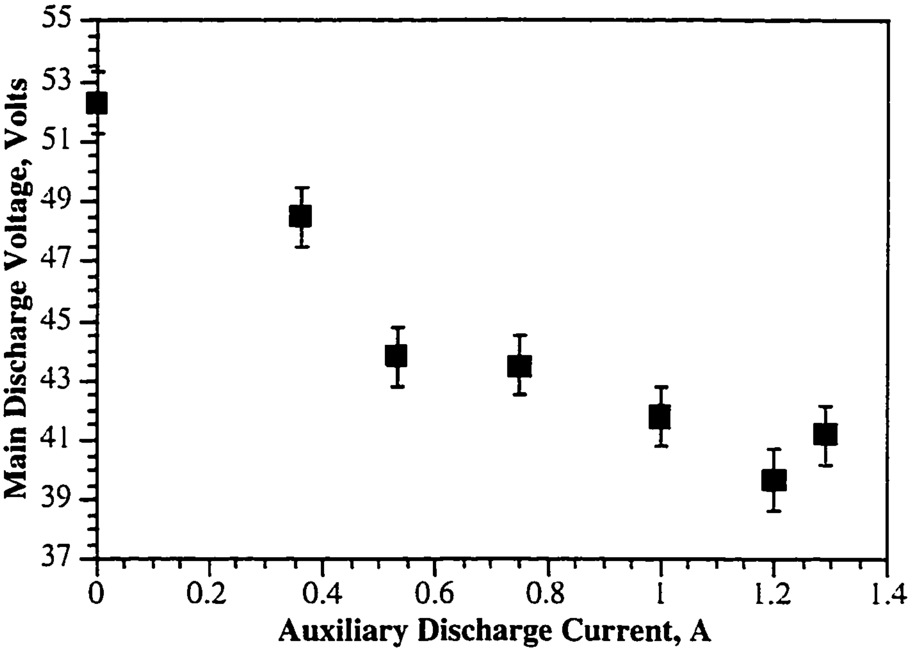

Figure 5.9. Main Discharge Voltage Dependence on Auxiliary Discharge Current: Transverse Magnetic Field=108 G.

5.5.2. Electron Energetics: EEDF and Emission Spectra

The auxiliary discharge has the ability to significantly modify the electron number density and the available transverse flux. Such modifications indicated that the auxiliary discharge must be influencing ionization processes in the near-anode region. Ionization in the volume enclosed by the auxiliary discharge electrodes gives rise to additional ion/electron pairs which diffuse out of this region and flow in the positive column and the near-anode region. EEDF measurements made for this investigation suggest that the energy distribution of the electrons in the near-anode region are not appreciably affected by these processes. Although there is some evidence of EEDF expansion into higher energies. for the most part, as illustrated in Figures 5.10 and 5.11 the curves are fairly insensitive to changes in the auxiliary discharge current. This insensitivity to changes in the auxiliary discharge current is reflected in the ionization rates (see Figure 5.12) calculated by integration of the EEDFs.

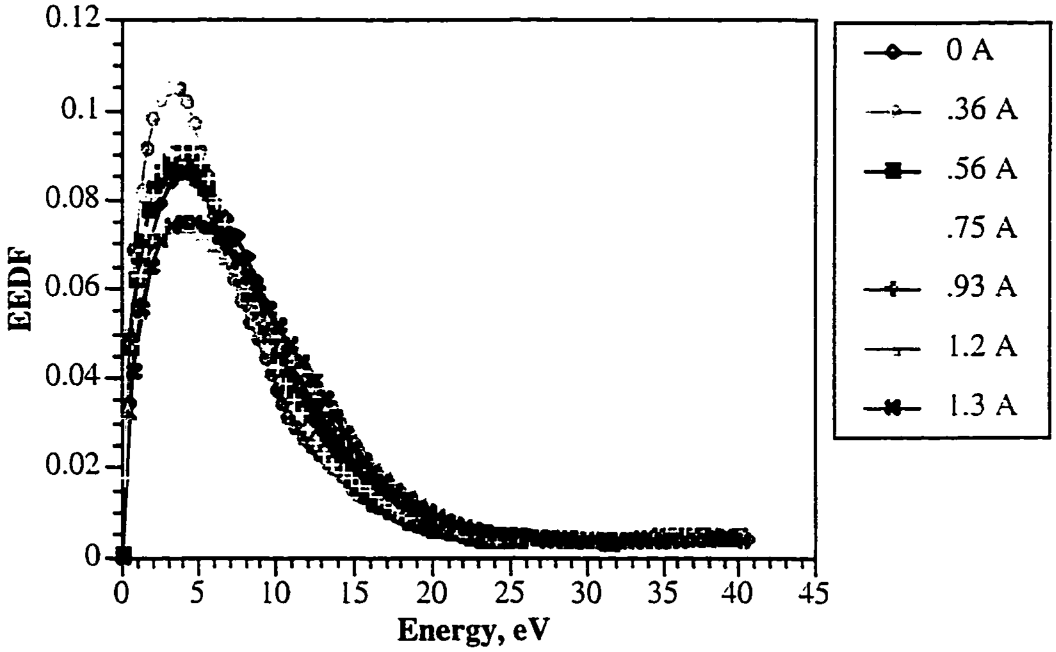

Figure 5.10. Variations in EEDF with Auxiliary Discharge Current: Transverse Magnetic Field=38 G.

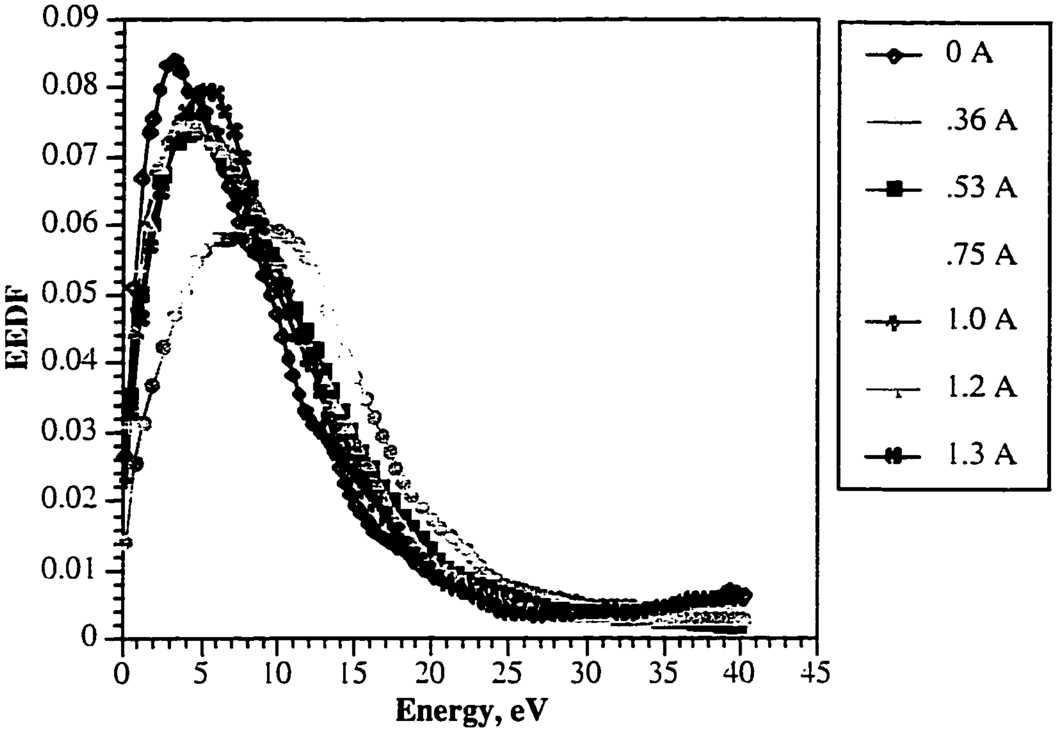

Figure 5.11 Variations in EEDF with Auxiliary Discharge Current: Transverse Magnetic Field=108 G Case.

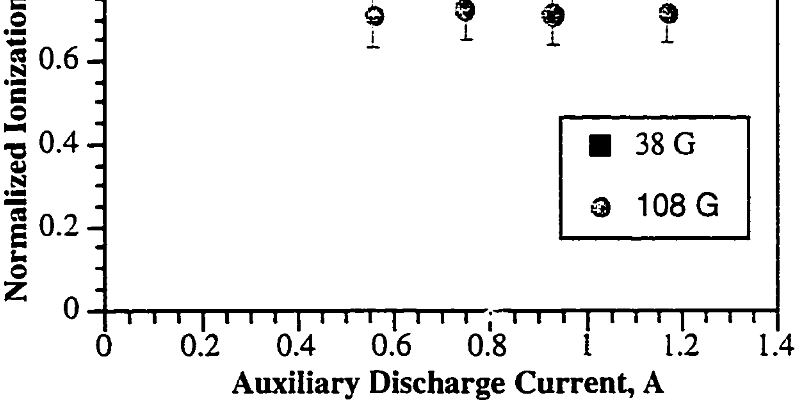

Figure 5.12. Variations in the Ionization Rate per Electron with Auxiliary Discharge Current.

The Langmuir probe used to make the EEDF measurements was aligned parallel to the magnetic field so that the energy measurements were sensitive to only those velocity components perpendicular to the surface of the probe. Energy components parallel to the probe's axis, and thus parallel with the magnetic field, cannot be detected by the probe. Because the electric field of the auxiliary discharge is parallel to the magnetic field, such a field can impart energy along this direction to electrons diffusing into this region. In this respect that energy component associated with the velocities parallel to the magnetic field can be altered thus possibly increasing the anisotropy of the total EEDF, which would be undetectable by this set-up.

Although an investigation into the anisotropy of the resulting EEDF is left to a future study, insight into the behavior of the near-anode electron population as a function of auxiliary discharge current can be obtained by an analysis of the emission spectra. Spectral intensity variations of three singly charged argon ion lines varied roughly as the anode fall voltage with changes in auxiliary discharge current. In general, when the auxiliary discharge was turned on, the discharge was observed to dim. The ion spectra reveals these trends. A dimming in intensity of the ion lines suggests that either the ion population is decreasing or that the number of electrons capable of exciting the ions is decreasing. Normalizing the raw intensity data (see Figures 5.13 and 5.14) with respect to the electron density yields a quantity that is proportional to the fraction of electrons with energies greater than the excitation threshold of the line in question. The excitation threshold for the argon ion lines associated with Figures 5.13 and 5.14 is 35 eV.[11] These data suggests that for auxiliary discharge currents less than one ampere, the fraction of electrons with energies capable of exciting the ion lines decreases with increasing auxiliary discharge current. The observed increases in this parameter at auxiliary discharge currents greater than one ampere for the 108 G case is attributed to similar increases observed in the auxiliary discharge voltage. It is interesting to note that the general shapes of the intensity plots in Figures 5.13 and 5.14 are remarkablely similar to the measured variations in discharge voltage thus illustrating the response of the energetic electrons to the main discharge voltage.

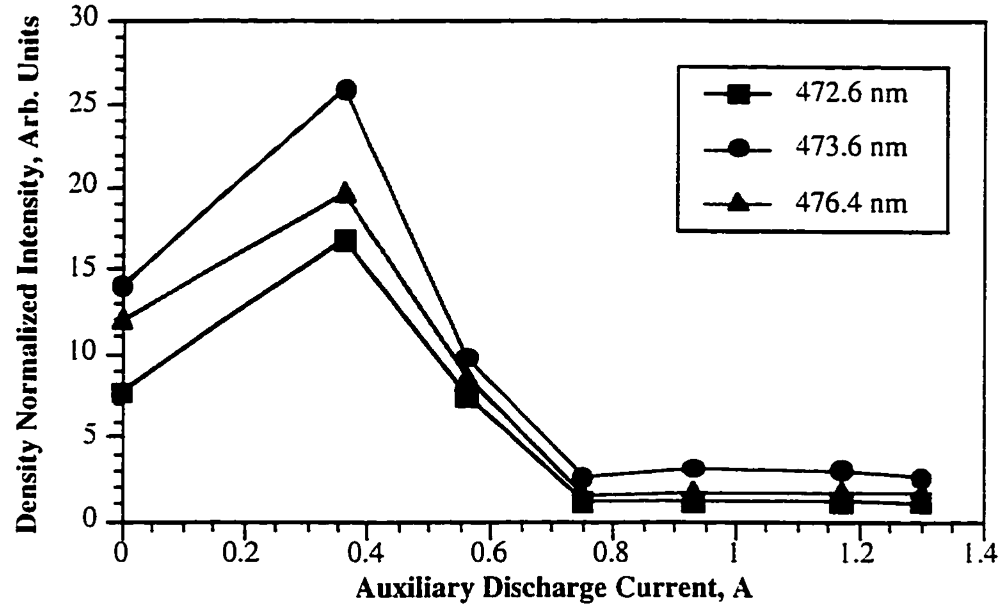

Figure 5.13. Variations in Density Normalized Intensity versus Auxilary Discharge Current: Transverse Magnetic Field=38 G.

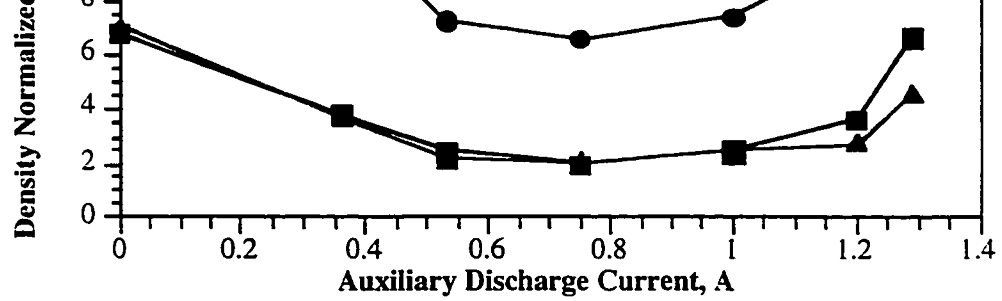

Figure 5.14. Variations in Density Normalized Intensity versus Auxilary Discharge Current: Transverse Magnetic Field =108 G.

5.5.3. The Effect of the Auxiliary Discharge on Anode Power Deposition

In general, the reduction in the measured anode power flux followed the measured changes in anode fall voltage as the auxiliary discharge current was varied. Even so, the anode fall power term in Cobine's power flux relation dominated measured anode power deposition (see Figure 5.15). However, in both cases the magnitude of power deposited into the anode decreased with increasing auxiliary discharge current. These reductions in the anode fall voltage gave rise to reductions in deposited anode power as large as 25% in the 108 G case and as large as 15% in the 38 G case (see Figure 5.16). If similar reductions in anode power flux could be achieved in MPD thruster systems, efficiencies as high as 55% or better could be realized. At such power levels, the MPD thruster becomes a more realistic propulsion option for energetic space missions.[12]

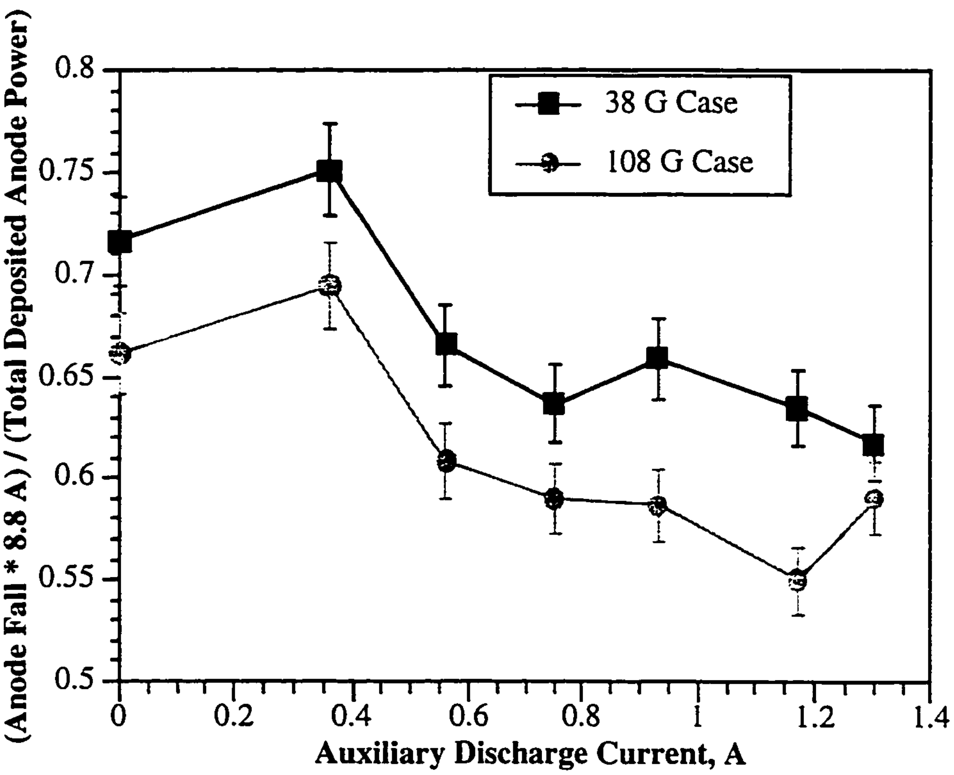

Figure 5.15. Contribution of Anode Fall* 8.8 A to Total Anode Power Deposition.

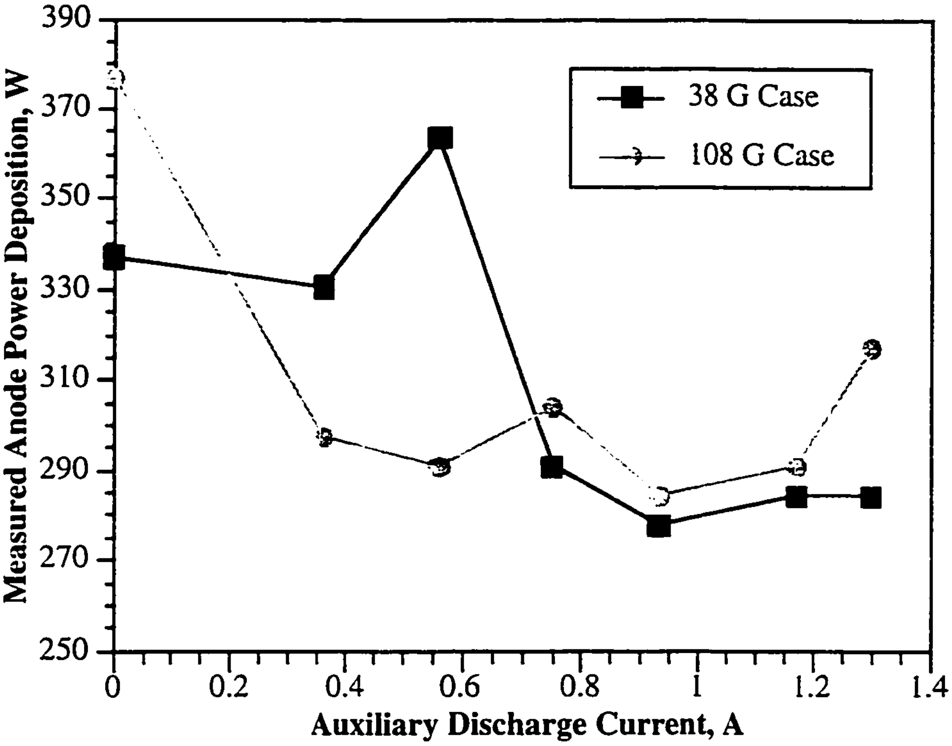

Figure 5.16. Measured Anode Power Deposition as a Function of Transverse Magnetic Field.

5.6. Implications for MPD Thrusters

Findings from this investigation suggest possible means for reducing anode fall voltage in MPD thrusters. Throughout this work, it has been emphasized that the electron number density and magnitude of the relative available transverse flux in the near-anode region play key roles in determining the anode fall voltage. In MPD thrusters the goal is then to increase the relative magnitudes of these parameters at a given thruster operating point. Here, three possible means of achieving these ends are presented and briefly commented upon.

5.6.1 Injection of Pre-ionized Propellant

The injection of pre-ionized propellant into the MPD discharge chamber is perhaps the most direct way to increase the electron density population in the near-anode region. One practical way of accomplishing this is to utilize a plasma contactor as the propellant injector.[13] The plasma contactor, which consists of a hollow cathode enclosed within a coaxial anode, ionizes the propellant that flows through it. As illustrated in Figure 5.17, this mix of partially ionized gas and neutrals that flows from the orifice of the contactor feeds the main discharge chamber. By varying the plasma contactor discharge current, the ionization fraction of the injected propellant can be varied. In order to enhance the coupling of the pre-ionized gas to the near anode region, the fluid can be injected tangentially or through insulated holes in the anode itself. The only negative aspect of this scheme is associated with the fact that additional power supplies must be utilized to operate the pre-ionizers, thus complicating the hardware simplicity associated with MPD thrusters. The system's complexity, however, may be offset through its inherent positives associated with the plasma contactor which include long lifetime and low power consumption.[18]

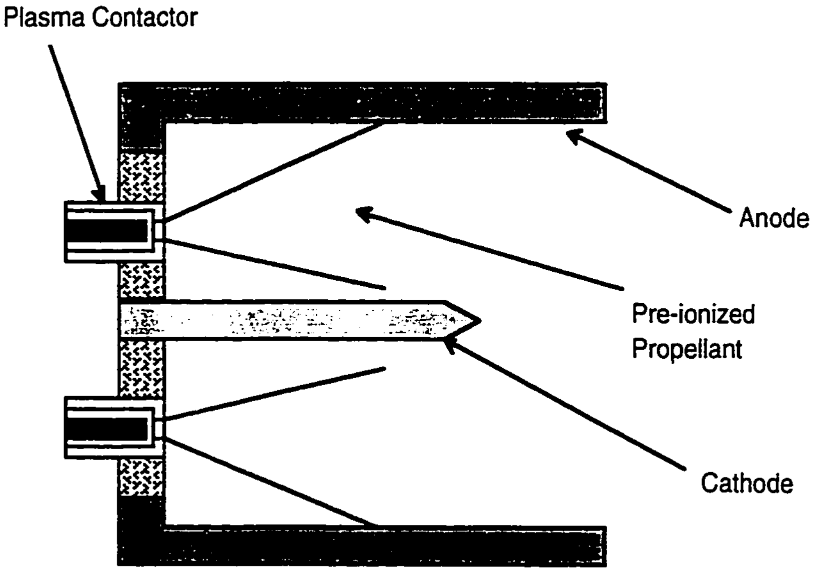

Figure. 5.17. Injection of pre-ionized propellant.

5.6.2. Consumable Anode Insert

Past researchers have postulated that vaporization of anode material by anode spots can control the behavior of anode power deposition by giving rise to saturation of the anode fall voltage.[14,15] This observation suggests still another possible means of increasing ionization in the near-anode region. One possible scheme is to utilize an anode made up of an easily ionizable metal such as zinc. This scheme is reminiscent of MPD engines which used metal propellants such as lithium.[16] The liquid metal approach, however, is not attractive due to environmental safety concerns related to the contamination issues and general spacecraft integration questions. If used for essentially primary propulsion, the consumable anode scheme would, however, be essentially immune to most of these concerns, ground-testing notwithstanding. In the consumable anode scheme, as the anode fall increases, the amount of thermal energy that is deposited into the anode also increases. Eventually, the heating of the insert gives rise to evaporation of anode material that is subsequently ionized, thus enhancing the conductivity of the near-anode plasma. This scheme (see Figure 5.18.) is active in that the amount of metal vapor from the anode that enters into the plasma depends on the magnitude of the anode fall. In steady-state, the anode fall should saturate because increases in anode fall gives rise to increases in metal vapor which in turn should bring the anode fall down to a steady-state value. By carefully selecting the insert anode material, a limit on the largest anode fall that will develop can be established. A secondary concern associated with this concept involves the lifetime of the anode. It is conceivable, however, that a consumable anode of sufficient thickness and hence lifetime can be successfully utilized to control the anode life problem.

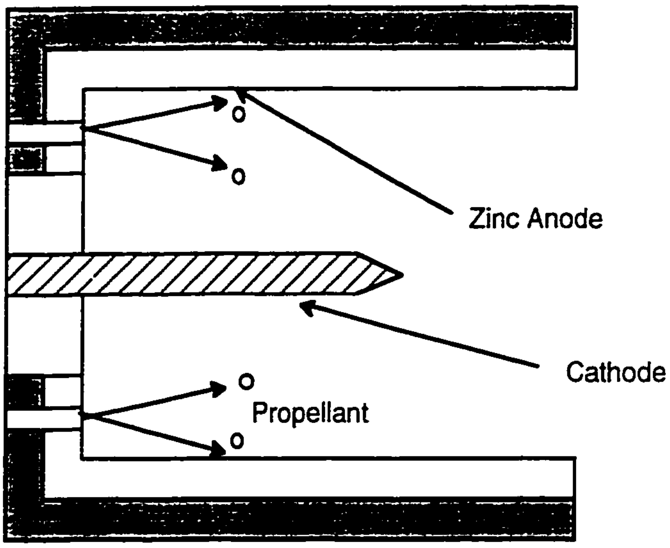

Figure 5.18. Consumable Anode Scheme.

5.6.3. Increasing Discharge Chamber Pressure

A "free burning" arc study conducted by Soulas and Myers[3] showed that increasing the local pressure decreases the anode fall voltage at a fixed transverse magnetic field strength. In addition, an MPD thruster study conducted by Myers indicated that thruster anode radius and flow rate affects the anode fall voltage.[12] The anode fall voltage was found to drop with increasing propellant flow rate and reduced discharge chamber radius. In general, decreasing the anode radius and/or increasing the propellant mass flow rate increases the discharge chamber pressure. These studies suggest yet another means for increasing ionization in the near-anode region. Because the density of neutrals increases with increasing pressure, the ionization probability for a given electron increases as well. As density increases, so must the available transverse flux. In order to enhance ionization phenomena in the near-anode region, propellant injection through efflux holes in the anode itself may be implemented. This hollow anode scheme, illustrated in Figure 5.19, would allow for a higher local neutral density in the near-anode region thus increasing the likelihood of increased ionization occurring there.

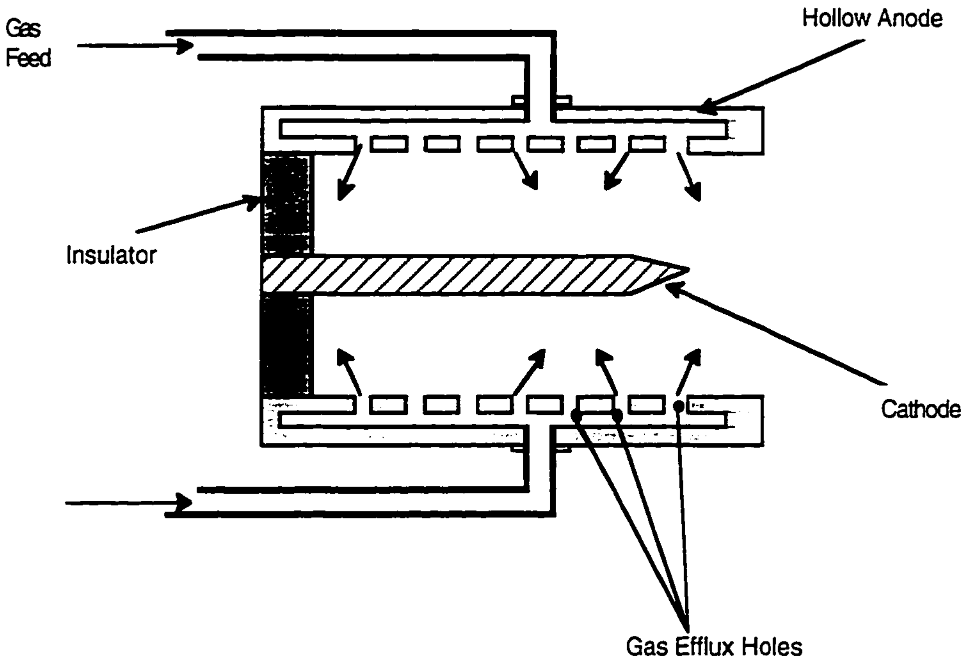

Figure 5.19. MPD with "Hollow Anode."

5.7. Summary

Significant modifications to the near-anode plasma of a transverse discharge was demonstrated through the application of an auxiliary discharge. Marked increases in the electron number density and available transverse flux brought on by the use of the auxiliary discharge gave rise to moderate reductions in the anode fall voltage. The main discharge voltage behavior was similar to the anode fall as the auxiliary discharge current was varied. One puzzling aspect of this study surrounds the relative insensitivity of the EEDF to changes in the auxiliary discharge current. This finding suggests that from an energy standpoint, the bulk electron population was not appreciably affected by the operation of the auxiliary discharge. However, possible anisotropy in the EEDF due to electric fields or an electron beam component associated with the auxiliary discharge could play an important role in determining overall ionization rates. Because the anode fall voltage dominates anode power deposition in this transverse discharge, decreases in the anode fall voltage gave rise to reductions in the measured anode power deposition as large as 25%. If such reductions in anode power flux could be made in MPD thrusters, these devices would then make a more realistic candidate for energetic space missions. The effect of an auxiliary discharge can possibly be achieved in MPD engines by utilizing components which enhance the near-anode electron number density. Such systems changes range from the use of pre-ionizers to increasing the pressure in the near-anode region of the discharge chamber. All of these possible techniques must be economical, clean, and robust in order to minimize spacecraft integration issues.

Notes to Chapter 5

[1] J.E. Foster and A.D. Gallimore, Accepted for publication in Physics of Plasmas Journal. 1996.

[2] J. Cobine and E. Burger, J. Appl. Phys., 26, 895, (1955).

[3] G. Soulas and R. Myers, Proceedings of the 23rd International Electric Propulsion Conference, IEPC 93-194, (The Electric Rocket Society, Columbus, Ohio, 1993).

[4] H. Hugel. IEEE Transactions on Plasma Science, vol. PS-8, no. 8, 437, December (1980).

[5] F. Chen, Introduction to Plasma Physics and Controllable Fusion (Plenum Press, N.Y., 1984), Chapter 5, Sect. 5.10.

[6] H. Kaufman, Operation of Broad Beam Ion Sources (Commonwealth Scientific Corporation, Virginia, 1984), Chapter 15, Sect. G.

[7] M. Sugawara, The Physics of Fluids, vol. 9, no. 497, April (1966).

[8] Y.P. Raizer, Gas Discharge Physics (Springer-Verlag, N.Y. 1991), Chapter 4, Sect. 4.1 and Chapter. 14, Sect. 14.3.4.

[9] R.E. Beverly III, Proceedings of the SPIE 7th International Symposium on Gas Flow and Chemical Lasers, vol. 1031, 1988.

[10] A.D. Gallimore, A. Kelly, and R. Jahn, AIAA Journal of Propulsion and Power, vol. 9, no.3, 361, (1993).

[11] T.L. Cox, V.G.I Deshmukh, D.A.O. Hope, A.J. Hydes, N. St. J. Braithwaite, and N.M.P. Benjamin, J. Phys. D: Appl. Phys., 20, 820 (1987).

[12] R. M. Myers, M. Mantenieks, and J. Sovey, Proceedings of the 21st International Electric Propulsion Conference, AIAA 90-2669, (American Institute of Aeronautics and Astronautics Publishing, Washington D.C. 1990).

[13] G.C. Soulas, Proceedings of the 30th AIAA Joint Propulsion Conference, AIAA 94-3310, (American Institute of Aeronautics and Astronautics Publishing, 1994).

[14] K.D. Diamant, E.Y. Choueiri, and R.G. Jahn, Proceedings of the 25th International Electric Propulsion Conference, IEPC 95-234, (The Electric Rocket Society, Columbus, Ohio, 1995).

[15] J.C. Metcalf and M.B.C. Quigley, Proceedings of the Third International Conference on Gas Discharges, (Institute of Electrical Engineers, London, 1974).

[16] D.B. Fradkin, Ph.D. Thesis, Princeton University, Department of Aerospace and Mechanical Engineering, 1973.

CHAPTER 6

THE ANODE SHEATH POTENTIAL MODEL

6.1. Introduction

Experimental findings discussed in the earlier chapters provide much evidence in support of the claim that ionization phenomena in the near-anode region play an important role in determining the anode fall voltage. Near-anode ionization processes control the magnitude of the local electron number density and to a certain extent, the value of the transverse electron flux. These ionization processes vary with transverse magnetic field. In addition to affecting ionization processes, the transverse magnetic field also reduces the available electron transverse flux. In this respect, if changes in ionization processes are insufficient to offset reductions in the transverse diffusion coefficient as the transverse magnetic field increases, then the ratio of available transverse electron flux to the collected discharge flux decreases. Physically, reductions in the available transverse flux relative to the collected discharge flux gives rise to reductions in negative space charge throughout the anode sheath. In this respect, the potential of the anode due to the potential contributions of the anode sheath space charge is smaller than in the case of larger available flux. Under these conditions, the potential of the anode can increase relative to the sheath edge potential leading to anode fall growth. Under these conditions, it is postulated that anode fall growth will occur with increasing transverse magnetic field.

These physical concepts can be quantified by incorporating them into a numerical model. The following sections describes such a model. The qualitative features describing the physics of the model along with relevant equations are discussed first. Following this section is a discussion of the algorithm and numerical techniques utilized in the model. Next, general results extracted from the model are described. In addition, a comparison between the model and experiment is made. Finally, the implications of the model along with suggestions for further model development are elaborated upon.

6.2. Description of Anode Model

The approach taken in developing a model of the evolution of the anode fall voltage as a function of transverse magnetic field is based on solving Poisson's equation in which one boundary condition, the potential of the anode, is allowed to vary in response to the changes in the space charge distribution in the anode sheath. The model is cylindrically symmetric and one dimensional. Figure 6.1 depicts physical processes included in the anode sheath model. Because the anode is an electron collecting body, in general an

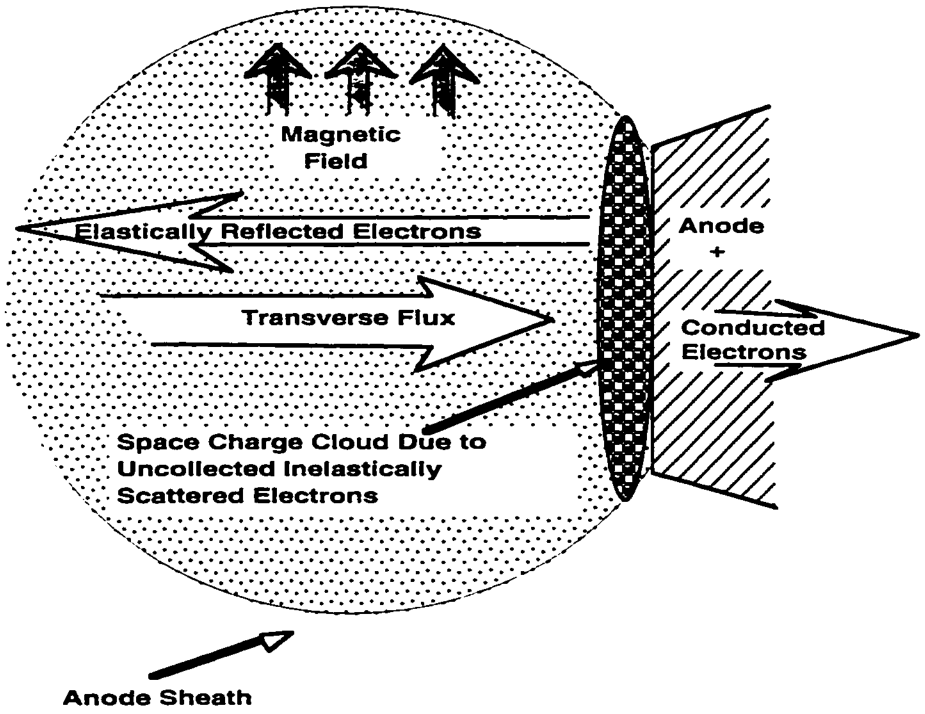

Figure 6.1 Schematic of Physical Processes taken into Account in the Anode Fall Model.

electron density gradient will exist between the anode and the plasma. Self-consistent with this density gradient is an associated potential distribution. For the case of an electron collecting electrode, the potential gradient is in many cases positive (i.e., electron attracting). This potential gradient, which extends on the order of a few Debye lengths is known as the anode fall voltage. The actual magnitude of this fall voltage depends on the space charge distribution in the anode sheath. The space charge distribution in the sheath is determined by the available electron flux incident on the sheath edge.

In the presence of a transverse magnetic field, the transverse electron flux is severely limited. This reduction is due in part to the reduction in the transverse diffusion coefficient. Classically the ratio of the transverse diffusion coefficient to the diffusion coefficient in the unmagnetized case is described by the classical relation: $\frac{D_{\perp}}{D} = \frac{1}{[1+\frac{\omega_{ce}^2}{\nu_c^2}]}$.

so that at large transverse magnetic fields, $\frac{\omega_{ce}^2}{\nu_c^2} >> 1$ so that $D_{\perp} << D$. The available transverse current to a planar probe as a function of transverse magnetic field is calculated using the relation derived by Sugawara:[1]

$$I_{e\perp} = \frac{1}{4} \cdot e n_o \bar{v}_e A \cdot [\frac{16}{3} \cdot \frac{\lambda_e \alpha^{\frac{1}{2}}}{K(k) \cdot r_o}] \cdot \frac{1}{1 + \frac{16}{3} \cdot \frac{\lambda_e \alpha^{\frac{1}{2}}}{K(k) \cdot r_o}} . \qquad (6.1)$$

At a fixed transverse magnetic field strength, the available current varies roughly linearly with electron number density. In this respect, the magnitude of the electron number density plays an indirect but important role in determining anode sheath potential behavior.

The potential distribution is calculated by solving Poisson's equation point by point from the sheath edge to the anode. The ion density profile is assumed to follow a Boltzmann distribution:

$$n_i = n_o \exp\left[\frac{-e\phi}{kT_i}\right]. \tag{6.2}$$

The contribution to the anode sheath density profile due to the input flux is obtained by invoking the conservation of electron flux:

$$n_e = \frac{\Gamma_e}{\sqrt{v_t^2 + \frac{2e\phi}{m}}}. \tag{6.3}$$

Here, n_i is the ion density, n_o is the background plasma density at the sheath edge, ϕ is the potential of the plasma, T_i is the ion temperature, n_e is the electron number density, Γ_e is the transverse available electron flux, v_t is the electron thermal speed at the sheath edge, m is the mass of the electron, k is Boltzmann's constant, and e is the electron charge. A similar expression multiplied by the electron elastic reflection coefficient is used to describe the density contribution due to particle flux reflected at the anode surface. The elastic reflection coefficient is an energy dependent quantity that depends on electrode material type and scattering plane orientation.[2] Interestingly enough, the electron elastic reflection coefficient can have significant structure as the energy of the incident electron is varied. For example, electrons scattering off the tungsten (100) plane experience significant reflection at energies just below 20 eV due to a peak in the reflection coefficient in this energy range (see Figure 6.2). Here, roughly 40% of the incident electrons are reflected. Such large reflection coefficients suggest that anode fall voltages of order 20 V should not be consistent with conditions where the available current is on the order of the discharge current. This notion further suggests that the elastic reflection coefficient can play a significant role in determining what anode fall will develop under certain discharge conditions. Although the role that electrode material type can play in determining anode power deposition (see Equation 3.6) from a work function point of view has been studied[3], the effect of reflection phenomena in regards to this problem has not been investigated.

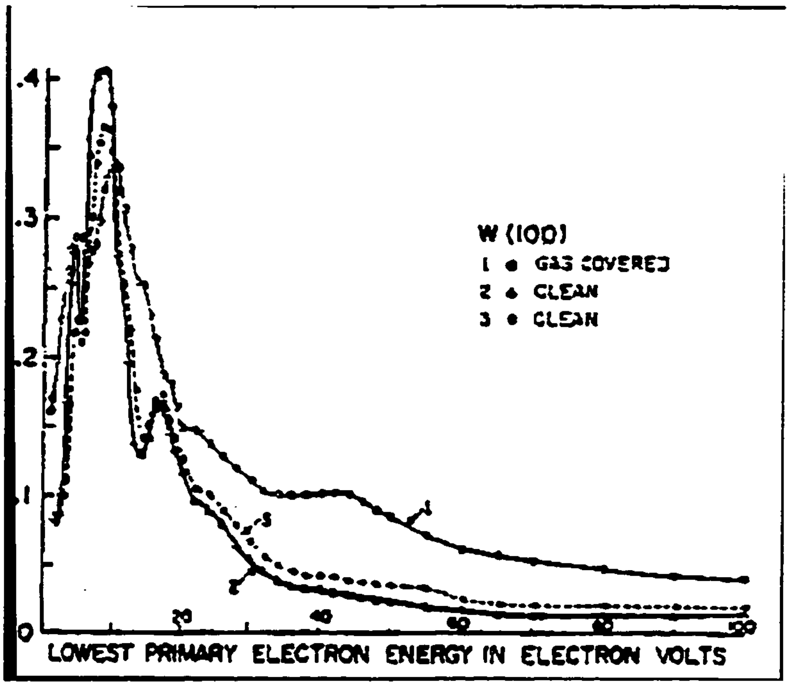

Figure 6.2. Variation in the Electron Elastic Scattering Coefficient with Incident Energy.[2]

The fraction of incident electrons that are not reflected or collected are assumed to scatter inelastically from the anode's surface. These electrons accommodate with the anode surface temperature and accumulate, forming a space charge layer at the anode's surface. With the discharge operating at constant current, this excess charge is not conducted away. This charge must be taken into account when solving Poisson's equation. The space charge layer assumes a steady-state value which is determined by the balance between the rate at which charge is lost due to recombination and diffusion and the replenishment rate due to incident electron flux. Because of the low ion density in the anode sheath, recombination losses are expected to be small. Diffusional losses along the magnetic field are the dominant mechanism for which charge in the surface charge layer is removed after inelastically scattering off the anode surface. The amount of charge in this surface charge layer is calculated by solving the first order differential equation:

$$\frac{dQ}{dt} = [J_{incident} - J_{reflected} - J_{discharge}] \cdot A - \eta \cdot Q. \tag{6.4}$$

Here η is the rate at which charge is lost along the magnetic field, $J_{incident}$ is the incident available electron current density, $J_{reflected}$ is the reflected electron current density, $J_{discharge}$ is the discharge current density, and A is the area of the anode. This rate, η, is related to the diffusional current along the magnetic field lines: $\Gamma_{\parallel} \cdot S$. Here $\Gamma_{\parallel}$ is the electron flux along the field lines and S is the effective area associated with the thickness of the space charge sheet adjacent to the anode through which radially diffusing electrons must pass. Taking these processes into account, Poisson's equation becomes:

$$\frac{d^2\phi}{dz^2} = \frac{1}{\varepsilon_o} \cdot \left[\left[\frac{en_o v_o}{v_o^2 + \frac{2e\phi}{m}} + \frac{e \cdot \Gamma_o \cdot f}{\sqrt{v_t^2 + \frac{2e}{m} \cdot [\phi - V_a]}} \right] - n_o e \cdot \exp\left[\frac{-e\phi}{kT_e} \right] + \delta(z) \cdot \sigma_s \right]. \tag{6.5}$$

Here, Γ_o is the electron flux at the sheath edge, f is the electron reflection coefficient, V_a is the anode fall voltage, v_o is the electron velocity at the sheath edge, σ_s is the surface charge associated with the anode space charge layer, and ε_o is the permittivity of free space. The sheath thickness is set at two Debye lengths, where the Debye length is defined from the boundary conditions. The potential of the anode over two Debye lengths decays to less than 15% of its surface value. The model solves Poisson's equation for the charge distribution determined by the flux equation taking into account the reflected current and surface charge effects over this thickness. The model then calculates changes in this space charge distribution brought on by changes in the input flux as the transverse magnetic field is varied. The effect of these changes on the anode's potential is then calculated. In this manner, the initial boundary condition at the anode changes relative to the potential at the sheath edge. The potential at the sheath edge is held fixed at $\phi = 0$ as a consequence of Debye shielding.[4]

6.3. Anode Model Algorithm

The general flow of the model is illustrated in the flowchart shown in Figure 6.3. The actual code is listed in Appendix A. The program starts by setting boundary conditions at the sheath edge and at the anode. In addition, plasma parameters such as background plasma density and average electron energy are initialized. Given the discharge current, the program then calculates the magnetic field associated with the condition that the incident available transverse current minus the reflected current equals the discharge current. Under these conditions, the anode fall voltage is expected to be at its maximum value. The magnetic field is then set to this value. Next, Poisson's equation is solved for the initial boundary conditions. The magnetic field is then decremented. This change increases the transverse electron flux which in turn influences the space charge distribution throughout the anode sheath. This change in anode sheath space charge is calculated using the earlier potential distribution along with the new transverse current. The potential contribution at the anode due to the change in anode sheath space charge is added to the anode's potential to calculate the anode fall voltage. Next, the program checks the anode fall to determine if it is less than zero. If this is the case, the program terminates, otherwise it loops back to the Poisson's equation solver and repeats the steps listed above using the new anode boundary condition. Program output includes the available current at the sheath's edge, the sheath's particle density and potential distribution, and the anode fall voltage all as a function of transverse magnetic field strength.

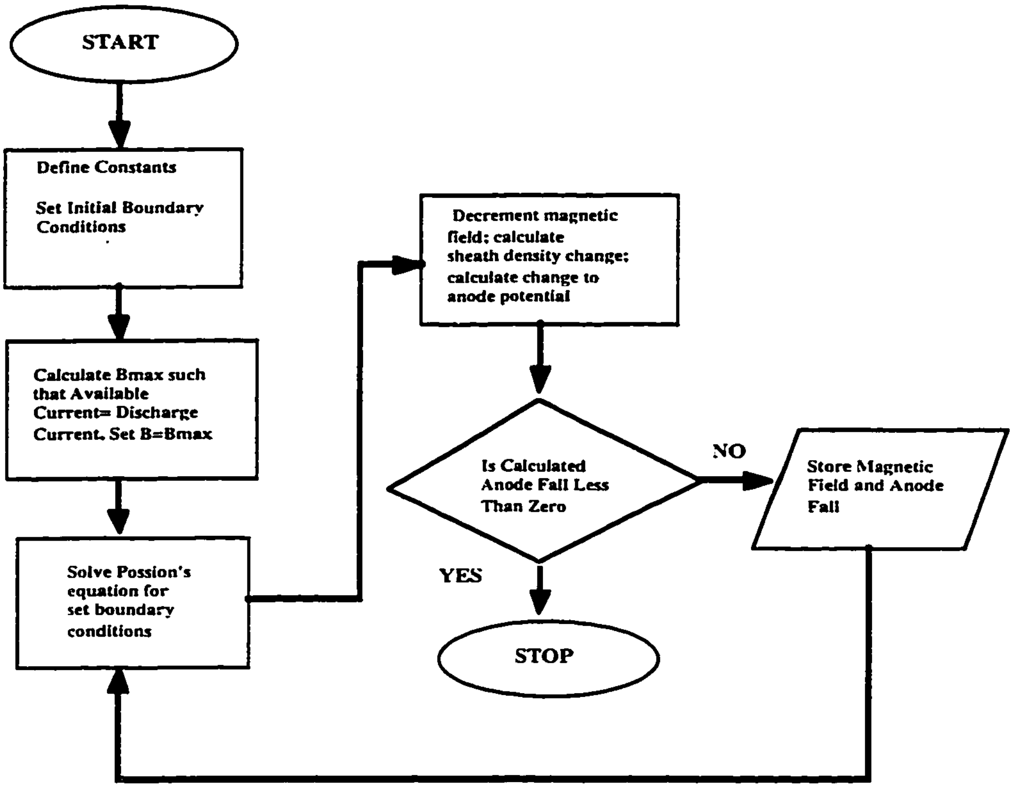

Figure 6.3. Anode Sheath Potential Model Flowchart.

6.4. Numerical Methods

By utilizing standard numerical techniques, the transition from the flowchart to the actual code is for the most part straightforward. Numerical techniques utilized in solving Poisson's equation and the calculation of the changes to the potential of the anode due to additional space charge, however, are worth mentioning due to the large part that they play in the program flow. Poisson's equation is solved using the nonlinear shooting method. In this approach, the second order differential equation with the boundary conditions $y(a) = c$ and $y(b) = d$ is broken up into two first order initial value equations:

$$y'' = f(x,y,y') \Rightarrow u' = f(x,y,y'), \quad y' = u \qquad (6.6)$$

along with the boundary conditions: $y(a) = c \quad y'(a) = t$, where $y'(a)$ is the shooting slope. This initial slope, $y'(a)$, is used to provide an additional boundary condition for one of the first order differential equations. The problem then becomes solving the two initial value equations. This task is achieved by the use of the fourth order Runge-Kutta technique. The trial solution of $y(b)$ using an estimated $y'(a)$ is compared to the true boundary condition at b. If the solutions are not within the specified tolerance (1% in this model's case), then the program calculates a better $y'(a)$ using Newton's method to solve the root of the equation: $y(b,t) - y(b) = 0$. This new value of t is then used in the routine to calculate a better solution for y.[5]

Calculation of changes in the potential of the anode due to changes in space charge is another important facet of the code. The anode sheath is partitioned with each grid point spaced by Δ (See Figure 6.4). Centered on these grid points are planes of finite thickness Δ and area A (anode surface area). This approach has been implemented in plasma simulation calculations.[6] Associated with each such slice is a charge density, ρ, and space charge $\rho \cdot A \cdot \Delta$. When the space charge profile is modified due to variations in the available current brought on by a reduction in the transverse magnetic field, the change in density at each slice is calculated at each grid point. The potential at the anode due to each such plane or disk of small but finite thickness Δ is evaluated by assuming each disk to be virtually a sheet of charge with surface charge $\rho \cdot \Delta$. The potential, ϕ_s, at the point z along the axis of a disk of surface charge σ is:[7]

$$\phi_s = \frac{\sigma}{2\varepsilon_o} \cdot \left[\sqrt{R^2 + z^2} - |z|\right]. \qquad (6.7)$$

Here R is the anode's radius and z is the axial position along the axis of a space charge layer. In the model, σ represents the change in surface charge on a "sheet" due ultimately to changes in the transverse magnetic field. ϕ_s is then evaluated at the anode for each "sheet." These potential contributions from each layer are summed and added to the anode's potential to calculate the new anode potential.

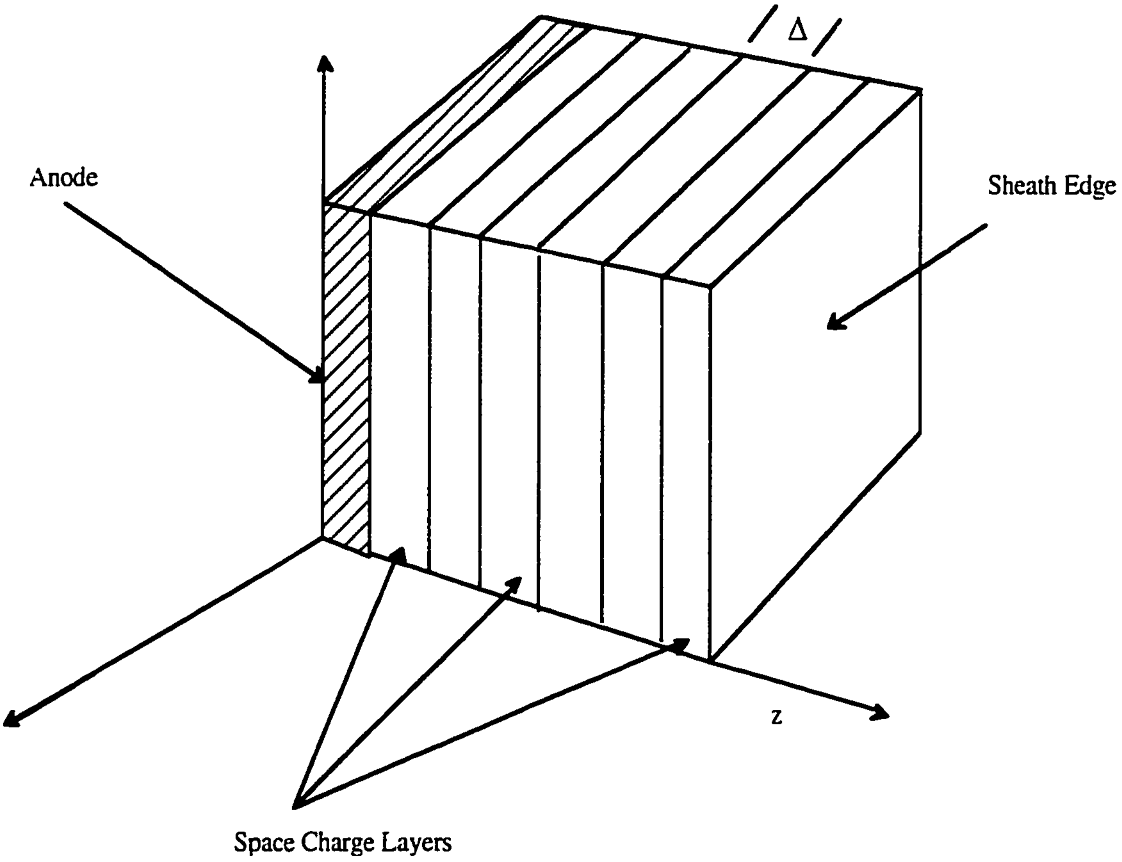

Figure 6.4 Schematic of Anode Sheath as Modeled in Simulation.

6.5. Model Results

6.5.1. General Findings and Results

The variations in the anode fall and available current as a function of transverse magnetic field was calculated by the anode fall model at a number of different plasma densities but at fixed electron temperature. For these cases the effective electron temperature along the discharge axis was set at 7 eV while the discharge current was set at 5 A. The 7 eV value is consistent with calculated effective electron temperatures obtained by integrating measured electron energy distribution functions. It should also be pointed out that this value is sufficiently large to sustain the prescribed discharge current at expected magnetic field strengths despite the relative smallness of the transverse diffusion coefficient at such field values. Figure 6.5 - 6.7 illustrate the predicted behavior in the normalized anode fall voltage and the ratio $\gamma = I_a / I_d$ versus transverse magnetic field strength. Here, I_a / I_d, is the ratio of the available transverse current to the discharge current. Anode fall voltage is normalized to the value that is associated with the condition where available current minus the reflected current equals the discharge current. The anode fall is maximum under these conditions. The fall value here, though arbitrary, is the starting point for the calculations.

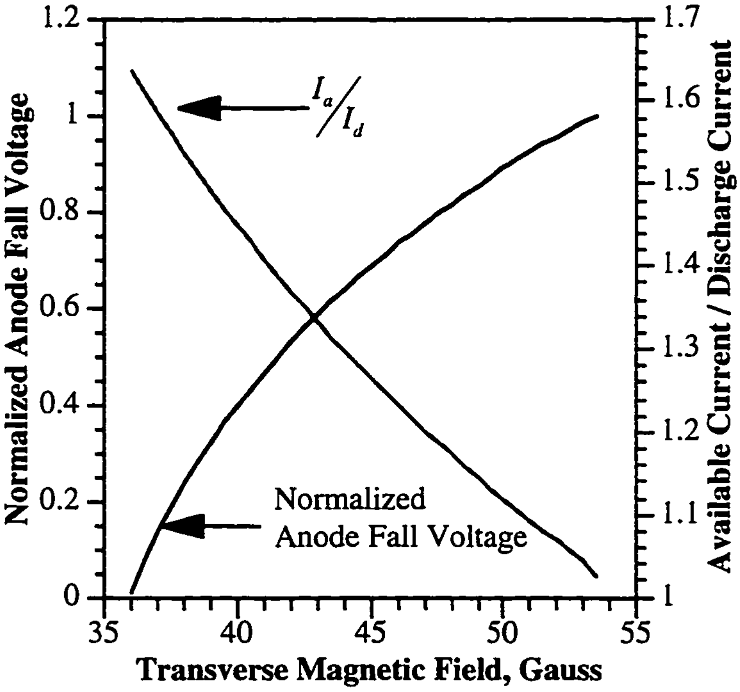

Figure 6.5. Variations in Anode Fall Voltage and Transverse Available Current with Transverse Magnetic Field with $n_e = 1 \cdot 10^{18}$ /m^3, $T_e = 7eV$.

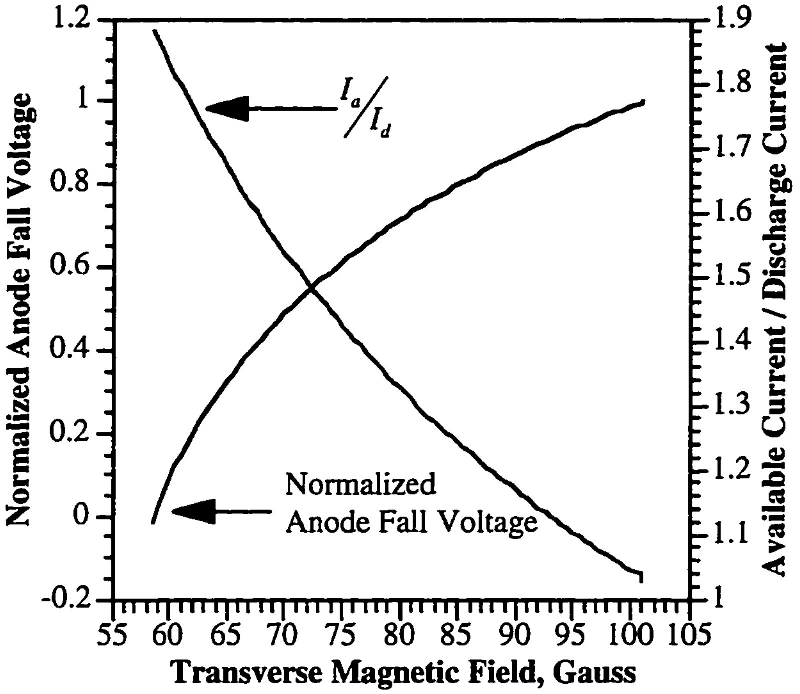

Figure 6.6. Variations in Anode Fall Voltage and Transverse Available Current with Transverse Magnetic Field with $n_e = 2 \cdot 10^{18}$ /m^3, $T_e = 7eV$.

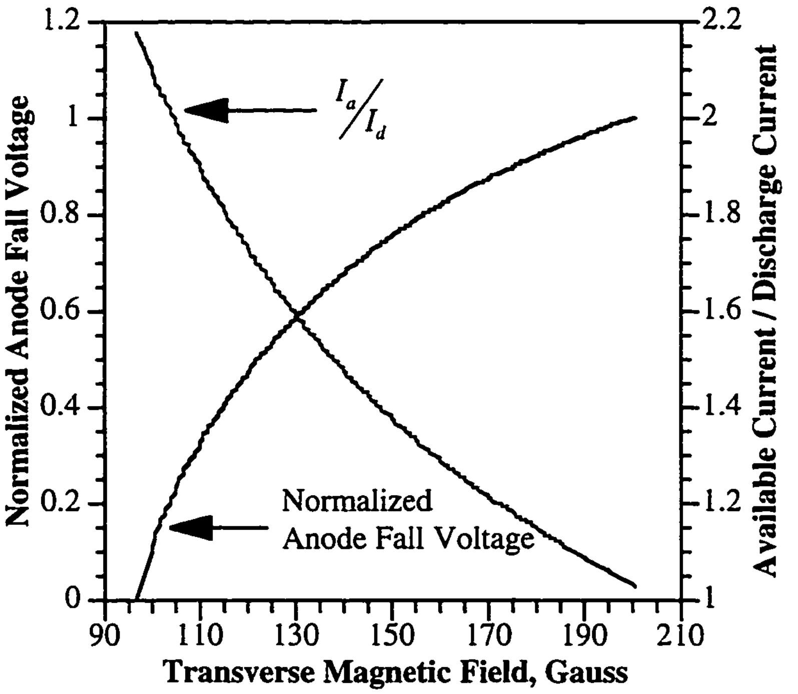

Figure 6.7. Variations in Anode Fall Voltage and Transverse Available Current with Transverse Magnetic Field with $n_e = 4 \cdot 10^{18}$ /m^3, $T_e = 7eV$.

One general feature preserved in all of these figures independent of electron number density is the behavior of the anode fall and γ with changes in the transverse magnetic field. As the transverse magnetic field increases, γ monatonically decreases while at the same time the anode fall voltage increases. This general behavior is postulated to be the basis of the anode fall variations with changes in the transverse magnetic field. Increases in the transverse magnetic field decreases the ratio γ. The decreases in γ gives rise to changes in the space charge distribution in the anode sheath. Furthermore, these changes in the space charge effect the potential profile along the anode sheath as calculated by Poisson's equation and as well as at the anode's surface. With this in mind, the general trends in the anode fall voltage and γ are expected.

The maximum magnetic field and magnetic field range between the maximum anode fall voltage and the zero of the anode fall voltage depends quite strongly on the local electron number density. Figures 6.5 through 6.7 show that in general, as the electron number density increases, the maximum magnetic field strength (associated with the condition where the corrected available current equals the discharge current) also increases. This is a direct consequence of a larger available current due to a larger background electron number density. In the cases presented here the maximum magnetic field increases linearly from 54 G at a density of $1 \cdot 10^{18}$ /m^3 to 101 G at $2 \cdot 10^{18}$ /m^3 to 200 G at $4 \cdot 10^{18}$ /m^3. The changes in the magnetic field range between the conditions where the anode fall is maximized and where the anode fall is zero also increase when electron number density increases. Here the range increases from 19 G case at the lowest density case to 43 G at the intermediate case to 105 G for the largest density case. This sensitivity to changes in the electron number density suggest that for a given transverse discharge device, the anode fall can be minimized at a given transverse magnetic field by increasing the local electron number density while maintaining at the same time a constant or increasing electron temperature. Indeed, this was found to be the case as observed in the auxiliary discharge study discussed in Chapter 5.

To summarize, the anode sheath potential model predicts that:

1. The anode fall voltage varies roughly inversely with γ at a fixed electron number density. This prediction is observed experimentally in both the characterization study and the auxiliary discharge study.
2. The anode fall voltage is controlled by γ which in turn is a strong function of the transverse magnetic field.
3. γ and thus the anode fall voltage are very sensitive to the changes in the local electron number density; this is a consequence of the fact that γ scales roughly linearly with electron number density. In this respect, it is ultimately the electron number density that controls γ and thus the anode fall voltage. This prediction is in accord with the measured nonlinear variations in the anode fall and electron density as the magnetic field increases (See Chapter 3).
4. The magnetic field range that a given transverse discharge can operate depends quite strongly on the electron number density.
5. The anode fall increases monatonically with increasing transverse magnetic field strength at a fixed electron number density. This prediction is also observed experimentally in the characterization study.

6.5.2. Comparison with Experiment

The anode model was compared with experimental data for a number of operating conditions. In general, the effect of the magnetic field is to alter plasma processes such that the electron density changes. As mentioned earlier, this is related to the influence of the transverse magnetic field on available flux and total ionization rate. In the case of the auxiliary discharge experiments of Chapter 5, the magnetic field was fixed while the electron number density varies under the influence of the auxiliary discharge. As the electron number density changes with variations in the auxiliary discharge so must the anode fall vary in response. Data from the auxiliary discharge experiments were compared with model predictions for similar changes in electron number density. At various input densities, the model calculates the anode fall at a fixed magnetic field and electron temperature. The anode fall was then normalized to the operating point where the anode fall is maximum. The experimental data was normalized to the anode fall voltage measured at a fixed auxiliary discharge current of 0.0 A. In most cases, for the 0.0 A auxiliary discharge current case, the anode fall voltage was maximized.

The comparison between experiment and model is illustrated in Figure 6.8 and 6.9. Again it should be pointed out that the model predicts these changes in both cases on density considerations alone. Figure 6.8 illustrates the comparison at a fixed transverse magnetic field of 38 G. The agreement between model and experiment appears to worsen as the auxiliary discharge current increases. The general trends in the behavior of the anode fall as predicted by the model, however, is still in reasonable agreement with experiment. Agreement between experiment and model for the 108 G case, illustrated in Figure 6.9, is much better than that of the 38 G case. Here the variations in the magnitude of the anode fall voltage with changing auxiliary discharge current as predicted by the model is consistent with those anode fall variations which were measured experimentally.

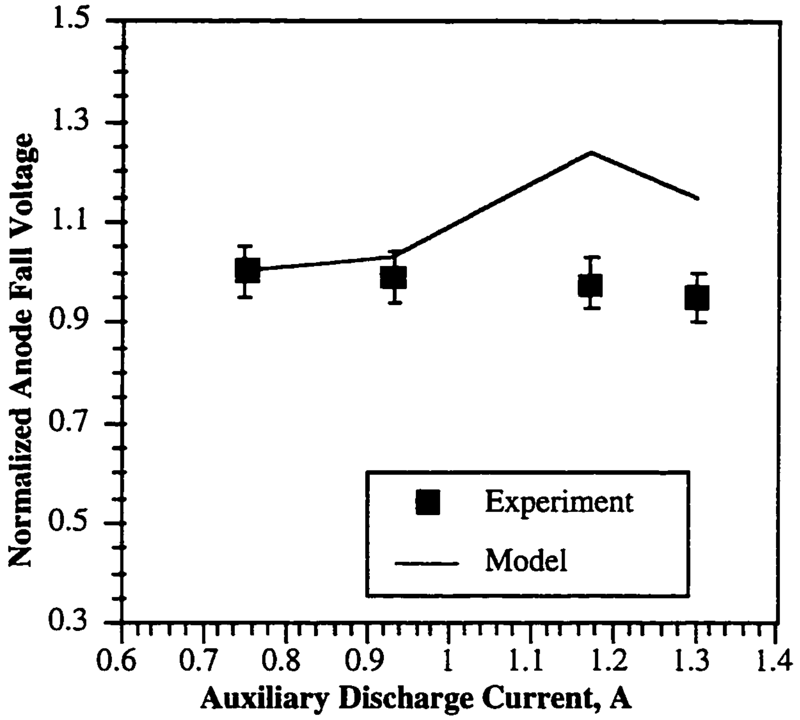

Figure 6.8. Comparison Between Experiment and Model: Transverse Magnetic Field=38 G.

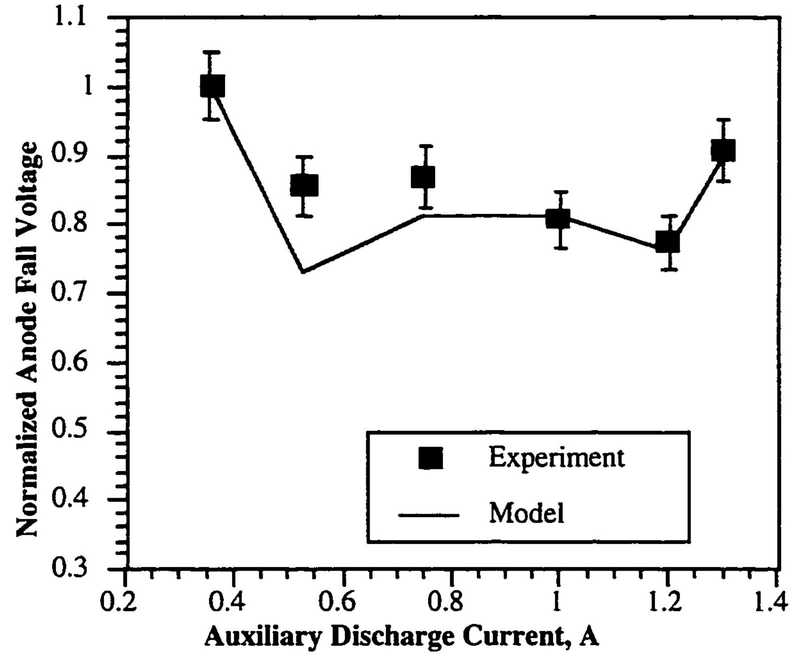

Figure 6.9. Comparison Between Experiment and Model: Transverse Magnetic Field=108 G.

One possible source of disagreement between model and experiment, particularly in the 38 G case, could possibly be related to differences between the functional dependence of the transverse diffusion coefficient used in the model and the actual dependence prevailing in experiment. The relation for the transverse available current used in the Sugawara relation assumes that the transverse diffusion coefficient can be described classically: $\frac{D_{\perp}}{D} = \frac{1}{[1+\frac{\omega_{ce}^2}{v_c^2}]}$. Experimentally, the nature of the diffusion coefficient has been investigated. Using the analysis of Chen[8] a rough estimate of the transverse diffusion coefficient can be obtained from the electron saturation current collected by a Langmuir probe of arbitrary shape. The approximate expression for the electron saturation current that follows the Chen analysis depends on the square root of the diffusion coefficient ratio:

$$I_{se} = \frac{4 \cdot n_o \cdot \bar{v} \cdot A_p}{3} \cdot \frac{\lambda}{a} \cdot \sqrt{\alpha}. \qquad (6.8)$$

Here, $\bar{v}$ is the electron thermal speed, a is the probe radius, and α is diffusion coefficient ratio. Upon finding the electron saturation current, α can be readily calculated.

The experimental diffusion coefficient was compared to the classical transverse diffusion coefficient for a plasma sustained by a 9 A discharge current. The comparison between the calculated classical transverse diffusion coefficient and that experimentally measured using Equation 6.7 is illustrated in Figure 6.10. From this Figure, the transverse diffusion coefficient does not appear to be classical. For a large transverse magnetic field range, the measured transverse diffusion coefficient is almost an order of magnitude larger than the classical transverse diffusion coefficient. The classical and experimental transverse diffusion coefficients, however, do appear to converge at larger transverse magnetic field strengths. The behavior of the classical and the experimentally determined transverse diffusion coefficient can in part be used to explain the relative agreement /disagreement between the model and experiment. At the low field regime, the disagreement between the diffusion coefficients is largest and thus agreement between model and experiment is expected to be the worst here. This reasoning is consistent with the discrepancies observed in the model comparison with experiment in the 38 G case. Because the experimental and classical diffusion coefficients appear to converge at large magnetic field strengths, the agreement between model and experiment should improve as the magnetic field increases. Again, this is consistent with that which is observed in the 108 G case where the agreement between model and experiment is quite good.

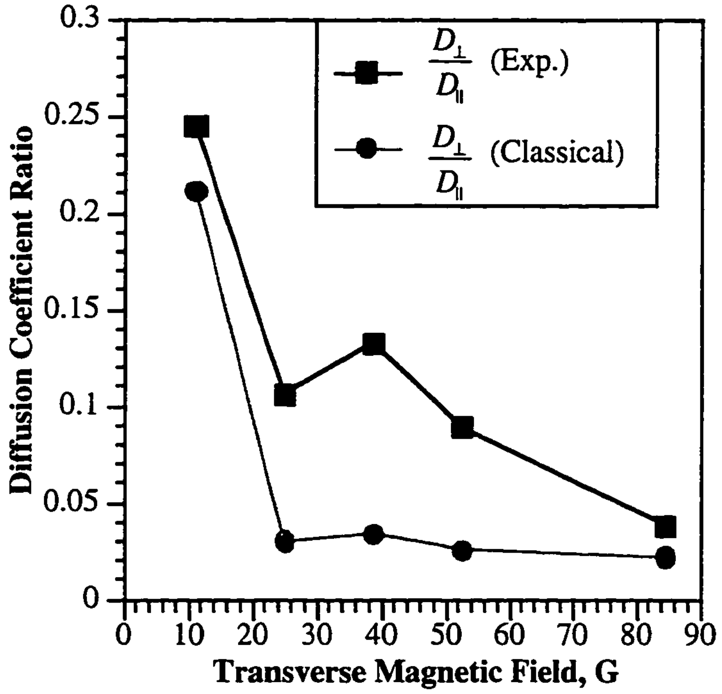

Figure 6.10 Classical and Experimental Transverse Diffusion Rates.

6.6. Conclusions

In summary, the anode model predicts anode fall behavior that is in accord with experimental findings. There were, however, some discrepancies. The identified discrepancies between experiment and model suggest possible future modifications.

Perhaps the greatest contributor of error lies in the uncertainty of the behavior of the available transverse electron current with changes in the transverse magnetic field. As discussed earlier, the transverse electron current relation derived by Sugawara assumes that transverse diffusion is classical. Experimental measurements on the other hand suggest that transverse diffusion is not strictly classical, especially in the limit of low magnetic field strength. A refinement would then be to incorporate a better model for the transverse electron current as a function of the transverse magnetic field. In the model, the ionization rate per electron is assumed to be constant and independent of magnetic field strength. Experiments indicate that the ionization rate is a function of the transverse magnetic field. In this respect, the local electron number density also depends on transverse magnetic field. A well developed model would include ionization as a function of transverse magnetic field. Despite its apparent deficiencies, the present model does predict the behavior of the anode fall in response to the magnetic field that is in accord with that which is measured experimentally. These predictions become better in the limit of large magnetic field.

Notes to Chapter 6

[1] M. Sugawara, The Physics of Fluids, Vol. 9, No. 4, 797 April (1966).

[2] I.H. Khan, J.P. Hoabson, and R.A. Armstrong, Physical Review, vol. 129, no. 4, 1513 (1963).

[3] G. Soulas and R. Myers, Proceedings of the 23rd International Electric Propulsion Conference, IEPC-93-194, (The Electric Rocket Society Press, Columbus, OH, 1993).

[4] Y.P. Raizer, Gas Discharge Physics (Springer-Verlag: New York, 1991), Chapter 8, Sec. 8.6, pp. 193-194.

[5] R.L. Burden, J. D. Faires, A.C. Reynolds, Numerical Analysis (Prindle, Weber,& Schmidt, Boston, 1978), Chapter 10, Section 10, pp. 469-476.

[6] C.K. Birdsall and A.B. Langdon, Plasma Physics via Computer Simulation (Adam Hilger, New York, 1991), Chapter 2, Section 2, pp. 8-10.

[7] M. H. Nayfeh and M.K. Brussel, Electricity and Magnetism (John Wiley Sons Inc., New York, 1985), Chapter 2, Sec. 2.7, pp. 52-53.

[8] R.H. Huddlestone and S.L. Leonard, Editors,Contributing author F. Chen, Plasma Diagnostic Techniques (Academic Press, New York, 1965), Chapter 4, Sec. 5, pp. 165-168.

CHAPTER 7

CONCLUSIONS AND SUGGESTED FUTURE WORK

7.1. Conclusions

This work entailed an investigation of the near-anode region of a low pressure argon arc under the influence of a transverse magnetic field. The significance of this work stems from the need to better understand the mechanisms behind the formation of large anode sheath potentials typically found in discharges with strong transverse magnetic fields. The interest in such phenomena comes largely from the electric propulsion community. In many cases, it is the sheath potentials at the electrodes which limit both engine life and thruster efficiency. The research presented here emerged from the need to understand the nature of such processes in MPD thrusters.

This investigation was essentially three-fold: 1.) Characterize the physics of the near-anode region under the influence of a transverse magnetic field. 2.) Using these findings, develop possible techniques to control the anode fall, and 3.) Using the experimental findings as a guide, develop a numerical model which contains the necessary physics to describe the behavior of the anode fall voltage as a function of the transverse magnetic field strength. Each aspect of this three tier approach yielded meaningful insight into the workings the near-anode plasma under the influence of a transverse magnetic field.

While characterizing the near-anode region it was found that under fairly isothermal conditions (constant electron temperature) it is the local electron density in the near-anode region that primarily dictates the behavior of the anode fall voltage. The variations in the electron number density is controlled by ionization processes that were shown to be influenced strongly by the transverse magnetic field. The relative importance of the electron number density stems from the fact that the available transverse flux is directly proportional to the electron number density. Indeed, the evolution of the anode fall voltage is a response to changes in electron number density and transverse current. The characterization study also indicated that the anode fall voltage dominates anode power deposition. This finding is consistent with anode power deposition studies conducted on actual MPD thrusters.[1]

Studies in the past have shown that significant field components parallel to the electron flux can reduce the anode fall voltage. The problem with such studies however is that the findings are usually convoluted with other possible effects which could plausibly reduce the anode fall voltage as well. Controlled experiments were undertaken to characterize the effect of an axial magnetic field at a fixed transverse magnetic field strength on the anode fall voltage. This study included an investigation into the effect of the magnetic field angle with respect to the anode surface on the anode fall voltage. It was found that at a fixed transverse magnetic field strength variations in the axial magnetic field strength and magnetic field angle had little effect on the anode fall voltage. The study suggested that it is the transverse magnetic field that dominates the behavior of the anode fall voltage.

The relationship between electron density and anode fall voltage determined from the characterization study motivated the implementation of an auxiliary discharge to modify plasma properties in the near-anode region. The auxiliary discharge proved to be quite useful in enhancing the local electron number density. These variations in electron number density and transverse electron current gave rise to expected changes in the anode fall voltage. In this respect, the findings from the characterization study were experimentally verified in a more controlled and deliberate manner. In addition, another possible means of reducing the anode fall voltage was uncovered. Possible means of implementing such a system on real electric propulsion systems were also discussed.

A numerical model was developed to predict the behavior of the anode fall voltage as a function of the transverse magnetic field strength. The ratio of the available current to the main discharge current, which is primarily determined by local electron number density and transverse magnetic field, proved to be an important model parameter in determining the behavior of the anode fall voltage. The magnitude of and ultimately the changes in the anode fall voltage are governed by the anode sheath space charge distribution which itself is determined by the ratio of available current to the discharge current. In addition, the importance of the elastic electron reflection coefficient was discussed in terms of its bearing on the measured anode fall voltage. In order to test its validity, the model was compared with experimental findings and was found to be in reasonable agreement. Agreement between model and experiment improved at higher magnetic fields strengths.

7.2. Suggested Future Work

Although many fundamental aspects regarding the behavior of the anode fall voltage and indeed the near-anode plasma under the influence of a transverse magnetic field have been discussed in this study, this thesis does suggest directions for future work. For example the evolution of the near-anode region under the influence of a transverse magnetic field could be studied by measuring the anode sheath electric field profile instead of measuring the total sheath potential difference. The large electric fields present in the anode sheath gives rise to the Stark mixing of electronic states in the discharge gas. This mixing gives rise to "forbidden" transitions. The intensity of the forbidden transition is related to the electric field strength.[2] This dependence can be determined numerically using the intensity of the "forbidden" line as an input. Because the use of Langmuir probes can give rise to possible local electron depletion effects thereby affecting the magnitude of the transverse available flux in the near-anode region, thus influencing the local sheath potential relative to the anode, this non-invasive spectroscopic technique is quite appealing. In addition, this non-invasive technique allows for spatially resolving the electric field variations in the anode sheath itself, something that is impossible with probes under these conditions. By integrating the calculated electric field over the sheath thickness, the anode fall voltage can be monitored as a function of transverse magnetic field strength. This technique was actually attempted in this study. Helium was used as the seed gas to make the measurements. The primary problem with this approach was related to poor resolution of the forbidden lines due to overlap with argon lines. Hence, this technique may be applicable to discharges of other working gases (e.g. helium or xenon).

In the auxiliary discharge experiment, it was found that the electron energy distribution function was not appreciably affected by the operation of the auxiliary discharge even though the electron number density was moderately changed. This finding suggests that the electron energy distribution function may not have been isotropic. Anisotropy in EEDFs has been measured for hollow cathode discharges.[3] In such a study, the second derivative of the current collected by a planar probe is measured at a number of different angular postitions. In order to shed light on the issue of anisotropy in the EEDF, it is suggested that the angular dependence of the EEDF be determined using similar techniques.

The anode model agrees fairly well with experimental results. The agreement improves with increasing magnetic field strength. As was stated earlier, this trend is attributed to the convergence of the true diffusion coefficient to the classical value in the limit of high magnetic field intensity. An enhancement of the anode model would entail adding a more realistic description of diffusion into the simulation to account for such discrepancies.

Notes to Chapter 7

[1] W. Schall, Proceedings of the AIAA 9th Electric Propulsion Conference, AIAA-72-502, (American Institute of Aeronautics and Astrounautics Press, Washington D.C., 1972).

[2] K. Takiyama, , T. Usui, Y. Kamiura, T. Fujita, T. Oda, and K. Kawasaki, Japanese Journal of Applied Physics, vol. 25, no. 6, L455, June (1986).

[3] S. Klagge and A. Lunk, J. Appl. Phys. 70 (1), 1, 99, July (1991).

APPENDICES

APPENDIX A

PROGRAM LISTING FOR THE ANODE SHEATH POTENTIAL MODEL

Listed below is the Fortran 77 computer code used to simulate the physical processes discussed in the anode sheath potential model as discussed in Chapter 6.

```
c John Edison Foster
c The anode fall model title: reflect.f
c The University of Michigan, Applied Physics

      Real VA,h,k,v0,me,nn,b,id,jflux,incre
    1       ,eo,nep(1000),ratek,Te,ld,Coull, Coll,ne,ocontr
     2        ,k11,k12,k21,k22,k31,k32,k41,k42,w1(1000),w2(1000),neg,
      3         x,TK,h,a,b,bc,bb,u1,u2,cc,ff,fyp,fy,kp11,kp12,kp21,kp22,
     4        kp31,kp32,kp41,kp42,u1(1000),u2(1000),Ti,rt,ypv,Zne,nes
     5       ,uvc,uvu,jold,pert(1000),refl,ppsig,cf,surf1,surf2,surf
    6      ,fract,vat,NEZ
      Integer n,ct,Pass,vari
     Character*18 output,distrib
      common v0,ne,jflux,Ti,id,fract,bc

c*****************Setting Constants**********************
c b=magnetic field, Tesla
c refl is the electron reflection coefficient at the anode
c it is a measure of how much of the uncollected incident electron flux is reflected
c pert refers to the density change in the gap due to a change in B Field.
c VA=anode fall voltage
        VA=64.00
c ppsig is the surface charge density at the surface immediately before a
c change in plasma conditions
        ppsig=0.0
        bc=VA
        ct=0
        surf=0
        Pass=0
        me=9.11e-31
c the surface charge is sigsur
c  id=discharge current
        sigsur=0.0
        eo=8.85e-12
        id=5.0
c n=number of 1-D grid spaces
        k=1.38e-23
        r0=1.27e-2
        e=1.6e-19
c r0 is the radius of the anode, Pr= pressure in mTorr, P=pressure in Pa
```

```
      c ******
            write(*,*) 'Input the background electron density in #/m^3'
            read*,ne
            neg=ne
            Te=7.0
      c  Enter the background pressure, Pr,  nn=neutral density  (MKS)
            print*, 'input background pressure'
            read*,Pr
            P=133.0*Pr
            Tg=300.0
            nn=P/(k*Tg)

      c Tg is gas temp, nn is gas density, v0=thermal speed, Ld=Debeye length
            v0=sqrt(8.0*1.38e-23*Te*11600.0/(3.14*9.11e-31))
            w1(0)=VA
      c when all charge is expelled, this value VA is potential of anode relative
      c to the sheath edge

      c********Introduction to the Program***********

            write(*,*) ' '
            write(*,*) ' '
            print*,'*******Anode Sheath Potential Calculator*******'
             write(*,*) ' '
            write(*,*) 'enter in the name of the anode fall output file'
            read*, output
            write(*,*) 'enter in the name of the potential distribution file'
            read*,distrib
      c   incre is the magnetic field increment or step, id=discharge current
            Open(UNIT=1,
FILE=output,ACCESS='SEQUENTIAL',FORM='FORMATTED',
         1      STATUS='NEW')
            Open(UNIT=2,
FILE=distrib,ACCESS='SEQUENTIAL',FORM='FORMATTED',
         1      STATUS='NEW')


      c********Calculating more parameters***************
      c note ld=Debye Length
        5   ld=sqrt(1.38e-23*Te*11600*eo/((1.6e-19)**2*ne))

      c h=grid spacing, sheath itself taken to be 2 Debye lengths long
         Pass=Pass+1
      c  Pass corresponds to the number of B field increments there are
      c Qen is the electron neutral collison cross section at 7 eV
      c Coull is the Lambda for the Coulomb Log, Coll is total electron coll freq
         Qen=9.4e-20
      c Qen interpolated from data in Kaufman's Broad Beam Sources
      c  Kaufman, Harold R., Operation of Broad-Beam Sources, Commonwealth
      c  Scientific Corporation, Alexandria, 1984.
            Coull=1.55e13*(Te)**1.5*1/Sqrt(ne)
            Coll=6.69e5*nn*Qen*Sqrt(Te)+1.94e-12*ne*log(Coull)*1/Sqrt(Te)
            Ti=.026
```

```
c************Setting up boundary conditions and grid parameters
c************for calculations


c n=number of 1-D grid spacing
c n is the number of divisions of the interval , ct=#of iterations
c a=begin point, bb end point of the interval
c w1 => y solution , w2=slope of y
c bc is the fixed boundary condition at w1(n)
c TK is the initial guess at the slope at a+n*h
c where h is the length of the segment

      a=0.0
      bb=2.0*ld
      w1(0)=bc
      h=-ld/300.0
      cc=(bb-a)/h
      n=-(cc)
      u1(n)=0.0
      u2(n)=1.0
      w1(n)=0
      TK=((bc-w1(n))/(a-bb))
      w2(n)=TK


c*******DETERMINATION OF THE MAX B FIELD***********

c  Determination of the Maximum magnetic field that can be supported
c   by the discharge for the specified discharge current, id
c  fract is the elastic electron reflection coefficient
         fract=reflec(bc+Te/3.14)
     If (Pass .EQ. 1) then
      nes=ne
        Do 7 yj=0,10000.0,.50
          rt=yj/10000.0
          Coullx=1.55e13*(Te)**1.5*1/Sqrt(nes)
          Collx=6.69e5*nn*Qen*Sqrt(Te)+1.94e-12*nes*log(Coullx)*1/Sqrt(Te)
           nes=flux(Collx,rt,r0,Te,ne)/v0
           ypv=e*flux(collx,rt,r0,Te,ne)*(3.14*r0**2)*(1-fract)

          print*, e*flux(collx,rt,r0,Te,ne)*(3.14*r0**2)*(1-fract),id

          If (ypv .LT. id) then
               b=rt-.50/10000.0
               incre=.5/10000

               write(1,*) b,VA,flux(Collx,b,r0,Te,ne)*e*3.14*r0**2,
   1           flux(Collx,b,r0,Te,ne)/v0

                print*,'b field max is',b,'  increment is',incre
               goto 8

          end if
```

```
   7  continue
          b=rt-.50/10000.0
          incre=.5/10000

           write(1,*) b,VA,flux(Collx,b,r0,Te,ne)*e*3.14*r0**2,
    1      flux(Collx,b,r0,Te,ne)/v0

      end if

c end to this block****************


C  calling the function to calculate the electron flux via relation of Sugawara


   8  fract=reflec(bc+Te)
     jflux=flux(coll,b,r0,Te,ne)
      hxc=flux(coll,b-incre,r0,Te,ne)

        If (e*jflux*(3.14*r0**2)*(1-fract) .LT. id) then
            Close(unit=1)
             print*,'not enough thermal current to support',id,'Amps'
            go to 100
        end if

c potential distribution solver...via the shooting method

   9  Do 10 j=n,1,-1
         If (j.eq. 1) then
           surf=sigsur/h
          else
           surf=0.0
     end if

     If (j .ne. 1)  then
         surf=0.0
      end if

     x=bb+(n-j)*h


c Calculation of 4th order Runge-Kutta Coef.
c note the calculation simply takes into account higher derivatives
c so that it is a viable numerical technique comparable to Taylor expansion
c techniques

         k11=h*w2(j)
         k12=h*ff(x,w1(j),w2(j),surf)
         k21=h*(w2(j)+.5*k12)
         k22=h*ff(x+h/2.0,w1(j)+k11/2.0,w2(j)+k12/2.0,surf)
         k31=h*(w2(j)+k22/2.0)
         k32=h*ff(x+h/2.0,w1(j)+k21/2.0,w2(j)+k22/2.0,surf)
         k41=h*(w2(j)+k32)
         k42=h*ff(x+h,w1(j)+k31,w2(j)+k32,surf)
```

```
c
        w1(j-1)=w1(j)+(k11+2.0*k21+2.0*k31+k41)/6.0
        w2(j-1)=w2(j)+(k12+2.0*k22+2.0*k32+k42)/6.0

c w1=> y(x), w2=>y'(x)


c next calculate functions related to the derivative
c so that the Newton-Ralson method can be used to obtain a better
c initial slope
        kp11=h*u2(j)
        kp12=h*(fy(x,w1(j),w2(j))*u1(j)+fyp(x,w1(j),w2(j))*u2(j))

        kp21=h*(u2(j)+.5*kp12)
        kp22=h*(fy(x+.5*h,w1(j),w2(j))*(u1(j)+.5*kp11)+
     1  fyp(x+.5*h,w1(j),w2(j))*(u2(j)+.5*kp21))
       kp31=h*(u2(j)+.5*kp22)
       kp32=h*(fy(x+.5*h,w1(j),w2(j))*(u1(j)+.5*kp21)+
     1  fyp(x+.5*h,w1(j),w2(j))*(u2(j)+.5*k22))
       kp41=h*(u2(j)+kp32)
       kp42=h*(fy(x+h,w1(j),w2(j))*(u1(j)+kp31)+
     1  fyp(x+h,w1(j),w2(j))*(u2(j)+kp32))


       u1(j-1)=u1(j)+1.0/6.0*(kp11+2.0*kp21+2.0*kp31+kp41)
       u2(j-1)=u2(j)+1.0/6.0*(kp12+2.0*kp22+2.0*kp32+kp42)

  10   continue

c    Check tolerance
        If (sqrt(((w1(0)-bc))**2)/bc .LT. .01) then
          print*,'within 1% tolerance*****'
          print*,ct,'iterations for solution'

          do 15 j=n,0,-1
             write(*,*) bb+(n-j)*h,w1(j),w2(j)

  15      continue
          goto 23
        end if


       ct=ct+1
        print*,tk, '   modified ',(w1(0)-bc)/u1(0), 'reflect',fract
        print*,'ct and tolerence ',ct,(w1(0)-bc)/bc,w1(0),bc,h

       If (ct .GE. 100) then
          print*,'exceeded 100 iterations...had to terminate'
           print*,'tolerence',sqrt(((w1(0)-bc))**2),ct,' counts'

        goto 23
       end if

c note the additional else statements
```

```
c the purpose of these is to prevent the program from
c switching the polarity of the the slope for small
c anode potentials

                print*,'initial tk value',tk
                uvu=(tk-(w1(0)-bc)/u1(0))
                uvc=tk

          if (((tk-(w1(0)-bc)/u1(0))/TK .LT. 0)) then
                  w2(n)=-uvu*.5
                 u1(n)=0.0
                 u2(n)=1.0

                 print*,' safety net',uvu
                 read*,mim
                 goto 9

            end if
c    ********************************

        TK=TK-((w1(0)-bc))/u1(0)

            print*,'ratio', TK/(TK-((w1(0)-bc))/u1(0)), tk
            print*,w1(0),bc, 'w1(0) and bc'


       w2(n)=TK

                u1(n)=0.0
                 u2(n)=1.0
       go to 9


c stepping the magnetic field
  23    b=b-incre

       if (b .LT. 0.0) then
         goto 100
       end if
      ct=0
c calculating the reflection coefficient
        fract=Reflec(bc+Te)
         print*,'reflection',fract,bc


c calculation of new density profile due to change in B using
c the earlier potential distribution and then calculating the
c series of charge sheets contribution to the potential of the anode
c relative to the sheath edge whose potential value is pegged  at zero
c
c calculation of an appropriate electron density
  25    Zne=ne
         jold=jflux
```

```
c

        jflux=flux(coll,b,r0,Te,ne)
        print*,'main calculator B and flux diff.',b,jflux*r0**2*3.14*1.6e-19-id

c*****************************************************
c******determining the fate of uncollected inelastically scattered
c electrons at the anode surface
c  note density at the sheet closest to the anode is calculated
c here the surface charge term is not included
c  this calculation is used to obtain what is the loss rate at anode by
c diffusion along the field lines
      NEZ=-e*jflux/Sqrt(v0**2+2*e*w1(1)/9.11e-31)
     1 +((jflux*fract
     2  ))*(-1.6e-19)/sqrt(vat**2+2*1.6e-19/9.11e-31*
     3  bc)
c calculation of the loss rate constant ratek for electrons at surface
       ratek=(-h)*(2*r0)*2*Sqrt(.333)*Sqrt(8*1.38e-23*300/(9.11e-31*
     1  3.14))*NEZ/(-e)
c******************************************************


c  calcuation of anode surface charge contribution to anode potential
        sigsur=((jflux*e*(3.14*r0**2)*(1-fract)-id)
     1     /(ratek*(3.14*(r0)**2)))*r0
        print*,'Surface charge',sigsur
        write(*,*) 'rate const**', ratek
c this following line adds the accumulated surface charge
c to the flux contribution of density

        vat=sqrt(v0**2+2*1.6e-19*bc/9.11e-31)
        Do 40 J=1,n
        If (j.eq.1) then
           surf1=sigsur
           surf2=psig
       Else
           surf1=0.0
           surf2=0.0
        End If

c NEP is the new charge distribution due to the density change via B

      NEP(J)=-e*jflux/Sqrt(v0**2+2*e*w1(J)/9.11e-31)
     1 +e*jflux/v0*Exp(-e*w1(J)/(k*Ti))+surf1/h+((jflux*fract))
     2  *(-1.6e-19)/sqrt(vat**2+2*1.6e-19/9.11e-31*
     3  bc)


      pert(J)=NEP(J)-(-e*jold/Sqrt(v0**2+2*e*w1(J)/9.11e-31)+
     1 e*jold/v0*Exp(-e*w1(J)/(k*Ti))+surf2/h+((jold*fract))
     2  *(-1.6e-19)/sqrt(vat**2+2*1.6e-19/9.11e-31*
     3  bc))
c
c*****this part of the program actually writes potential
```

```
c*****distribution  to a file...a big memory drain so
c****it its turned off here
c      write(2,*),a+(-j)*h,w1(j),
c    1 (-e*jold/Sqrt(v0**2+2*e*w1(J)/9.11e-31)+
c    2 e*jold/v0*Exp(-e*w1(J)/(k*Ti))+surf2/h+((jold*fract))
c    3  *(-1.6e-19)/sqrt(vat**2+2*1.6e-19/9.11e-31*
c    4  bc))*1/e
c pert is the difference point by point between density after the magnetic
c field changed and the one before the B field changed
c it is the perturbation to the density due to the B field change

c  calculation of the sheet of charge contribution to the anode potential.
        ocontr=ocontr+(-1*h)*pert(J)/(2*eo)*(Sqrt(r0**2+(J*h)**2)-
     1  Sqrt((J*h)**2))


  40  Continue


c       Diagnostic print statements  (optional)
        print*,ocontr,' pot due to charge distribut'

        print*,'ion contribut to pot.',e*ne*Exp(-e*w1(J)/(k*Ti))

c adding total sheet contrib to the surface charge contrib
        print*,'potent  ',ocontr,sigsur*r0/(2*eo)
c      print*,((jflux*e*(3.14*r0**2)-.05)/
c    1  (ratek*(3.14*(r0)**2)))*r0

c note ppsig is subtracted away from sigsur...
c this is in line with the fact that its the change in surface
c charge that gives rise to the change in anode potential
c not the absolute magnitude
c because sigsur is the absolute magnitude of the surface charge after
c the b field change

        bc=bc+ocontr

c writing the magnetic field and the potential difference

        write(1,*) b,bc-w1(n),jflux*e*(3.14*r0**2),jflux/v0
        ocontr=0.0
        write(*,*) bc-w1(n)
        if (bc-w1(n) .LE. 0.0) then
           goto 100
        end if
        neg=jflux/v0
        ppsig=sigsur

        go to 5


 50     Format(1x,f10.4,f10.4,f10.4,f10.4)
 100    close(unit=1)
```

```
      close(unit=2)
      Stop
        End
c
c *******************Function Section*******************
c

c   ==Flux Calculator....ref. Sugawara, Phys of Plasma,Vol. 9, 1966.==
c                              =========
c this function calculates the available electron flux at the sheath edge
        Real Function flux(a1,a2,a3,a4,a5)
c a1= electron tot. coll. freq., a2=magnetic field (transverse)
c a3= probe radius, a4=electron temp, eV, a5=electron density
c

        Real  a1,a2,a3,a4,a5,k,m,mfp,alp,cyclo,lk,bk,nc,mc,ei,aa,flx
        k=1.38e-23
        m=9.11e-31
        bk=0.0
        mc=1.0
        nc=1.0
        vt=sqrt(8.0*k*a4*11600.0/(3.14*m))
        aa=1.27e-2
        mfp=vt/a1
        cyclo=(a2*1.6e-19/m)
        alp=1.0/(1.0+(cyclo/a1)**2)
        lk=Sqrt(1-alp)
c calculation of the Complete Elliptic Integral using first 10 terms
        Do 45 j=1,10
              mc=mc*((1.0+(j-1.0)*2.0)/(2.0+(j-1.0)*2.0))
              nc=nc*lk**2
              bk=bk+mc*nc
  45    Continue
c EI is the complete elliptic integral, flx is the flux

        EI=3.14/2*(1+bk)
        flx=.25*a5*vt*(16.0/3.0*mfp*Sqrt(alp)/(EI*AA))*
   1  (1+16/3*(mfp*Sqrt(alp)/(EI*AA)))**-1
         flux=flx

      Return
      End
c____________________________________________________________

c this function block calculates  f(x,y,y')

        Real Function ff(xx,yy,zz,sey)
        real xx,yy,zz,g,aa,bx,cc,dd,sey,area,vata,ee,frac,bcc
c aa=V0,bx=ne,cc=jflux,dd=Ti,sey=surface charge
        common aa,bx,cc,dd,ee,frac,bcc
c frac =electron reflection coef., ee=discharge current, bcc=anode potential
c       if (aa**2+2*1.6e-19/9.11e-31*yy) .LE. 0 then
          area=3.14*(1.27e-2)**2
          vata=sqrt(aa**2+2*1.6e-19*bcc/9.11e-31)
```

```
c vata is the electron speed at the anode
        g=(1.6e-19/8.85e-12*cc/sqrt((aa**2+2*1.6e-19/9.11e-31*yy)))
    1 -1.6e-19/8.85e-12*cc/aa*
    2  exp(-1.6e-19*yy/(1.38e-23*dd*11600.0))-sey/8.85e-12+
    3  1.6e-19/8.85e-12*(cc*frac)/
    4  sqrt(vata**2+2*1.6e-19/9.11e-31*(yy-bc))
        ff=g


        return
        end

c this function is fy ....derivative of f w.r.t. y
      Real Function fy(aa,oo,uu)
       Real aa,oo,uu,gg,av,bv,cv,dv,ev,fra,bcd,area
c av=V0,bv=ne,cv=jflux,dv=Ti
        common av,bv,cv,dv,ev,fra,bcd
        vata=sqrt(av**2+2*1.6e-19*bcd/9.11e-31)
        area=3.14*1.27e-2**2
     gg=(-(1.6e-19)**2/(9.11e-31*8.85e-12)*cv/
    1  (av**2+2*1.6e-19*oo/9.11e-31)**1.5)
    2  +(1.6e-19)**2*(cv/av)/8.85e-12*exp(-1.6e-19*oo/
    3   (1.38e-23*dv*11600))/
    4  (1.38e-23*11600*dv)-1.6e-19**2/8.85e-12*
    5   (cv*fra)/
    6  ((vata**2+2*1.6e-19/9.11e-31*(oo-bcd))**1.5*9.11e-31)
       fy=gg

      return
      end
c this function calculates the derivative of f w.r.t. y'
        Real Function fyp(rr,ss,tt)
        Real rr,ss,tt,yu,avt,bvt,cvt,dvt
c av=V0,bv=ne,cv=jflux,dv=Ti
        common avt,bvt,cvt,dvt
        yu=0.0
        fyp=yu
        return
        end


c********reflection coefficient using Khan et al Phys Rev vol 129 1963
c*****here single crystal tungsten is the electrode material type
     real Function Reflec(en)
     Real en,io4
c  io4 = curve fit to reflection coefficient for W(100)
        If ((en .LE. 8) .and. (en .gt. 0)) then
            io4=-2.4644e-3+4.3383e-2*en
        end if
        If ((en .GE. 8) .and. (en .LT. 15)) then
            io4=.73544-4.2190e-2*en
        end if
        If ((en .GE. 15) .and. (en .LT. 17)) then
            io4=-8.4463e-2+1.5433e-2*en
```

```
        end if
        If ((en .GE. 17) .and. (en .LT. 100)) then
             io4=.65674-4.8487e-2*en+1.5266e-3*en**2-2.3958e-5*en**3
     1          +1.8399e-7*en**4-5.4967e-10*en**5
        end if
        If ((en .LT. 0.0) .OR. (en .GT. 100)) then
            io4=0
        end if
       If (io4 .LT. 0) then
             io4=0
        end if
c taking average
      Reflec=(io4)
      return
      end
```

APPENDIX B

SPATIAL CHARACTERISTICS OF THE NEAR-ANODE PLASMA UNDER THE INFLUENCE OF A TRANSVERSE MAGNETIC FIELD

B.1. Introduction

The spatial uniformity of the plasma in the near-anode region under the influence of a transverse magnetic field was accessed using a cylindrical Langmuir probe and emission spectroscopy. The argon plasma investigated was sustained by a 8.5 A argon arc at 50 mTorr. The purpose of the characterization was to determine the effect of the transverse magnetic field on spatial variations in plasma potential, local electron number density, and electron temperature. The spatial measurements were made by displacing the entire discharge relative to the fixed Langmuir probe and optical imaging axis. The discharge apparatus is shown again in Figure B.1. The near-anode region investigated extended as far as 8 mm downstream of the anode surface (cathode - anode gap was 60 mm). In general, over the spatial positions studied here with the electrostatic probes no significant potential gradients are expected because the closest probing distance relative to the anode is several orders of magnitude larger than the Debye length. In order to ascertain plasma processes very near the anode surface, emission spectroscopy is used to map out features over length scales much smaller than the 0.2 mm diameter Langmuir probe.

B.2. Spatial Langmuir Probe Data

Spatial Langmuir probe measurements were taken by translating the entire discharge in step increments of 1 mm relative to a probe fixed with respect to the anode. Figure B.2 shows the variation in the plasma potential measured downstream of the anode at various magnetic field strengths: 9 G, 35 G and 55 G. In general, the plasma potential profile downstream of the anode was slowly varying with position, not showing much spatial structure. These relatively flat profiles are consistent with the expected behavior of the plasma potential in the positive column.[1] Most of the potential drop at the anode is confined to such a small volume that Debye shielding is fairly complete at distances exceeding 1 mm downstream of the anode. It is worth noting, however, the presence of a presheath extending several millimeters downstream of the anode is possible. A slight drop in the plasma potential of order 1 V was observed in the higher field cases (35 G and 55 G) occurring between 1 and 4 mm above the anode's surface. The formation of such a presheath may be necessary in order to offset reductions in transverse flux by increasing the mobility term of the electron flux. In addition, it is also worth noting that as expected the average value of the plasma potential on these relatively flat profiles increases with increasing magnetic field rising from approximately 31 V at 9 G to roughly 40 V at 55 G.

As illustrated in Figure B.3, the electron number density also varied little with position at fixed transverse magnetic field strength. The spatial structure in the electron number density profile, however, does appear to increase with increasing magnetic field strength. These spatial variations in the electron number density did not exceed 40%, which is actually below the expected error associated with such measurements.

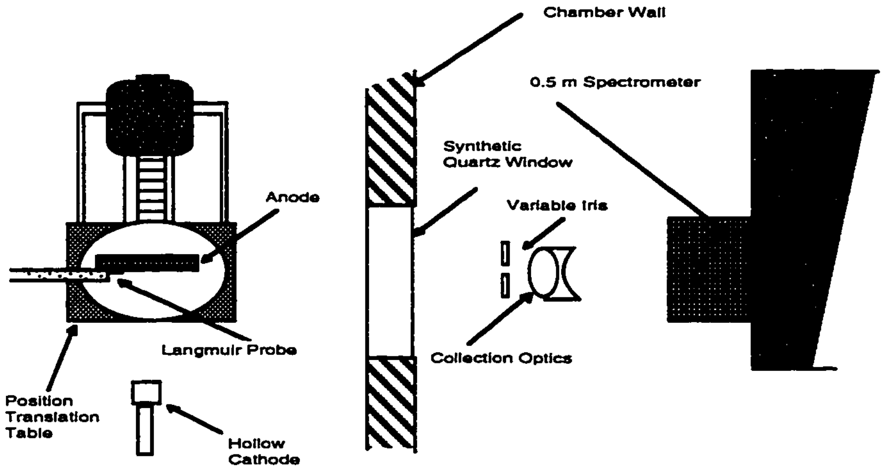

Figure B.1. Discharge Set-up for Spatial Measurements.

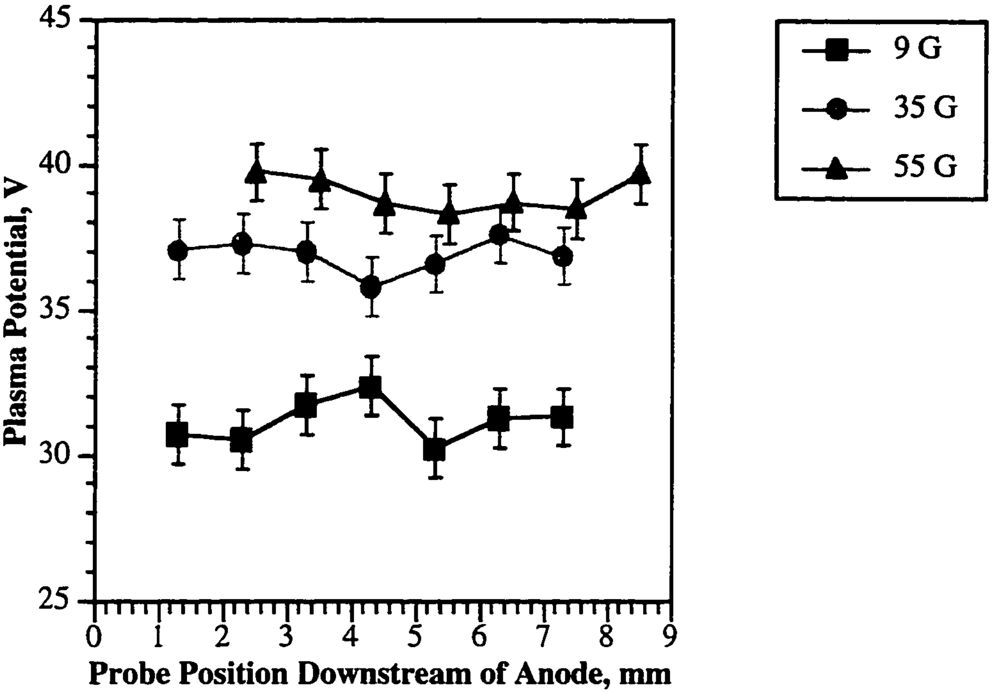

Figure B.2. Potential Variation in the Near-Anode Plasma Region.

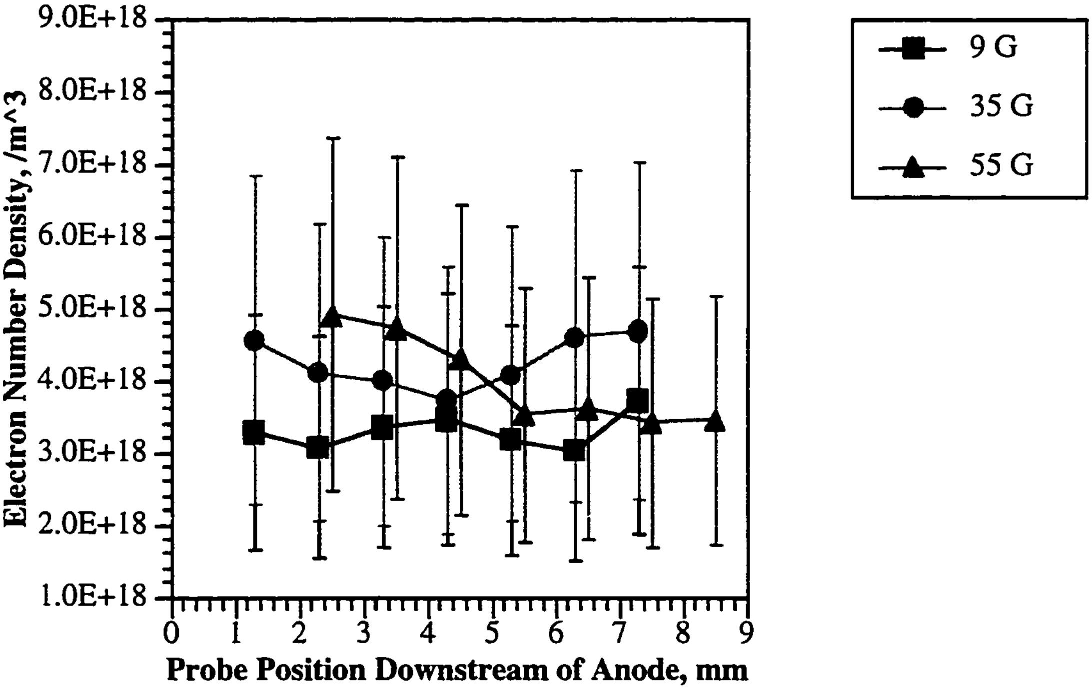

Figure B.3. Electron Density Variation in the Near-Anode Region.

Spatial variations in electron temperature at various magnetic field strengths is illustrated in Figure B.4. Here the variations in the electron temperature are also small over the 6 mm section of near-anode region investigated not exceeding 0.5 eV.

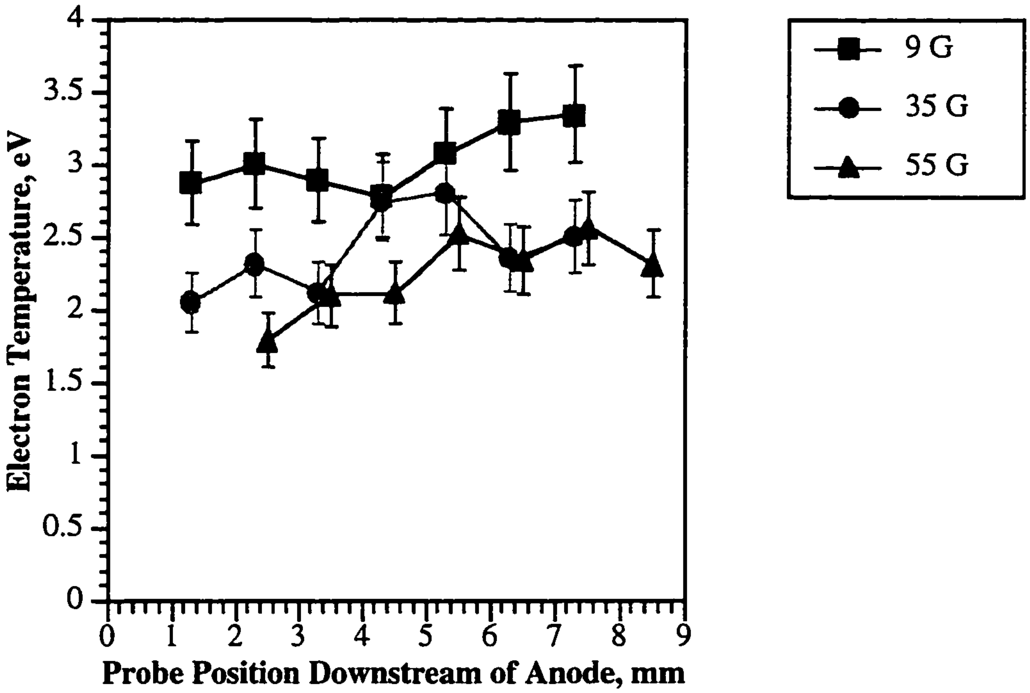

Figure B.4. Electron Temperature Variation in the Near-Anode Region.

B.3. Spatial Spectral Profiles

The near-anode region was probed spectroscopically by acquiring light along a fixed optical axis as the discharge was translated (see Figure B.1). Light from argon neutrals and ions was collected from near-anode points located 0.07 mm apart starting at the anode surface. The spatial profiles of the 470.2 nm neutral line and the 473.5 nm ion line were monitored up to 0.28 mm upstream of the anode. The intensity of each Ar I and Ar II line is normalized to the intensity of the line measured at the anode surface.

The spatial variations in the intensity of the 470.2 nm argon neutral line is illustrated in Figure B.5. As the magnetic field increases, the drop off in intensity as a function of increasing distance above the anode becomes more pronounced. This drop-off eventually saturates into a flat profile. Because the anode acts as a physical barrier to the gas flowing from the cathode, a stagnation region is expected to form near the anode surface. The stagnation region is associated with a higher local pressure/neutral number density than what would be observed in the discharge gap itself. Excitation of neutrals in regions near the anode is then expected to increase as the anode fall increases because the electrons entering the anode sheath are accelerated to higher energies by the potential gradient that exists within the sheath. Indeed the anode fall voltage increases from 16.4 V at 18 G to 21.0 V at 44 G to 29.7 V at 63 G. In this respect, an intensity gradient is expected to increase with anode fall voltage. This behavior is experimentally observed as illustrated in Figure. B.5. Here the slope of the intensity profile turns negative as the field strength increases. The relative steepness of the negative slope is a measure of how much energy that an electron gains as it propagates through the anode fall region. The slope is most negative at the highest transverse field strength (63 G), which corresponds to the largest anode fall measured for this investigation.

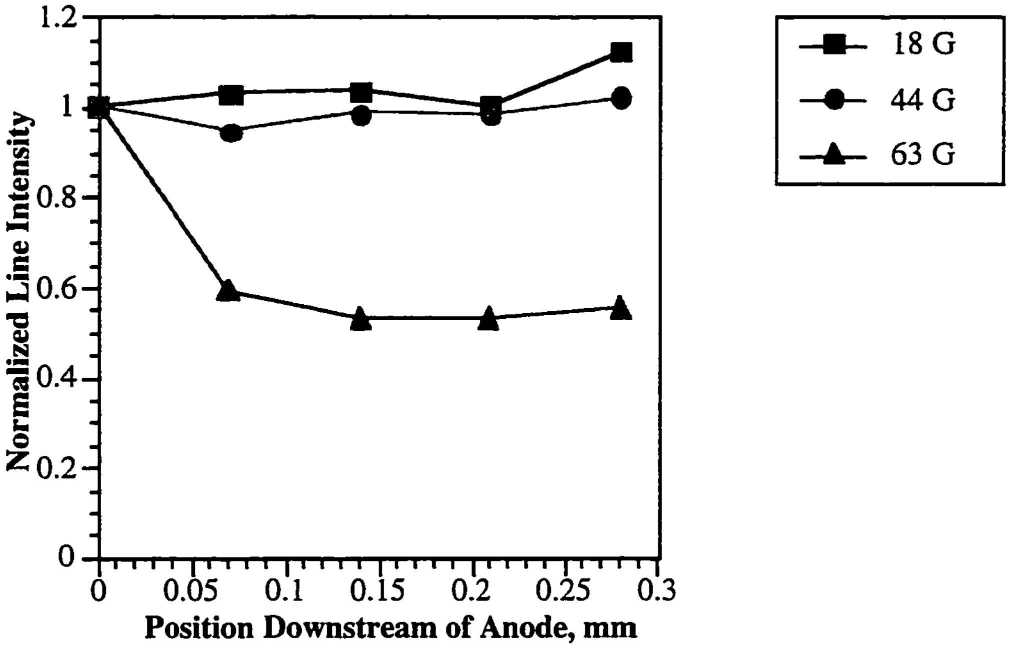

Figure B.5. Spatial 470.2 nm Neutral Line Intensity Variations in the Near-Anode Region.

Spatial variations in the argon 473.5 nm argon ion line shown in Figure B.6. appear to reflect changes in the anode fall voltage as the transverse magnetic field is varied. The slope of the intensity profile near the anode changes sign as the magnetic field increases. The slope near the anode turns positive with increasing magnetic field strength. These changes are consistent with the variations of the anode fall voltage which increases with increasing magnetic field strength for the operating conditions investigated here. The presence of an ion density gradient, with the ion density decreasing toward the anode, is suggested by the ion spectra. This density gradient along with the ion emission intensity gradient is expected to intensify with increasing anode fall voltage. Such an increase in the emission gradient is indicated in Figure B.6. The drop in intensity for the 63 G case beyond 0.1 mm suggests a rather abrupt reduction in the ion production and the ion excitation rate. This reduction may be due to variations in neutral number density downstream of the anode. The stagnation region near the anode is one possible contributor to spatial variations in neutral densities near the anode.

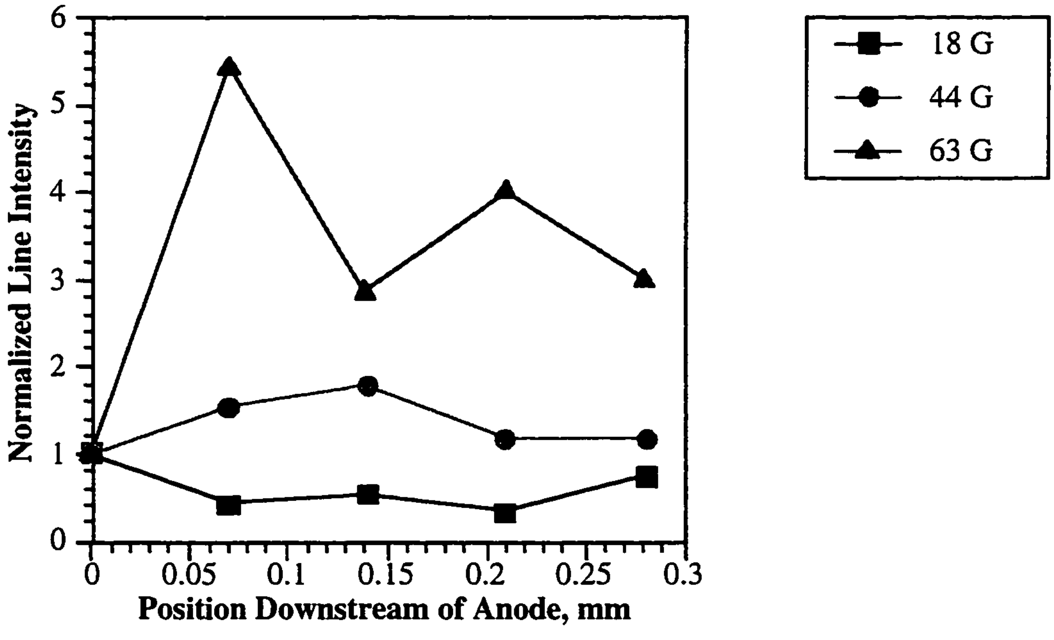

Figure B.6. Spatial 473.5 nm Ar II Line Intensity Variations in the Near-Anode Plasma Region.

B.4. Conclusions

Spatial variations in basic plasma parameters such as electron number density, electron temperature, and plasma potential were fairly constant at fixed transverse magnetic field strength. Such behavior is consistent with that expected from the positive column. Emission spectra intensity gradients measured reflected the changes in the anode fall voltage as the transverse field increased.

Notes to Appendix B

[1] Y.P. Raizer, Gas Discharge Physics (Springer-Verlag, New York, 1991), Chapter 8, Sec. 8.6, pp. 193-194.

BIBLIOGRAPHY

BIBLIOGRAPHY

Beverly III, R.E., Proceedings of the SPIE 7th International Symposium on Gas Flow and Chemical Lasers, vol. 1031, 1988.

Birdsall, C.K. and A.B. Langdon. Plasma Physics Via Computer Simulation. New York: Adam Hilger, 1991.

Burden, R.L., J. D. Faires, A.C. Reynolds. Numerical Analysis. Boston: Prindle, Weber& Schmidt, 1978.

Chen, F. Introduction to Plasma Physics and Controlled Fusion . New York: Plenum Press, 1984.

Cobine, J. and E. Burger, J. Appl. Phys. 26, 895 (1955).

Cox, T.L., V.G.I Deshmukh, D.A.O. Hope, A.J. Hydes, N. St. J. Braithwaite, and N.M.P. Benjamin, J. Phys. D: Appl. Phys., 20, 820 (1987).

Daybelge, U. and B. Bein, Phys. of Fluids, 24, 6, (1981).

Diamant, K.D., E.Y. Choueiri, and R.G. Jahn, Proceedings of the25th International Electric Propulsion Conference, IEPC-95-234, (The Electric Rocket Society Press, Columbus, OH, 1995).

Druyvesteyn, M.T., Z. Phys, 24, 781 (1930).

Foster, J.E. and A.D. Gallimore, Accepted for publication in Physics of Plasmas Journal, 1996.

Fradkin, D.B., Ph.D. Thesis, Princeton University, Department of Aerospace and Mechanical Science Department, 1973.

Gallimore, A.D., Ph.D. Thesis, Princeton University, Department of Aerospace and Mechanical Science Department, 1992.

Gallimore, A.D., A. Kelly, and R. Jahn, AIAA Journal of Propulsion and Power, vol. 9, no.3, 361 (1993).

Gallimore, A.D., R. Myers, A. Kelly, and R. Jahn, AIAA Journal of Propulsion and Power,Vol. 10, No. 2, 262 (1994).

Gallimore, A.D., R.M. Myers, A.J. Kelly, R.G. Jahn, Proceedings of the 27th Joint Propulsion Conference, AIAA 91-2343, (American Institute of Aeronautics and Astrounautics Press, Washington D.C. 1991).

Godyak, V.A., R.B. Piejak, and B.M. Alexandravich, J. Appl. Phys., vol. 73, no. 8, 15, 3657 (1993).

Gon-Ho, K., Ph.D. Thesis, University of Wisconsin, Department of Nuclear Engineering, 1993.

Haydon, S.C. Editor. J.M. Somerville, Contributing author. Discharge and Plasma Physics. Australia: University of New England Press, 1964.

Heidenreich III, J.R. Paraszczak, M. Moisan, and G. Sauve. J. Vac. Sci. Technol. B 6(1) Jan./Feb. (1988).

Hoyt, R.P. et al., Proceedings of the 30th Joint Propulsion Conference, AIAA 94-2992, (The Electric Rocket Society Press, Columbus, OH, 1994)·

Huddlestone, R.H. and S.L. Leonard, Editors. Francis Chen, Contributing author Plasma Diagnostic Techniques. New York: Academic Press, 1965.

Hugel, H., IEEE Transactions on Plasma Science, vol. PS-8, no. 8, 437, December (1980).

Hutchinson, I. H. Principles of Plasma Diagnostics. New York: Cambridge University Press, 1987.

Jahn, Robert G. The Physics of Electric Propulsion. New York: McGraw-Hill Book Company, 1968.

Kaufman, H., Operation of Broad Beam Ion Sources. Virginia: Commonwealth Scientific Corporation, 1984.

Kerkow, H., D. Boubetra and K. Holldack, Nucl. Instrum. Methods Phys. Res., B68, 41 (1992).

Khan, I.H., J.P. Hoabson, and R.A. Armstrong, Physical Review, vol. 129, no. 4, 1513, (1963).

Lide, D.R., Editor in Chief, CRC Handbook of Chemistry and Physics. Ann Arbor: CRC Press, 1994.

Loeb, L.B. Basic Processes of Gaseous Electronics. Berkeley: University of California Press, 1955.

Metcalf, J.C. and M.B.C. Quigley, Proceedings of the Third International Conference on Gas Discharges, (Institute of Electrical Engineers, London, 1974).

Myers, R.M., Proceedings of the 1991 AIAA Joint Propulsion Conference, AIAA-91-2342, (American Institute of Aeronautics and Astrounautics Press, Washington D.C. 1991).

Myers, R.M. and George Soulas. Proceedings of the 1992 AIAA Joint Propulsion Conference, AIAA 92-3463 (American Institute of Aeronautics and Astrounautics Press, Washington D.C. 1992).

Myers, R. M., M. Mantenieks, and J. Sovey, Proceedings of the 21st International Electric Propulsion Conference, AIAA 90-2669, (American Institute of Aeronautics and Astronautics Publishing, Washington D.C. 1990).

Niewood, E.H. and M. Martinez-Sanchez, Proceedings of the 22 nd International Electric Propulsion Conference, IEPC-91-099, (American Institute of Aeronautics and Astronautics Publishing, Washington D.C. 1991).

Raizer, Y.P. Gas Discharge Physics. New York: Springer-Verlag, 1991.

Rapp, D. and P. Englander-Golden, J. Chem. Phys. 43, 1464 (1965).

Rundle, H.W., D.R. Clark, and J.M. Dechers, Canadian Journal of Physics, vol. 51 (1973).

Schall, W., Proceedings of the AIAA 9th Electric Propulsion Conference, AIAA-72-502, American Institute of Aeronautics and Astrounautics Press, Washington D.C., 1972).

Scheuer, J.T. et al., Proceedings of the AIAA 23rd International Electric Propulsion Conference, IEPC-93-118, (The Electric Rocket Society Press, Columbus, OH, 1993).

Shih, K. and E. Pfender, AIAA Journal, vol. 8, 211 (1970).

Soulas, G.and R. Myers, Proceedings of the 23rd International Electric Propulsion Conference, IEPC-93-194, (The Electric Rocket Society Press, Columbus, OH, 1993).

Strangeby, Peter, The Physics of Fluids, vol 27, no. 3, 682 March (1984).

Sugawara, F., The Physics of Fluids, vol. 9, no. 4, 797 April (1966).

Swift, J. and M. Schwar. Electrical Probes for Plasma Diagnostics. New York: Llife Books, 1970.

Tahara, H., M. Sasaki, Y. Kagauya, and T. Yoshikawa, Proceedings of the 1990 21st International Electric Propulsion Conference, AIAA 90-2554, (AIAA Publishing, Washington D.C. 1990).